University of Oxford

Department of Materials

# INORGANIC SEMICONDUCTOR NANOPARTICLES FOR PHOTOVOLTAICS

by

ALEXANDROS STAVRINADIS

St Peter's college


A thesis submitted for the degree of

Doctor of Philosophy

*Dedicated to*

*my father Stavros*

*and my mother Margarita*

**Statements on originality and intellectual ownership**

1/9/2009, Oxford, United Kingdom

I declare that the content of my D.Phil thesis titled "Inorganic Semiconducting Nanoparticles for Photovoltaics" is my own work except of the following parts

- The chemical experiments on the synthesis of PbS and CdS nanocrystals in conjugated dendrites and oligomers presented in Chapter 2 were performed in collaboration with Dr. Elizabeth Thomsen during her visit in Oxford in 2007. All other characterisation on these materials was performed solely by me.
- The XPS and UPS data presented in Chapter 3 were acquired at the University of Nottingham by the employee of the University of Nottingham Dr. Emily Smith. This was performed under an EPSRC-open access contract between me and the University of Nottingham with the written agreement that all intellectual property related to the samples and the analysis of the XPS and UPS data belong to me and the University of Oxford. All relevant sample preparation and analysis of the data was performed by me.
- The schematics of Figure 3.2. in Chapter 3 were adapted from the literature, specifically from two papers published in journals of ACS publications, as stated in the caption of the figure in the thesis. No license agreement is required for the adaption of schematics according to the website of ACS publications.
- STEM microscopy and the relevant STEM micrographs presented in 3.8.c and d were performed by Dr. Rebecca Nichols in the Unversity of Oxford and are used with her kind permission.
- The Schematic of Figure 4.3 on the solar cell fabrication steps was adapted from an original design by Mr. Christopher Cattley with his kind permission.
- The XRD data presented in Chapter 5 were acquired by Mr. Christopher Cattley. The relevant sample preparation and analysis of the data was performed by me.

Alexandros Stavrinadis

# Acknowledgements

The completion of this thesis would not have been possible without the constant teaching, material and intellectual support and encouragement from my supervisors Dr. Jason M. Smith and Dr. Andrew A.R. Watt. Over the last 3 years they always had their office doors open for enlightening discussions, problem solving and brainstorming. More importantly they always allowed me to pursue my own ideas and experiments, do many "crazy" Friday evening experiments just for the fun of it and turn my project to routes that primarily interested me. For all these and many more I thank them as both a student and a friend.

I would also like to thank a number of academic personnel of the University with which I collaborated over the last 3 years and received their advice and expertise: Dr Jamie Warner who helped me understanding better the synthesis of PbS nanocrystals, Dr. Rebecca Nichols who offered me high quality ESTEM imaging of PbS nanocrystals, Dr. John Hutchison who taught me HREM and discussed with me many of my TEM data and Dr. Henry Snaith who collaborated with me on making PbS sensitised Gratzel-type cells. I would also like to thank Dr. Elizabeth Thomsen who as a student in the University of St. Andrews visited our labs in 2007 and conducted with me synthesis experiments on CdS and PbS nanocrystals in conjugated oligomers and dendrimers, Dr. David Keeble from the University of Dundee who collaborated on detailed EPR characterisation on nanocrystal/polymer composites and Dr. Emily Smith from the University of Nottingham who conducted the XPS and UPS measurements under an EPSRC open access contract.

I am also grateful to my co-workers and fellow students in the lab: Dr. Jonathan Moghal, Dr. Brian Patton, Mr. Shek Li, Mr. Christopher Cattley, Mr. Richard Beal, Mr. Shawn Willis, Miss. Laura Droessler, Miss. Elva Zhou, Mr. Simon

Fairclough, Mr. Fabio Grazioso and Mr. Benny Sher. We have shared and taken care of many instruments, discussed a lot of science and had a decent number of pints.

I would also like to thank my studentship sponsors who funded my research: Trackdale ltd, EPSRC, and Armourers and Brasiers. Without their financial support I could not conduct my research.

I am particularly grateful to the people I shared many personal thoughts and problems during the frustrating times of my DPhil studies. Dr Anastassios Antonakos was always on the other side of the phone to discuss problems, solutions and dreams and for his friendship I sincerely thank him. Words can hardly describe my gratitude to Miss Simeonidou-Bessi Parthena who as my life-partner offered me infinite companion, understanding and help during my studies in Oxford. This thesis would not exist without her.

My greatest gratitude goes to my family: Anna, Ilias, Margarita and Stavros. Their unconditional love and support created a beautiful path of life and studies for me to walk.

# Abstract

We investigated the colloidal synthesis, the properties and the application of inorganic semiconductor nanocrystals in photovoltaics. We focused on lead sulphide nanocrystals for the creation of photovoltaics, efficient in the infrared (IR). We studied both organic/inorganic and all inorganic nanocrystal cells.

We showed that PbS and CdS nanocrystals can be directly synthesized in aromatic suspensions of a variety of conjugated organic macromolecules via a surfactant-free low temperature method. Solar cells of PbS/MEH-PPV composites had poor power conversion efficiencies and this was related to self-assembly and oxidation of the nanocrystals during solution processing of the composites. Using detailed TEM we provided mechanistic insights to these phenomena.

The surface chemistry of PbS nanocrystals was further studied using X-ray and ultraviolet photoelectron spectroscopy on all inorganic nanocrystal films. The oxidation, optical absorption and HOMO of colloidal PbS nanocrystals was found to be influenced by post-synthesis processing techniques for ligand exchange/removal.

Subsequently, PbS nanocrystal films were used in Schottky-type solar cells with ~20% external quantum efficiency in the IR. The films were fabricated using an optimised layer-by-layer deposition method. These devices have high (~9mA/cm$^2$) photocurrents but low (0.2-0.3V) open circuit voltage. This problem was addressed by introducing a SnS nanocrystal layer to create a SnS-PbS heterojunction. Device results provided strong evidence for a type II band alignment between the two materials and showed improved power conversion efficiencies compared to control PbS-only devices. We also contributed on the synthesis and characterisation of SnS nanocrystals.

Table of Contents

# Table of Figures

# 1 Photovoltaics and Nanocrystals

## *1.1 Goals of this thesis*

Materials science is the systematic study of the synthesis, properties and applications of materials we use to make our lives better. By that definition this thesis concerns the material science of inorganic semiconductor nanocrystals, particularly metal-chalcogenide (PbS, CdS, SnS) nanocrystals for low-cost photovoltaics. We aim contributing new knowledge on all three interactive aspects of this topic: synthesis and processing of the nanocrystals by means of wet colloidal chemistry, characterisation of the nanocrystals' physicochemical properties, and their applications in nanostructured solar cells.

The specific questions that will be experimentally addressed are: 1) How can nanocrystal/polymer composites be directly synthesized and with what properties? 2) How does the surface chemistry of nanocrystals affect their functionality in solar cells and how can it be controlled? 3) How can different semiconductor nanocrystals be combined for the creation of improved all inorganic-nanocrystal solar cells? 4) What is the best way of utilising PbS nanocrystals as an infrared photoactive material in low-cost solar cells- in plastic or in all inorganic cells?

## *1.2 Structure of this thesis*

This thesis is divided into six chapters. This Chapter introduces the basic operational principles of semiconductor solar cells with specific focus on new solar

cell architectures utilising low-cost solution processed nanomaterials, more specifically inorganic semiconductor nanocrystals. The Chapter continues with a further introduction on the synthesis, chemical and physical properties of nanocrystals and closes with a literature review on the utilisation of various nanocrystal materials in solar cells.

Chapters 2-5 present the experimental findings of 3 years' work in the lab addressing the questions described in **1.1.** Each Chapter can be considered as a self contained piece of experimental work with distinct motivation, background introduction where required, results, discussion and conclusions. Chapter 6 presents the overall conclusions from the combination of the findings in the previous experimental chapters.

## *1.3 Operation of Solar Cells*

### 1.3.1 The solar spectrum

Approximately 1GW $km^{-2}$ of solar radiation heats the surface of the earth at its peak during the day [1]. That radiation's spectrum resembles the one of a black body of 6000K in temperature, modified by the optical absorption and scattering by the earth's atmosphere. As can be seen in Figure 1.1, the earth's surface receives light of wavelength from ~200nm to over 2000nm and the greatest proportion of the solar power lies in the boundary between the visible and the Near Infrared Red (NIR) optical regions [2]. The solar power can be converted to electric potential via the photovoltaic effect [3].

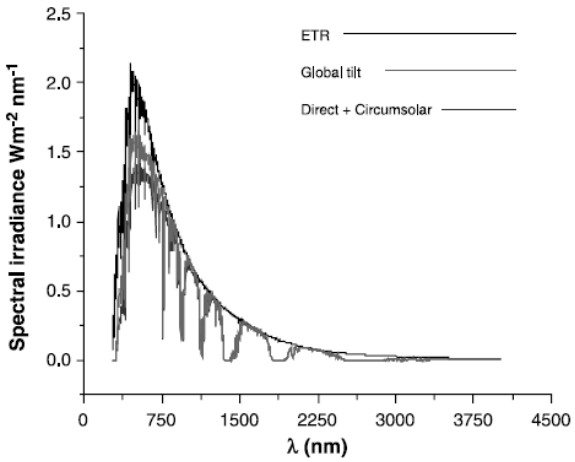


**Figure 1.1 Solar spectrum measured under different conditions. ETR is the extra terrestrial radiation that is the radiation that the earth would receive if there was no atmosphere on the planet. Direct is the nearly parallel (0.5$^o$ divergence cone) to the surface radiation excluding scattered sky and reflected ground radiation. Circumsolar shows spectral irradiance within ±2.5$^o$ field of view centered on the 0.5$^o$ solar disk but excluding the radiation from the disc. Direct+circumsolar is the *A.M.* 1.5 global solar spectrum. Global tilt displays spectral radiation from solar disk plus sky diffuse and diffuse reflected from ground on south facing surface tilted 37$^o$ from horizontal.**

### 1.3.2 The photovoltaic effect

The photovoltaic effect refers to the direct transformation of optical to electrical power in a semiconductor material system connected to an external electrical load. Very simply it can be described as the transformation of incoming photons to outgoing electrons from a semiconductor[4]. As described in the textbook by Dr. Jenny Nelson "The Physics of solar cells" [4], this effect consists of six main processes described below 1) photon absorption 2) carrier generation 3) charge separation 5) charge migration 6) charge collection

### 1.3.3 Photon absorption and charge/exciton generation

If a photon of energy E=hv, where h is Planck's constant and v is the photon's frequency, hits a semiconductor of energy gap $E_g$<E then this photon may be absorbed by the material by the excitation of an electron from the valence to the conduction band of the semiconductor. This process is called photogeneration. The photogeneration rate in a semiconductor is determined by the optical absorption rate of the material which is subsequently determined by the optical absorption coefficient *a(E)*. A light beam of initial intensity $I_o$ is absorbed as it travels though the material and the beam's intensity drop is described by the Beer-Lambert law[4]:

$$I(x) = I_o e^{-ax} \quad \text{(Eq. 1.1)}$$

Where *x* is the distance from the surface of the semiconductor and *a* is assumed to be uniform for all E. We note that the coefficient *a* accounts not only for the photogeneration mechanism but also for other absorption mechanisms like phonon creation or charge scattering, however the last two mechanisms are usually important only for E<$E_g$[4]. We also note that *a* is not uniform for all E, instead for E>$E_g$ *a* is proportional to $(E-E_g)^{1/2}$ and to $(E-E_g)^2$ for direct and indirect bandgap semiconductors respectively.

**Comment [a.s1]:** corrected

In most bulk semiconductors at room temperature photogenerated electrons and holes are considered free carriers which mean that they are not bound as excitons. This occurs because the exciton binding energy in these materials is comparable to or less than kT [5]. However, in semiconductor inorganic nanocrystals this is not the case: the absorption of light results to the formation of excitons. That is a result of the quantum confinement effect, described later in **1.4.3** for nanocrystals**,** which strongly affects the electronic structure of nanocrystals with dimensions comparable to the carriers' wavelengths[6]. Because of this effect the binding energies of the excitons are

**Comment [a.s2]:** deleted sentence about relaxation of carriers in bulk semiconductors

**Comment [a.s3]:** polymers deleted from this sentence

much stronger (>>kT) compared to bulk semiconductors[6] and unless separated by an electric field or heterointerface the photogenerated electrons and holes exist in pairs, the excitons. For that reason these classes of nanomaterials are often called excitonic materials.

**Comment [a.s4]:** I prefer not to mention Frenkel and Mott excitons

### 1.3.4 Charge separation

Bound in pairs or not, the photogenerated holes and electrons must be quickly spatially separated and travel to the electrodes of the solar cell. The speed at which this process should occur in order to have an efficient solar cell is determined by the recombination lifetime(s) $\tau$ of the carriers for the specific material[4]. Recombination can be considered the reverse procedure of photogeneration i.e. the return of the carriers from their excited energy state to their ground energy state via transfer of their energy to another particle like a photon (radiative recombination) or phonon (non-radiative recombination) or another charge carrier (Auger recombination)[4].

**Comment [a.s5]:** Restated t avoid incorrect terminology

Practically, charge separation is induced by the presence of an electric field which drives electrons and holes in opposite directions[4]. In the absence of an externally applied electric field (short circuit condition) an intrinsic electric field, some times called built in field, must be present in order for the device to drive current under illumination. Intrinsic charge separating fields originate from spatial gradients of the electronic levels inside the solar cell which cause gradients in the hole and electron quasi levels $E_{Fp}$ and $E_{Fn}$ respectively. This can be caused by gradients of the valence and conduction band density of states $-\frac{kT}{q}N_v$ and $-\frac{kT}{q}N_c$ respectively, of the electron affinity $\chi$ and of the ionization potential $\chi$-$E_g$[4]. Such changes are

**Comment [a.s6]:** added

**Comment [a.s7]:** replaced the term "built-in

present at the interface of two different regions like between two differently doped regions of the same material (homojunction) as in the case of the p/n Silicon diodes, or between a metal and semiconductor (Schottky junction) or between two different semiconductors (heterojunctions)[4, 7]. [I'm still not happy with this wording. Electric fields are caused by regions of space charge in devices, ie by depletion regions (eg in the case of pn junctions) and accumulation regions (for example in resonant tunnelling diodes). We do not think of the step potential at a heterointerface as an electric field region.] The latter are categorised into type I, II and II heterojunctions according to how the electron affinities and ionization potentials of the two materials are aligned as schematically shown in Figure 1.2.

**Comment [a.s8]:** term "different electronic structures" replaced with term "different regions"

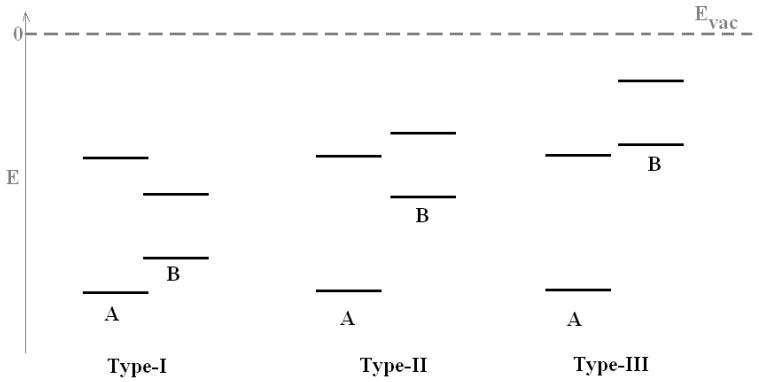


**Figure 1.2 Different kinds of heterojunctions formed due to different alignment of the valence and conduction bands of two different semiconductor materials (A and B).**

Assuming that in the dark the net current at any point is $I=I_n+I_p=0$, then under illumination the hole and electron current densities $I_p$ and $I_n$ at any point of a solar cell is given the following vector equations[4]:

**Comment [a.s9]:** term "vector" added

$$I_n = qD_n\nabla(n-n_o) + \mu_n(n-n_o)(qF - \nabla\chi - kT\nabla\ln N_c) \qquad \text{(Eq. 1.2)}$$

$$I_p = -qD_p\nabla(p - p_o) + \mu_p(p - p_o)(qF - \nabla\chi - \nabla E_g + kT\nabla \ln N_v) \quad \text{(Eq. 1.3)}$$

Where q is the elementary charge, $D_n$ and $D_p$ are the electron and hole diffusion coefficients, $\mu_n$ $\mu_p$ are the electron and hole mobilities, n and p is the density of the free electrons and holes under illumination respectively and $n_0$ and $p_0$ are the respective values at thermal equilibrium and F is the externally applied electric field. We note that while for bulk semiconductors n and p are roughly equal to the number of absorbed photons, in excitonic materials the densities of the photogenerated free carriers n (or p) can be related to the density of the excitons $g_{exc}$ via a factor $c_{ems}$[8]. This factor is the probability of an exciton to diffuse to and be separated at a region with a strong enough intrinsic charge separating electric field e.g. at a heterojunction interface. Then $n=g_{exc}c_{ems}$[8].

**Comment [a.s10]:** replaced the term built-in

### 1.3.5 Charge transport/collection

After holes and electrons are separated they travel to the electrodes of the cell. From the current Equations 1.2 and 1.3 it can be seen that the higher the carrier mobilities in the regions they travel through the higher the photocurrent of the device will be. This is an important aspect of solar cell design and the efficiency of a photovoltaic junction crucially depends on whether the electron- and hole- accepting parts of the junction can facilitate balanced transport of the two different carriers. High carrier mobilities in silicon devices are the main reason why p/n silicon photovoltaics are effective[4].

The mobilities of the carriers in a specific material depend on the electronic structure of the material, its doping density and its crystallinity. According to Bloch theory in a perfect infinite crystal free carriers may travel uninhibited in the crystal[3].

In reality however carriers are scattered inelastically by structural defects which in the case of polycrystalline and nanocrystalline materials become very important. For example in an ensemble of nanocrystals the interface between neighbouring nanocrystals can be considered crystal grain boundary and charge carriers must travel via a "hopping" mechanism between neighbouring nanocrystals[9]. Similar considerations must be made designing the electrodes of a solar cell and the electrode/semiconductor interfaces. The efficiency of the charge collection depends on both presence of defects and electronic alignment across these interfaces[10].

### 1.3.6 The I-V curve of a solar cell

The simplest and first measurement to be done when studying the photovoltaic behaviour of a solar cell is its current-voltage curve in the dark and under illumination which for typical solar cells resemble the ones shown in Figure 1.3 [7]. Most types of semiconductor solar cells act as diodes and so under an applied bias (V) in the dark, the current density I through the cell depends asymmetrically on V as given by Shockley's equation[4, 7]:

$$I_{dark} = I_o(e^{\frac{qV}{nkT}} - 1) \quad \text{(Eq. 1.4)}$$

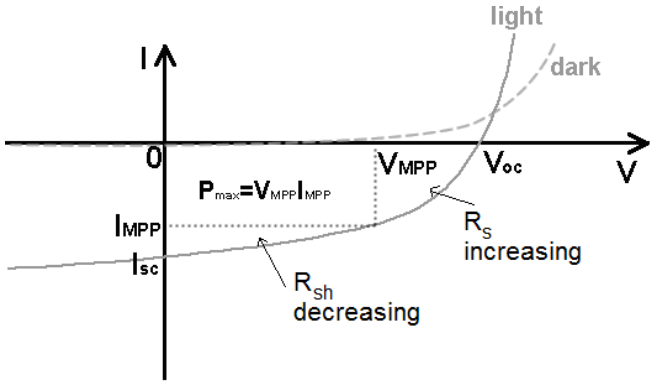


**Figure 1.3 Schematic representation of an IV curve of a typical photovoltaic diode at dark and under illumination, Symbols are defined in main text.**

where $I_o$ is a current density constant, q is the elementary electrical charge, k is the Boltzmann's constant, T is the temperature and n is the ideality factor with minimum value n=1 for an ideal diode. Practically n>1 because of the presence of charge-recombination mechanisms in the diode[4].

**Comment [a.s11]:** corrected

Under steady illumination, a stable solar cell generates a constant current $I_p$, called primary photocurrent, which flows in the reverse direction. The behaviour of most solar cells can be approximately explained considering that the total current flowing through them is the sum of $I_p$ and $I_{dark}$[4, 7]:

$$I = I_o(e^{\frac{qV}{nkT}} - 1) - I_p \qquad \text{(Eq. 1.5)}$$

At zero applied bias the solar cell's photocurrent, called short circuit current $I_{sc}$, is $I_{sc}=I_p$. In reality a solar cell is not an ideal diode and presents resistivity which is analysed to a component $R_{sh}$ parallel to the diode and a component $R_s$ in series to the diode[4, 7]. $R_{sh}$ is also called shunt resistance and generally is associated to leakage currents through the cell's interfaces. $R_s$ is called series resistance and is related to the natural resistivity of the semiconductor constituents and the metal contacts of the solar cell. The equivalent electrical model of solar cell of active area A with parasitic

**Comment [a.s12]:** terminoloy clarified

resistances $R_s$ and $R_{sh}$ is shown in Figure 1.4, and in this case the current of the cell is given by[4, 7]:

$$I = I_o(e^{\frac{q(V+IAR_S)}{nkT}} - 1) - I_{sc} + \frac{V + IAR_s}{R_{sh}} \quad \text{(Eq. 1.6)}$$

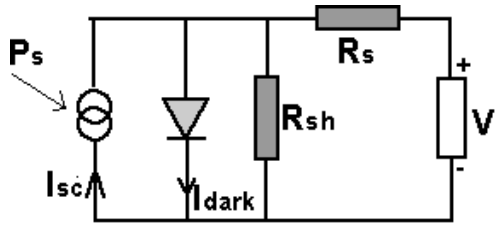


**Figure 1.4 Equivalent circuit of a solar cell**

$R_s$ and $R_{sh}$ qualitatively affect the shape of the I-V curve as indicated in Figure 1.3. The power density P of a cell at any point of its I-V curve is given by:

$$P=IV \quad \text{(Eq. 1.7)}$$

and the cell offers surplus of power to the external circuit when it is operated in the I-V quadrant showed in Figure 1.3. Although for that region the maximum I and V points are $I_{sc}$ and $V_{oc,}$ the maximum power is generated at the point called maximum power point ($I_{MPP}$, $V_{MPP}$) where the product of I and V is maximum and the electrical power is $P_{MPP}=V_{MPP}I_{MPP}$. The solar cell studies presented in this thesis are based on power conversion efficiencies at the ($I_{MPP}$, $V_{MPP}$) point.

The maximum power point is conveniently related to $I_{sc}$ and $V_{oc}$ with the fill factor FF of the cell defined as:

$$FF = \frac{I_{MPP}V_{MPP}}{I_{SC}V_{OC}} \quad \text{(Eq. 1.8)}$$

Thus, a cell presenting $I_{sc}$ and $V_{oc}$ under a constant illumination of optical power density Ps, the power conversion efficiency PCE of the cell will be

$$PCE = \frac{I_{SC} V_{OC} FF}{P_S} \quad \text{(Eq. 1.9)}$$

It is obvious that the efficiency of a solar cell crucially depends on FF which should be as large as possible. This is theoretically achieved when $R_s$ is 0 and $R_{sh}$ is infinite.

### 1.3.7 Solar Cell Generations

Today, the photovoltaic effect is best exploited in terms of power conversion efficiency via solid-state photodiodes of bulk inorganic semiconductors [11]. Inorganic semiconductors are ideal for such applications due to their good and well understood optoelectronic properties such as high carrier mobilities and band gaps within the solar optical spectrum [1, 12]. After the first announcement for Si based cells with 6% power conversion efficiency 65 years ago, two generations of photovoltaic devices (PV), one based on silicon wafers and one on thin film multi-junctions, were developed. [13]. Today we speak of commercial and state-of-the-art cells with ~10-20% and 38.8% power conversion efficiencies respectively [11]. Despite their high efficiencies, the large scale use of bulk semiconductor solar cells is hindered by high financial cost. The growth and processing of semiconductor wafers and thin films are achieved with complex physical processes requiring expensive equipment such as ultrahigh vacuum systems [14]. This fact has driven interest to the development of alternative very low cost-materials for PV.

For 3rd generation PV attention has been focused on macromolecular photoactive materials, namely: organic dyes, conjugated polymers, fullerenes, inorganic nanocrystals and composites of the above [1, 14-17]. These materials can be synthesized by means of low cost colloidal chemistry and can be processed by simple

and cheap solution-based techniques towards the production of novel solar cells. Because of their low cost, it is believed that macromolecular material- based solar cells will become commercially competitive to the classic ones when the relatively moderate milestone of stable 10% power conversion efficiency is reached [16] .

For the solid-state dye-sensitized solar cells, the highest efficiency achieved so far is 3.8% [18]. In terms of efficiency, the research on conjugated polymer cells has been more fruitful. Very recently scientists from the University of California-Santa Barbara and Gwangju Institute of Science in Korea announced conjugated-polymer tandem cells with 6.8% efficiency [19]. The use of nanocrystals in solar cells has been mostly focused on the creation of heterojunctions with conjugated polymers and fullerenes, and nanocrystal/metal Schottky junctions.

Before the detail review of the progress which has been made so far in the field of nanocrystal based PV, some basic concepts on conjugated polymers, nanocrystals and polymer/nanocrystal composites will be briefly presented.

## *1.4 Materials*

### 1.4.1 Conjugated polymers

Conjugated polymers are materials that combine the optoelectronic properties of inorganic semiconductors with the advantageous mechanical properties of plastics [20, 21]. When functionalized with side chains like long alkyl and alkoxyl groups, they can be easily solution-processed towards the production of large scale optoelectronic devices [22]. Typical examples of successfully used polymers in PV are

poly[2-methoxy-5-(2'-ethylhexyloxy)-p-phenylene vinylene] (MEH-PPV) and poly(3-hexylthiophene) (P3HT) [16, 22].

The common characteristic of all conducting polymers is the alternating single (σ-bond) and double (σ-bond plus a π-bond) carbon-carbon bonds along the backbone of the polymer chain [15]. The π-bond between two neighbouring carbon atoms is formed due to the overlapping of the atomic $p_z$ orbitals, and their hybridization into the formation of π (bonding) and $\pi^*$ (antibonding) molecular orbitals [23]. In a chain of more than two π-bonded carbon atoms, the $p_z$ orbitals are further delocalized and the electronic bandgap $E_g$ between the highest occupied molecular orbital (HOMO) of the π states and the lowest unoccupied molecular orbital (LUMO) of the $\pi^*$ states decreases providing semiconducting properties to the material [15, 20, 23].

Generally, the larger the length of conjugation is, the lower the electronic bandgap will be [20]. For polymers however, the conjugation does not extend along the whole length of their chains. It is rather confined in straight segments, usually 4-10 monomeric units long, called chromophores which are located in between points of twisting and coiling of the chains [20]. The energy bandgap of each chromophore depends on its conjugation length. Each segment contributes individually to the optoelectronic properties of the polymer like in photogeneration and confinement of excitons. The variations of the chromophores' optoelectronic properties are expressed as a Gaussian distribution of the polymer's $\pi \rightarrow \pi^*$ transitions [23]. For most polymers $E_g$ is in the range 1.5-3eV.

### 1.4.2 Semiconductor Nanocrystals

Semiconductor nanocrystals combine some of the good optoelectronic functionality of the bulk semiconductors with additional features associated with their nano-dimensionality: they can be synthesized and processed towards applications by means of low-cost wet chemistry and their physical properties can be tailored as a function of their size and shape[6]. The last is a result of the so called "quantum confinement effect".

### 1.4.3 Quantum confinement in Nanocrystals

Quantum confinement refers to effect on the wavefunctions and energy level of a quantum particle that is spatially confined between potential barriers. Textbooks by Woggon[24] and Gaponenko[5] offer comprehensive introductions to quantum confinement in nanocrystals: The simplest paradigm of quantum confinement is in the case of a quantum particle in an infinite potential well of length *a* as shown in Figure 1.5 where the potential U(x) is:

$$U(x) = \begin{cases} 0, & |x| \le a/2 \\ \infty, & |x| \ge a/2 \end{cases} \qquad \text{(Eq. 1.10)}$$

Solving the time independent Schroedinger equation for this system:

$$-\frac{\hbar^2}{2m}\frac{\partial^2}{\partial x^2}\psi(x) + U(x)\psi(x) = E\psi(x) \quad \text{(Eq. 1.11)}$$

where m is the particle mass, E is the particle energy and $\hbar$ is Planck's constant, with the boundary condition $\psi(x)=0$ for every $|x| \ge a/2$, gives:

$$\psi^{(-)} = \frac{\sqrt{2}}{\sqrt{a}}\cos\left(\frac{\sqrt{2mE}}{\hbar}x\right) \quad \text{for odd n (n=1.3.5,….)} \qquad \text{(Eq. 1.12)}$$

$$\psi^{(+)} = \frac{\sqrt{2}}{\sqrt{a}} \sin\left(\frac{\sqrt{2mE}}{\hbar} x\right) \quad \text{for even n (n=2,4,6,….)} \quad \text{(Eq. 1.13)}$$

with energy eigenvalues:

$$E_n = \frac{\pi^2 \hbar^2}{2ma^2} n^2 \quad \text{for n=1,2,3….} \quad \text{(Eq. 1.14)}$$

Thus, the smaller the size *a* of the well and thus the more spatially confined the particle inside the well is, the higher the kinetic energy of the particle will be. This is the quantum confinement effect. Another important aspect of this effect is that the interstate energy differences also increase as *a* decreases:

$$\Delta E_n = E_{n+1} - E_n = \frac{\pi^2 \hbar^2 (2n+1)}{2ma^2} \quad \text{(Eq. 1.15)}$$

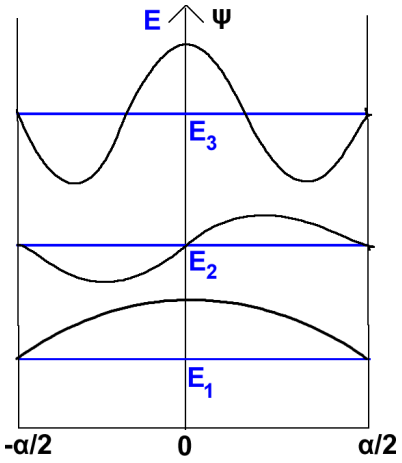


**Figure 1.5. Schematic representation of the wavefunctions and the energy levels of a quantum particle is a square well of length a and of infinite potential walls.**

Nanocrystals resemble the particle in a box model because electrons, holes and quasiparticles like excitons are spatially confined inside the nanocrystals and their energy levels depend on the size and shape of the nanocrystals. Practically this effect becomes important when one or more dimensions of the nanocrystal becomes

comparable to the Bohr radius $a_B$ of the respective bulk semiconductor material, the values of which are in the range 1-40nm for a wide range of II-VI, IV-VI and III-V materials[5]. Under the effective mass approximation in a spherical nanocrystal of radius *a* the energy of the first excited exciton will depend on *a* as[5, 24]:

$$E_{1st-exc} = E_g - R_y * \left[ 1 - \frac{\mu *}{\mathrm{M}} \left( \frac{\pi a_{\mathrm{B}}}{a} \right)^2 \right] \quad \text{(Eq. 1.16)}$$

[this is purely for the weak confinement regime – you should at least say so] and the effective bandgap $E_g^{eff}$ of the nanocrystal, i.e. the minimum energy required to create a pair of free electron and hole, will be larger than the bandgap $E_g$ of the respective bulk material as:

$$E_g^{\ eff} = E_g + \frac{\hbar^2 \pi^2}{2\mu * a^2} = E_g + \left( \frac{\pi a_B}{a} \right)^2 R_y * \quad \text{(Eq. 1.17)}$$

where $R_y$* is the effective binding energy of the exciton, $M=m_e*+m_h*$, $\mu* = \frac{m_e * m_h *}{m_e * + m_h *}$ and $m_e$* and $m_h$* the effective masses of the free electron and hole, all in the respective bulk material [This is really unclear. What are you trying to say?]..

It can be seen that how the radius *a* of the nanocrystal compares to the effective Bohr radius $a_B$ of the material affects critically the energy of the exciton. When $a>>a_B$ and $a_B/a<<1$ then from Equations 1.16 and 1.17 we see that the first exciton's and the first free electron-hole pair's kinetic energies due to spatial confinement are smaller than the binding energy $R_y$* and this is why this nanocrystal size-scale is being called "weak confinement" regime[5]. When however $a<<a_B$ then $a_B/a>>1$ and the first exciton's and the first free electron-hole pair's kinetic energies due to spatial confinement are larger than the binding energy $R_y$*. This situation is called "strong confinement"[5]. In fact in this case, every photoexcited electron-hole

pair should be treated as quasiparticle, some times referred as an "exciton in quantum dot", with a centre of mass motion and a specific binding energy. From the literature we find that the ground state electron-hole pair energy (1s,1S) in the strong-confinement regime will be[5]:

$$E_{1s,1S} = E_g + \frac{\pi^2 \hbar^2}{2\mu * a^2} - 1.786\frac{e^2}{\varepsilon a} \qquad \text{(Eq. 1.24)}$$

where $\varepsilon$ is the dielectric constant of the material and e is the elementary charge of the electron.

With all the above in mind, and without going into detail description of the energy bandsructure in a crystal solid as this would exceed the scope of this introduction, we mention the following qualitative conclusions. When the dimensions of a crystal become comparable to the wavelength of the free carriers in the crystal then the energy dispersion of the carriers does not only depend on the characteristics of the material like the lattice constant and the dielectric constant but also on the dimensions of the crystal. As in the case of the simple particle-in-a-box system, as the dimensions of the crystal decrease the interband energy spacing of the crystal will increase and the absorption spectrum and all its characteristics will shift to higher energies.

**Comment [a.s13]:** deleted confusing sentence on "narrower" DOS

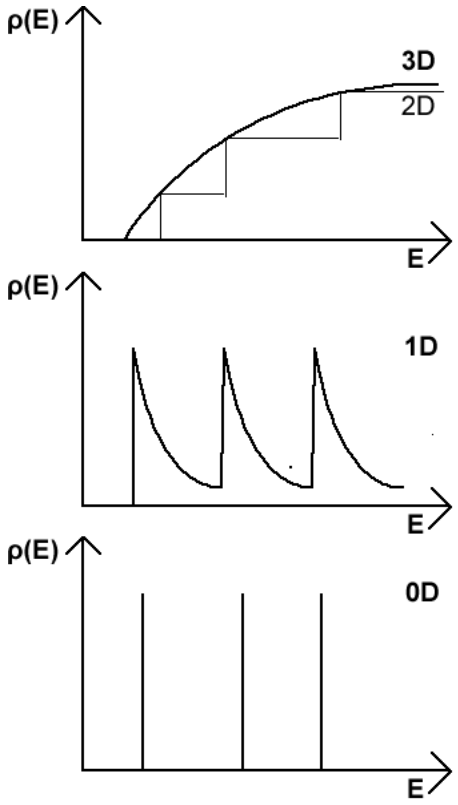


**Figure 1.6 Schematic representation of the density of states distribution in a bulk (3D), a quantum well (2D), quantum wire (1D) and quantum dot (0D) semiconductor**

All the above become evident when the diameter *a* of the nanocrystal is comparable to the effective Bohr radius of the materials. The distribution of energy state density *ρ(E)* for each confined level as a function of energy will also depend on the dimensionality of the confinement via the general relationship $\rho(E) \propto E^{d/2-1}$ with d=1,2,3 the number of the spatially unconfined dimensions of the crystal. For a 0-dimensional quantum dot the density of states will be given by a set of δ-functions as shown in Figure 1.6.

Experimentally as a result of all the above, nanocrystals are highly excitonic materials and nanocrystal samples with narrow size distributions, typically <10%,

present distinct excitonic peaks in their absorption spectrum. The energy of both excitonic peaks and absorption onsets of nanocrystals can be tuned as a function of their size and this has been nicely demonstrated in the literature for the case of PbS nanocrystals of sizes < $a_{B,PbS}$=18nm with excitonic peaks ranging from 500nm to 2000nm[25, 26]. Another consequence of the excitonic nature of nanocrystals is that the photogenerated excitons are "hot" in the sense they can not relax via phonon-assisted paths due to the narrow bandwidth of the energy levels[5, 6, 27]. A consequence of this property is a phenomenon called multiple exciton generation which refers to the relaxation of a high energy exciton via the creation of multiple lower energy excitons[27]. This phenomenon has been observed experimentally for Si and lead and cadmium chalcogenide nanocrystals and has recently being exploited in a PbS nanocrystal photodetector device with an external quantum efficiency >100%[28-30].

### 1.4.4 Colloidal Synthesis of Nanocrystals

Inorganic semiconductor nanocrystals (NC) can be fabricated with various methods such as metal-organic chemical vapour deposition (MOCVD), molecular beam epitaxy (MBE) and colloidal growth [31]. The later approach attracts most of the attention due to its low cost and versatility.

Every method of colloidal growth of nanocrystals includes materials serving the following roles[32]:

- Precursor materials as atomic feedstock for the growth of the desired nanocrystals
- Solvents for the precursor materials

- Molecular agents stabilising the surface of the nanocrystals, controlling the growth rate and preventing coarsening of growing nanocrystals

The majority of the methods for the synthesis of binary semiconductor nanocrystals include an anion (metal) precursor and a separate cation (non-metal) precursor. Common types of metal precursor are simple inorganic salts like chlorides, acetates, oxides with notable examples for the cases of lead and cadmium chalcogenide nanocrystal synthesis: $PbCl_2$[33], $PbO$[26], $Pb(CH_3COO)_2$[34], $Cd(CH_3COO)_2$[35], $CdCl_2$[33]. Depending on the method the above may be used pure or hydrated. The cation precursor is usually an organometallic precursor which decomposes upon anion presence donating the desired cations. Typical examples are: bis(trimethylsilyl)sulphide (TMS)[26] and bis(trimethylsilyl)selendide (TMSe)[36] for the synthesis of chalcogenide nanocrystals. For the latter, elemental S[33] and Se[37] are other options. One category of more sophisticated synthesis methods is based on the use of single organometallic precursors which at high temperatures and/or in the presence of a surfactant they decompose releasing both anions and cations which react forming nanocrystals. For example CdSe nanocrystals have been synthesised by the decomposition of $[(CH_3)CdSe_2CN(C_2H_5)_2]_2$ at $>120^oC$ and presence of tri-n-octyl-phosphine oxide (TOPO)[38].

The precursors need to be solvated in the reaction solution to produce a homogenous atomic feedstock for the subsequent nanocrystal synthesis. Common solvents used are protic polar solvents like fatty acids[26] and amines[33], aprotic polar solvents like dimethylsulphoxide and dimethylformamide[39], non-polar solvents like fatty alkanes and alkenes[34] and finally aromatic solvents like toluene[39]. Water is

another solvent and all methods including water as a solvent are usually called hydrothermal to distinguish from anhydrous methods[40].

At the right temperature solvated anions and cations react and form growing crystals. Obtaining nano-sized crystals requires careful control of the growth rate of the crystals and inter-crystal merging process. This is achieved by using macromolecules with functional sides binding to the surface of the growing nanocrystals controlling both the growth rate and the minimum allowed inter-nanocrystal distance[32]. Commonly used types of such molecules, also called surfactants or ligands, are alkyl phosphines, alkyl phosphine acids and their oxides, fatty acids and their oxides and some nitrogen contained aromatics [32]. The surfactant material is a very important part of the synthesis procedure because usually it also solvates the precursors forming organometallic precursors in the reaction solution. For example oleic acid dissolves PbO forming Pb-oleate[26] and oleylamine dissolves $PbCl_2$ or $CdCl_2$ forming oleyleate complexes[33], all very reactive.

A typical nanocrystal synthesis route containing the above materials is schematically shown in Figure 1.7 and described as follows: in a reaction flask containing surfactants and possibly an additional solvent (step 1 in Figure 5) the metal salt is added and under high temperature (usually >100C) the surfactants dissolve the salt forming complex organometallic complexes (step 2). Then, at a desired temperature, a second solution containing the cation precursor in a readily reactive form is added to the reaction flask (step 3). Then the two precursors react with the anions and the cations forming small crystal nuclei. This is the nucleation stage (step 4). The formed nuclei consist of few atoms, they are surrounded by surfactant molecules attached to their surface, and their stability depends on their size. If a nucleus' radius r is smaller than a specific value called the critical radius r* then the

nucleus dissolves; otherwise it grows further fed by the precursor stock of the solution (step 4)[24]. The critical radius is defined at the radius at which G(r) the free energy per unit volume of the crystal, is a maximum, and depends on many parameters like the nanocrystal material, the surfactant molecules the temperature and precursor concentration[24, 32].

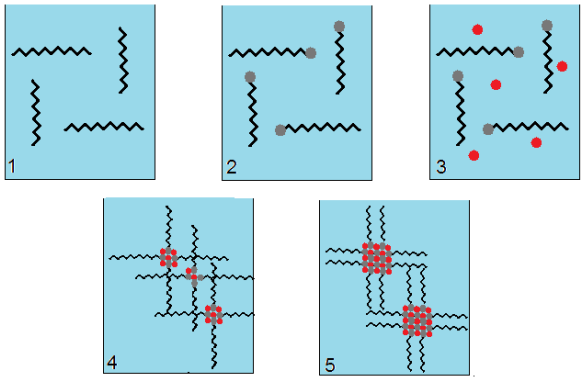


**Figure 1.7 Colloidal nanocrystal synthesis as described in text.**

The critical radius decreases and the growth rate increases as the growth conditions progress as follows: monomer concentration increase, temperature increase and surfactant concentration decrease. In addition the smaller a nucleus is (but with r>r*) the faster it grows at stable growth conditions[32, 41]. The above has offered researchers the mechanistic insight into controlling both the final average value and distribution of nanocrystal size in colloidal synthesis routes, as described in published literature reviews of the subject[32]. A notable example relative to the content of this thesis is the Hines and Scholes method for the synthesis of oleic acid capped nearly PbS nanocrystals[26]. With that method batches of nearly monodispersed nanocrystals with well defined excitonic absorption peaks ranging from 800 to 2000nm can be

obtained by careful control of the oleic acid and lead oleate concentrations in the reaction solution[26].

Another important aspect of colloidal nanocrystal synthesis is controlling the shape of the nanocrystals. There are three main mechanisms that are exploited for shape-control i.e. for creation of anisotropic structures. The first is the anisotropic growth of some materials as a result of their specific structure[31, 42-44]. Two typical examples is the wurtzite CdSe[42] and the hexagonal ZnO[45] which grow favourably across their c axis and nanorods of this directionality can be grown in both cases. The second mechanism is the growth of different structural phases of a certain material at different temperatures[42]. This is best described by the case of growing CdSe nanotetrapod. This is achieved by an initial nucleation and growth of quasispherical zinc-blende CdSe nanodots at temperatures <220$^{o}$C and the subsequent growth of 4 rod-shape wurtzite "arms" onto the zinc blende nanodots when the temperature of the reaction flask is raised above 220$^{o}$C[46]. The third mechanism is a more complex one and is based on controlling the growth rates of the various crystallographic planes of the nanocrystals by the anisotropic affinity of the surfactants on the crystal facets. A nice example of this strategy is the selective growth of PbS nanocubes, nanostars, nanorods and nanowires depending on the relative concentrations of oleic acid, oleylamine and trioctylphosphine in multiple surfactant methods [34, 47].

## *1.5 Nanocrystals in Photovoltaics*

Nanocrystals have been widely investigated as building blocks in nanostructured photovoltaics. The majority of the relevant literature concerns the

photovoltaic properties of conjugated polymer-nanocrystal composites as bulk type-II heterojunctions.

### 1.5.1 Nanocrystal/Polymer bulk type-II heterojunctions

A bulk type-II heterojunction is formed when two macromolecular materials like nanocrystals and conjugated polymer forming a type-II-heterojunction are mixed becoming two percolating networks as shown in Figure 1.8. The photovoltaic effect in such a composite starts with light absorption and photogeneration in both the polymer and the nanocrystals

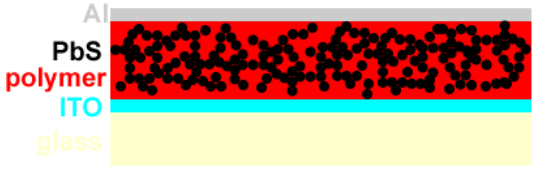


**Figure 1.8 Schematic representation of a nanocrystal/polymer bulk heterojunction device**

Photogeneration of excitons is followed by exciton diffusion. In conjugated polymers this diffusion is assisted by the movement of the excitons towards chromophores of higher conjugation lengths and lower excitonic energy levels. For most conductive polymers the diffusion length is in the range of 4-20nm [14, 48].

The third stage is the separation of the excitons i.e. the formation of free electrons and holes at the interface of a type –II (staggered) heterojunction [1, 14]. In these composites the polymers acts as the electron donor and inorganic nanocrystals as the electron acceptor. The efficiency of the charge separation process can be high

in bulk heterojunction composites because the percolating-networks geometry provides a large interface which assists the charge separation of the excitons in the vicinity of their formation [9, 14].

The separated electrons and holes are then free to travel to the device's electrodes through the materials hosting them. The choice of inorganic nanocrystals as electron acceptors is beneficial for the charge transport process, because conjugated polymers have higher hole mobilities than electron mobilities ($10^{-1}$-$10^{-7}$ and $10^{-9}$-$10^{-4}$ $cm^2V^{-1}$ $s^{-1}$ respectively) [14]. In contrast, bulk inorganic semiconductor have high electron mobilities e.g. 1020 $cm^2V^{-1}$ $s^{-1}$ for PbSe [3]. In nanocrystal composites, however, electron transport occurs via a hopping mechanism rather than via bulk-like transport [9, 49, 50]. In addition, charged sites can repel electrons from travelling to the electrodes [9]. For these reasons, the electron mobilities in the organic/inorganic composites are far from the bulk material values (e.g. $\mu_e$= 84 $cm^2V^{-1}$ $sec^{-1}$ in PbS NC/MEH-PPV composites with 70 wt% NC) [51].

The force pulling the carriers to the electrodes is the electric field created due to the difference between the two electrodes' work-functions. The materials commonly being used for the two electrodes are Ca or Al or both for the top electrode and Au or Indium Tin Oxide (ITO) for the bottom electron, as shown in Fig. 1.8 [1, 14, 16]. The last two come in the form of transparent thin films so they form the transparent electrode via which light enters the device. An additional thin layer of poly (3,4-ethylenedioxythiophene):poly(styrenesulfonate) (PEDOT:PSS) is often used to increase the charge collection, block electrons and lower the work function of the bottom electrode.

The research in the field of polymer/nanocrystals PV has been lead so far by Paul Alivisatos' group in University of California, Berkeley; from that group

Greenham et al. in 1997 were the first to report the fabrication of nanocrystal/conjugated polymer bulk heterojunction solar cells [9]. In this work, trioctyolphosphine oxide (TOPO) coated CdS and CdSe spherical nanocrystals 2-5nm in diameter were incorporated in MEH-PPV. Although the power conversion efficiency (PCE) of the cells was quite low (0.1%), two important concepts were introduced by this work. It was found that when the nanocrystals were washed with pyridine before being incorporated in the polymer, the charge separation of the photogenerated excitons increased. That was manifested by a decrease of the polymer's photoluminescence efficiency by a factor of four compared to the unwashed nanocrystal/polymer composites. The reason was that pyridine removed most of the TOPO ligands from the surface of the nanocrystals. That reduced the distance between the nanocrystals and the MEH-PPV and increased the charge transfer between the two materials [9]. Greenham also discovered that the external quantum efficiency (EQE), i.e. the number of electrons extracted from the device per number of incident photons, increased as the weight percentage of the nanocrystals in the composite increased. The EQE jumped to 12% for a 90 wt% CdSe NC composite, because the specific nanocrystal-concentration lead to the formation of a continuous NC network which eased the transport of the electrons to the Al electrode.

Although the initial experiments on polymer/nanocrystal solar cells proved the potential of this new idea, the <1% power conversion efficiencies were far from ideal. It was evident that further improvement of the cell's performance required consideration of the following:

- broad absorption window,
- efficient exciton separation,
- fast charge transport

From the above, the exciton separation is the least challenging issue today. From the first publication by Greenham et al. it was obvious that this issue could be efficiently tackled by reducing the interface distance between the nanocrystals and the polymer chains via removing the nanocrystals' ligands [9, 49]. It has also been shown that it is possible to grow nanocrystals in conjugated polymer templates without using any surfactants [52].

The absorption window depends on the materials used for the cells. Although the absorption cross-section of both conjugated polymers and nanocrystals is high, and a composite-film thickness of 100-300nm is enough for the complete absorption of wavelengths up to the polymer's excitonic peak[15, 16], polymers do not readily absorb in the IR. In order for this to happen, one needs to use nanocrystals which absorb in these wavelengths. There are semiconductors which do so. However one should keep in mind two things. First, not all semiconductor materials are readily available today in nanocrystalline form (at least not via efficient colloidal chemical methods e.g. the efficient colloidal synthesis for most III-V semiconductors is still not a reality [53] ). Secondly, nanocrystals which absorb in the IR have small energy gaps and because of that, they more often form type-I and not type-II heterojunctions with many conjugated polymers [54, 55]. Generally however improvements over the spectral response of bulk heterojunction solar cells can be seen in the context of different nanocrystal materials used. Finally, the use of nanocrystals with anisotropic shapes and large surface-to-volume ratios has been shown to further improve the efficiency of the exciton separation and charge transport processes [49].

### 1.5.2 Cadmium Chalcogenide Nanocrystals in plastic PV

Since Greenham first used them in 1996 [9], cadmium sulphide and cadmium selenide nanocrystals are the most widely studied NCs for solar cells. CdSe can offer broader absorption spectrum (up to ~750nm) than CdS[9]. CdSe nanocrystals of various shapes, like rods [49, 50, 56, 57], tetrapods [58-60] and "three dimensional snow flakes" [61], have been used in combination with various polymers like MEH-PPV and P3HT in bilayer and bulk heterojunction solar cells. Most of this work has been carried out by the Greenham and Alivisatos groups and it is presented in detail later in **1.5.5**.

Another good infrared absorber is CdTe, however plastic cells with CdTe nanocrystals have not been as efficient as CdSe cells [62]; while CdSe nanorods/MEH-PPV cells present 1.8% PCE under AM1.5 [49], CdTe nanorods/ MEH-PPV cells present 0.052% PCE [63]. Their low efficiency was originally attributed to low percolation network of the nanocrystals [63]. In addition, Zhou et al demonstrated that CdTe nanocrystals form a type-I and not a type-II heterojunction with MEH-PPV and attributed the low PCE values to that reason[62].

### 1.5.3 Lead Chalcogenide Nanocrystals in plastic PV

Binary lead chalcogenide (PbX where X is S or Se or Te) nanocrystals are being widely studied as active materials for low cost PV. These materials are attractive for photovoltaic (PV) applications for three reasons: a) their bulk $E_g$ values lie in the NIR region (>2000nm) and so PbX nanocrystals can potentially absorb from the entire solar spectrum [64], b) their Bohr radii $a_B$ are large, specifically 20nm, 46nm and 152nm for PbS, PbSe and PbTe respectively [29, 64], and thus the optoelectronic properties of nanocrystals with diameters $<a_B$ are a function of their size and shape

within the strong quantum confinement regime c) the multiple exciton generation effect (MEG) in nanocrystals was first discovered to occur in lead chalcogenides [28, 65]. Experiments indicate that MEG in these materials occurs for photon energies $\geq 3E_g$ and leads to exciton photogeneration efficiencies >100%, up to 690 % for PbSe [65].

The first plastic solar cells with lead chalcogenide nanocrystals, composed of PbS and MEH-PPV, were reported in 2005 by the Sargent group from the University of Toronto, Canada [55]. The cells in the initial report by McDonald et al. were not tested under AM1.5 and no PCE values were reported [55]. However, it was demonstrated that these cells did behave as excitonic type-II photodiodes, suitable for PV applications. It was shown that the nanocrystals extended the devices' spectral response in the IR, beyond the polymer's excitonic threshold[55]. Also at short-circuit conditions and under 975 nm monochromatic illumination the internal and the external quantum efficiencies of the devices were ~0.006% and ~0.0008% respectively [55]. These values were very low compared to the best values from cells with cadmium chalcogenide nanocrystals, e.g. in ref [49]. The low efficiencies were attributed to the fact that the nanocrystals' surface was covered with octylamine which hinders the charge transfer between the NCs and the MEH-PPV .

In a later publication, the same group reported that thermal annealing of the devices at temperatures >160 $^{o}$C resulted in significant improvements of their efficiencies[66]: the internal quantum efficiency was raised to 0.15%, the short-circuit current increased by 200 times and the maximum power output increased by a 600 times compared to un-annealed devices. The authors argued that these improvements could be attributed to improved charge transport caused by morphological changes in the polymer film and to partial removal of the nanocrystals' organic ligands during the heating [66].

A way to bypass the problems caused by the presence of surfactants in PbS/polymer composites was reported by Watt et al [51, 52, 67]. Watt managed to synthesize PbS nanocrystals directly in a suspended solution of MEH-PPV without using any surfactants. Composites of 70 wt % nanocrystals with an excitonic peak at 700nm were synthesized that way and used in PV devices with 0.7% under 5mW/cm$^2$ of AM1.5 illumination [67]. The devices showed power conversion efficiencies of up to xxx?.

In 2006, Cui et al presented PbSe NC/ P3HT bulk heterojunctions devices with spectral response up to 1600nm and PCE up to 0.14% [68]. One of their findings was that 33% of their device's photocurrent was originating from excitons generated in the nanocrystals. Similar devices with even broader spectral response up to 2μm were reported by Jiang et al [54] . The devices' PCE values were quite small (0.04 – 0.14% under AM1.5, depending on the incident optical power) and as expected the open-circuit voltage was also low 0.34V[54]. Jiang at al. also showed that PbSe nanocrystals with diameters larger than 8nm formed a type-I heterojunction with P3HT. This fact limits the maximum achievable optical window for devices of P3HT/ PbSe NC composites [54].

Films of PbX nanocrystals have been also used as IR absorbers in solar cells of bilayer[69-71] and Schottky junction architecture[36, 72-75]. These are discussed in greater detail in **1.5.6** and Chapters 4 and 5.

### 1.5.4 Oxide nanocrystals in plastic PV

There are a few reports on the use of nanocrystalline ZnO and $TiO_2$ as active p-type semiconductors in plastic bulk heterojunction PV. Although these materials do

not absorb in the red and IR due to their large bandgaps their use is motivated by the fact they are less toxic and more friendly to the environment compared to lead- and cadmium- containing compounds[1].

In 2004 Beek et al. [76] created a photoactive layer of MDMO-PPV mixed ZnO nanocrystals. The PCE was 1.6% under 0.7 sun illumination (AM1.5). Their devices had high fill factor (FF) 0.6 and $V_{oc}$, 0.6 and 0.86% respectively, and a spectral response up to 700nm. ZnO NCs have been also mixed with regionregular [?] P3HT, but the resulting devices had significantly lower PCEs (<0.9%) [77].

Nanodots and nanorods of $TiO_2$ have been used in combination with various polymers like MDMO-PPV and MEH-PPV forming bulk heterojunctions [78, 79]. Another popular device configuration when using $TiO_2$ is the creation of a nanoporous $TiO_2$ layer made from spin casting of nanocrystals [45, 80] . The pores of the films are then filled with polymer via means of spin casting or deep coating. The PCE from such composites were <0.6% [78] [45].

### 1.5.5 Nanocrystals with anisotropic shapes in plastic PV

Soon after the first paper by Greenham et al [9], the first breakthrough in the field of nanocrystal/polymer solar cells came again from Alivisatos' group when Huynh et al incorporated CdSe nanorods in P3HT for PV [49, 50, 56]. This resulted in cells of power conversion efficiencies up to 1.8% under A.M. 1.5. More importantly, Huynh demonstrated that the improved efficiencies of these devices resulted from the fact that nanorods improve the charge separation and the charge transport processes. Compared to spherical nanocrystals, nanorods have a higher surface-to-volume ratio. Because of this, nanorod/polymer bulk heterojunctions have larger interface areas and

can offer better charge separation compared to spherical NC/polymer composites [56]. In addition, nanorods reduce the number of the of the electrons' inter-particle hops during their transport. Individual nanorods can even act as single conduction pathways for electrons to travel to the top electrode of the device. Improved efficiencies of CdSe nanorod-based PV were presented by the Greenham group in 2006 [81]. They reported the fabrication of ITO/PEDOT/CdSe tetrapod-P3HT/Al devices of 2.6 %PCE under AM1.5. The concepts introduced by Huynh et al. inspired many others to experiment with nanorods in organic solar cells [45, 82, 83]. Despite the advantages of the rods over spherical nanocrystals, a problem arose on the surface: during the spin casting of a composite film, nanorods generally tend to align parallel to the film's plane, rather than vertical to it [60].

This problem was bypassed by the Greenham group in 2003. They were the first to use CdSe tetrapods in making composites for PV [60]. CdSe tetrapods were discovered by Manna et al. [42] in 2000. Tetrapods combine the advantageous properties of nanorods, like high surface-to-volume ratio and linear branches, while at the same time it is physically impossible for them to lie parallel to the film's plain. Spin-cast tetrapods will always have at least one arm facing towards the metal electrode of the device due to their four pointed pyramid-like geometry. Sun et al made PV devices of CdSe tetrapods/ poly (2-methoxy-5-(3',7'-dimethyl-octyloxy)- *p*- phenylenevinylene) ($OC_1C_{10}$-PPV) composites and compared their efficiencies with the ones of CdSe nanorods/$OC_1C_{10}$-PPV devices [60]. Under 0.39mW $cm^{-2}$ illumination at 480nm (the polymer's excitonic peak) the external quantum efficiency (EQE) of the tetrapod device was twice the EQE of the rod. That was consistent with the idea of improved electron transport perpendicular to the plane of the film as a consequence of the shape of the tetrapods [60]. This concept is also supported by the Alivisatos group which

reported plastic cells devices utilising CdTe tetrapods[62] and hyperbranched CdSe and CdTe nanocrystals[84] with power conversion efficiencies as high as 2.2% under AM1.5[61].

### 1.5.6 Nanocrystals in Bilayers heterojunctions

Although bulk heterojunctions offer larger interfaces for charge separation compared to bilayer heterojunctions of excitonic materials, the latter offer solar cells of comparable efficiencies with the former. In 2005, Sun et al. reported the fabrication of solar cells with films of CdSe tetrapods/ $OC_1C_{10}$-PPV composites with 2.8% PCE [59]. This is the best efficiency of CdSe tetrapod/polymer based device ever reported. In these bilayers, the charge separation mostly takes place at the interface between the two different sides [81]. The electrons diffuse to the nanocrystal-rich side and the holes to the polymer-rich side and travel to the respective electrodes. The bilayer configuration is expected to offer better electron mobility with respect to the bulk heterojunction-configuration. In particular, the dense packing of the nanocrystals in the bilayer architecture is expected to improve the electron mobility, because it reduces the number of electron traps on the nanocrystals' surfaces. The latter also reduces the probability of bimolecular recombination of the carriers. Finally, in the bilayer configuration, no short circuit features between the electrodes are expected to be present. The high efficiencies of the cells' fabricated by Sun et al. were in agreement with the above considerations [59].

Another approach to NC based bilayers came from the Silva group in Surrey University. In a series of publications Dissanayake et al.[71, 85, 86] examined the photovoltaic properties of PbS nanocrystal/ $C_{60}$ bilayers. Using optical

photoluminescence, photoelectron spectroscopy and current-voltammetry they studied a type-II heterojunction formed between the two materials and described a simple optical model for the operation of these devices which presented 0.5% power conversion efficiencies.

Nanocrystal/nanocrystal bilayer solar cells are also promising. Gur et al. fabricated solar cells of rod CdSe/rod CdTe bilayers by means of spin-casting [57]. The two materials formed a type II heterojunction with CdTe being the electron-donor and CdSe the electron-acceptor and this combination yielded devices with PCE as high as 2.9% under AM1.5. Surprisingly, the device performance could be further improved by 12% after exposure to air and light for 13 minutes. This is a significant advantage over organic cells which become deficient under the same conditions due to oxidization of the conjugated polymers [57]. However, the cells made by Gur et al. resemble typical 2$^{nd}$ generation devices without offering the high efficiencies of the latter, e.g. relatively cheap bilayers of polycrystalline CdS/CdSe offer 16.5% PCE [87]

Nevertheless, in the period 2007-2009 a number of works on all inorganic nanocrystal based solar cells appeared in the literature. In 2008 Wu et al reported bilayer devices of CuS and CdS nanocrystals with a stable 1.6% power conversion efficient at ambient conditions[88]. In 2009 Sun et al reported PbS nanocrystals/ amorphous Si bilayers with 0.9% power conversion efficiency and 5% external quantum efficiency in the infrared[89]. In a work by Chol et al published as these lines were written 3.4% efficient PbSe/ZnO nanocrystal solar cells were reported, the best all inorganic nanocrystal based photovoltaics produced to date[90].

Many of these works are driven by the potential good electronic properties of nanocrystal solids in excitonic PV [37]. In an array of nanocrystals, charge transport may be increased by energy coupling of the excitonic levels of neighbouring

nanocrystals[91]. The transport can be controlled by matching of the energy levels of neighbouring nanocrystals on the exchange coupling energy between the nanocrystals and on the Coulomb charging energy of the nanocrystals array. Depending on these parameters, the nanocrystal solid can act as a Mott insulator or p- and n-semiconductor [37]. This was elegantly demonstrated by Talapin and Murray in 2005 [37]. They reported a solution-based processing method for making PbSe nanocrystal solids for n- and p-channel thin film field effect transistors (FET). The nanocrystals were highly monodisperse in size and passivated by organic surfactants. By controlling the the nanocrystals' ligands, the researchers were able to control the charge mobilities in the solid. Talapin et al also discovered that exposure of the in hydrazine led to a decrease of the nanocrystals' spacing from 1.1nm to 0.3nm and an increase in the nanocrystal solid's conductance by 10 orders of magnitude. Subsequent vacuum treatment of the films switched their conductivity from n-type to p-type as the hydrazine desorbed. In the same paper, it was claimed that operational FET's from PbS, PbTe, CdSe, and InP nanocrystals and CdSe nanorods had also been fabricated. Because of their findings Talapin and Murray argued that their method had opened the way for sequential layer-by-layer deposition of n- and p-type nanocrystal solids for designing nanocrystal-based photovoltaic cells [37]. FETs from nanocrystal solids have also been investigated by other researchers [92].

## *1.6 This thesis in the context of the literature*

The following 4 experimental chapters cover many of the areas covered in the aforementioned literature. Chapter 2 is an investigation on the surfactant free

synthesis of CdS and PbS nanocrystals in conjugated polymer matrixes for creation of bulk heterojunction composites. The results in Chapter 2 motivated us to further study in Chapter 3 the surface chemistry and electronic properties of PbS nanocrystal films as a function of their chemical and physical processing. We then sought to utilise such PbS films in efficient Schottky-type solar cells as presented in Chapter 4. This work supported our next step on combining PbS and SnS nanocrystals to make efficient bilayer solar cells. The authors' belief is that, overall, all these chapters are connected by the same question spanning across the vast relevant literature: what is the best material combination and device architecture for utilising nanocrystals in solar cells?

**Comment [a.s14]:** made it more "journey" like

# 2 Direct Synthesis of Nanocrystal/Polymer Composites

## *2.1 Synopsis*

This chapter presents new findings on the synthesis and characterisation of organic inorganic composites. It builds on the work reported from 2004 to 2006 by Watt et al. on a surfactant-free single pot method for the direct synthesis of PbS nanocrystal: MEH-PPV composites[51, 52, 67, 93]. Through a series of synthesis and characterisation experiments this chapter shows that the aforementioned method can be generalised for the synthesis of PbS and CdS nanocrystals in a variety of conjugated macromolecules like the MEH-PPV, oligomers and dendrimers. The molecular structures of the conjugated molecules used here are shown in Figure 2.1. The chapter continuous with advanced characterisation of PbS:MEH-PPV composites emphasising the self-assembly of nanoparticle superstructures with morphologies varying from nanorods to 3-dimensional particles. Detailed electron microscopy characterisation of these superstructures suggests specific mechanistic models on the self assembly of the PbS nanocrystals in the composites. The chapter closes with results on devices made from these composites and the conclusions of this work.

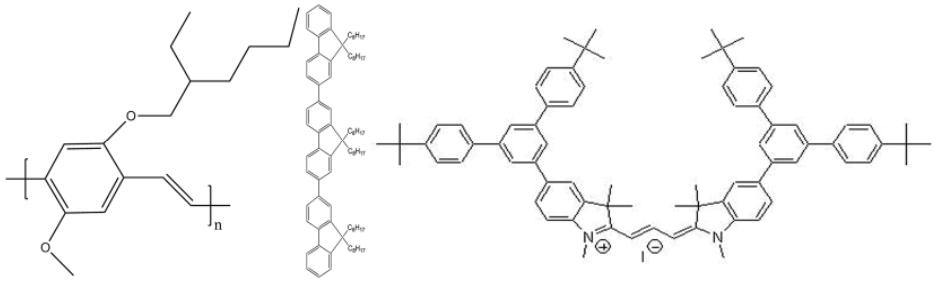

**Figure 2.1 From left to right the molecular structures of MEH-PPV, the conjugated oligomer ADS038FO and the conjugated cyanine-dye core S-dendrimer[94] used in the work presented in this chapter**

## *2.2 Motivation*

Nanocrystal: conjugated polymer bulk type-II heterojunction composites are conventionally produced by mixing colloidal ligand-capped nanocrystals with conjugated polymers at a common aromatic solvent, then spin casting the suspension to form thin films[49, 55, 60, 68]. However as discussed in Chapter 1 the photovoltaic efficiency of the composites strongly depends on the presence and length of ligands on the nanocrystals' surface[9, 66]. These ligands act as energy barriers to carriers moving across the nanocrystal/polymer interface, inhibiting exciton dissociation and charge transport as schematically shown in Figure 2.2 [9]. There are two main strategies proposed in the literature to solve the above problem. One concerns replacing the long fatty ligands like oleic acid or oleylamine with shorter ones like pyridine or primary amines [9, 66]. This method works well with cadmium chalcogenide nanocrystals resulting in solar cell devices with >2% efficiency [49, 61, 81]. However, in the case of lead chalcogenide nanocrystals this method has not produced yet efficient composites [55, 66, 70]. A possible explanation is that lead chalcogenide nanocrystals tend to have low colloidal stability and aggregate unless passivated with long ligands [95, 96].

For the above reasons in 2004 a second strategy was proposed by Watt et al: the direct formation of PbS nanocrystals in a conjugated polymer without the use of surfactants[52]. This chapter includes the basic concepts and results of this strategy and further advancements on the direct synthesis and characterisation of nanocrystal: conjugated polymer composites for optoelectronic applications.

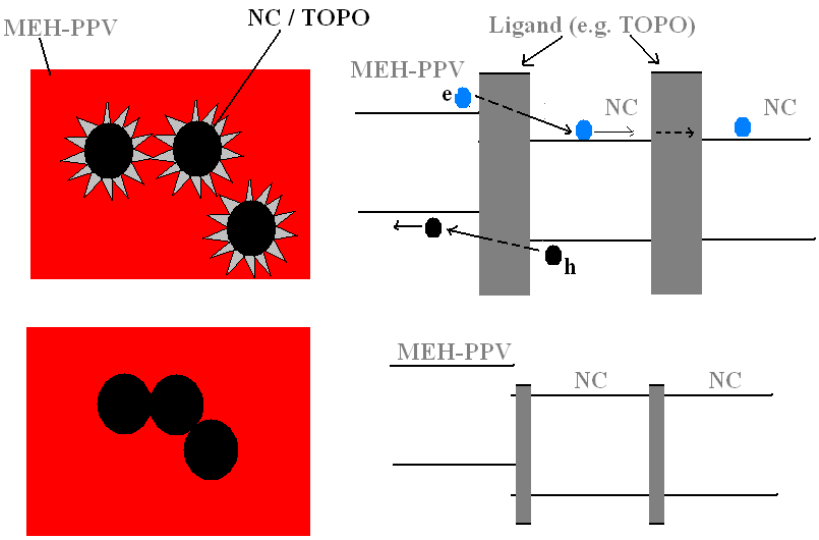


**Figure 2.2 Schematic presentation of the "ligand" problem in nanocrystal: polymer composite. Ligands at the nanocrystals' surface act as energy barriers at the organic/inorganic interface and when removing them this barrier becomes smaller. Based on ref[9]**

## *2.3 Direct Synthesis of Nanocrystals in MEH-PPV*

The first reports of polymer assisted colloidal synthesis of PbS and CdS nanocrystals date back to 1990[97, 98]. The main polymers used in those hydrothermal methods were PVA and PMMA. It was regarded that polymer chains suspended in a medium like water may inhibit nanocrystal overgrowth via steric forces in the same medium and passivate the nanoparticles[97]. Although these methods had no use in optoelectronic applications as they produce low quality and highly oxidised material[97] and neither PVA nor PMMA is conjugated, they indicated that conjugated polymers could potentially be used in a similar manner for synthesis of nanoparticles.

Thus in 2004 Watt et al reported the direct synthesis of PbS nanocrystals in an MEH-PPV aromatic suspension[52]. The details of this method are as follows: an

aromatic solvent like toluene or chlorobenzol or dichlorobenzol is used to completely dissolve MEH-PPV and act as the solvent medium for nanocrystal synthesis. Then lead acetate trihydrate is added in the solution. This salt can not readily dissolve in the aromatic solvent. For this reason dimethyl-sulphoxide (DMSO) is added to the solution. DMSO was chosen for two reasons: it dissolves the lead salt and when added at a small enough quantity and is soluble with the polymer aromatic suspension. This mixture is heated at 100-170$^{o}$C to allow complete dehydration and mixture of the components. A sulphur precursor is also prepared by dissolving elemental S in an aromatic solvent under heat and stirring. When the two solutions are mixed at 80-170$^{o}$C sulphur reacts with the lead forming PbS nuclei growing into nanocrystals while the polymer chains surrounding them prevent aggregation and bulk crystal growth.

There are three main parameters affecting the kinetics of the reaction. The first two are the reaction temperature and the precursor concentrations: the higher these are the faster the reaction and the larger the final nanocrystal size will be[99]. The third parameter is the polymer's molecular weight[99]. It was found that the higher this molecular weight is the smaller the final nanocrystal size will be. This finding gave further support to the idea that polymer chains control nanocrystal growth by acting as steric barriers around the nanocrystals. Under this model, higher molecular weight polymer will occupy a higher effective volume and will result in less available space for the nanocrystals to grow in[99].

The above synthesis method was completed by a post-synthesis purification step of the organic inorganic composite. When the reaction is stopped by cooling to room temperature, methanol is added to the solution. The hydrophobic nanocrystals and polymers chains precipitate under the polar methanol environment while the

unreacted precursors are soluble in methanol and stay suspended. The precipitation step is completed by a centrifuge step, the supernatant is removed and the precipitated composite is redissolved in an aromatic solvent[99].

## *2.4 Experimental Methods*

### 2.4.1 Materials

All solvents used were of >99.8% purity and anhydrous, purchased from Sigma Aldrich. Sulphur flakes, lead acetate trihydrate and Cadmium acetate dehydrate (99.9% pure) were purchased from Fisher Scientific. MEH-PPV (molecular weight 40-70 kDaltons) was purchased from Sigma Aldrich. The conjugated oligomer 9,9,9',9',9",9"-hexakis(octyl)-2,7',2',7"-trifluorene (ADS038FO) ,hereafter called oligomer, was purchased from American Dye. The conjugated dendrimer with a conjugated cyanine dye-core of medium conjugation length and absorption peak at 680nm, hereafter called dendrimer, was used as described and supplied by Dr. Elizabeth Thomsen from the University of St. Andrews[94]. All materials processing and synthesis took place in a dry nitrogen glovebox ($O_2$, $H_20$ <10ppm).

### 2.4.2 Synthesis of PbS nanocrystals in MEH-PPV

The nanocomposite was prepared as follows: 0.1g of lead acetate trihydrate and 0.01 g of MEH-PPV were dissolved in a 12ml anhydrous solution of dimethylsulphoxide (DMSO) and dichlorobenzene (DCB) of 2:1 DMSO/DCB volume ratio. In a second

vial 0.1g sulphur flakes were dissolved in 5ml anhydrous DCB. Both solutions were heated at the same temperature (between 100-170$^{o}$C depending on the experiment) for 1hr under vigorous stirring. Then, 1ml of the sulphur precursor was rapidly injected in the other solution. The system was left reacting at the same temperature for 1h and subsequently left to cool down to room temperature. The composite was then precipitated from solution by the rapid addition of anhydrous methanol or a higher alcohol and centrifuged. The supernatant was then removed and the composite was re-dissolved in toluene.

### 2.4.3 Synthesis of PbS nanocrystals in dendrimer

This synthesis was conducted in collaboration with Dr. Elizabeth Thomsen. Similarly to **2.4.1,** 0.25g of lead acetate trihydrate and 0.05g dendrimer were dissolved in 2ml DMSO and 4 ml toluene. In a second vial 0.1g sulphur flakes were dissolved in 5ml DCB. Both solutions were heated to 110$^{o}$C, then 0.55ml of the sulphur solution was injected into the first solution, and the solution was left to react for 30 minutes. The composite was separated from DMSO by adding a mixture of alcohol and hexane and centrifuging. The composite formed a thick suspension at the bottom of the vial topped by a clear supernatant. These supernatant was removed and the composite was completely re-dissolved in toluene.

### 2.4.4 Synthesis of CdS nanocrystals in MEH-PPV

This is similar to the one described in **2.4.1** with the following modifications: 0.3g of cadmium acetate (with 1-2 degrees of hydration) and 0.01g of

MEH-PPV were dissolved in 4ml DMSO and 8ml DCB. In a second vial 0.2g of sulphur flakes were dissolved in 5ml of DCB. Both solutions were heated to 160$^{o}$C, then 1.5ml of the sulphur solution was injected into the first solution, and the solution was left to react for up to six hours

### 2.4.5 Synthesis of CdS nanocrystals in oligomer

0.1g cadmium acetate dihydrate and 0.01g oligomer were dissolved in 4ml DMSO and 8ml DCB. In a second vial 0.1g sulphur flakes were dissolved in 5ml toluene. Both solutions were heated to 110$^{o}$C, then 1ml of the sulphur solution was injected into the first solution, and the mixed solution was left to react for 4 hours turning yellow as the reaction proceeded. The composite was precipitated using methanol, centrifuged and re-dissolved in toluene.

### 2.4.6 Characterization Techniques

Composites were characterised using Transmission Electron Microscopy (TEM), High Resolution Electron Microscopy (HREM), optical absorption and optical photoluminescence. For electron microscopy samples were made as follows: carbon films (continuous or lacy on Cu grid) were dipped in thin composite aromatic suspensions, then left to dry for 5min before use. Bright and dark field TEM images and diffraction patterns were taken using a JEOL 2000FX operated at 200 kV. HREM was conducted with a JEOL 4000HR operated at 100 kV, equipped with a Gatan digital camera.

The absorption spectra of composite solutions of equal polymer concentrations were acquired with a Jasco V-570 UV/Vis/NIR spectrophotometer with a 1nm data pitch and 5 and 8nm resolutions in the UV-Vis and NIR regions respectively. Fluorescence spectra of composite suspensions and thick composite films on glass substrates were acquired using a Jasco FP-6200 spectrofluorometer. For the optical spectroscopy results presented in **2.5.1** quartz cuvettes containing composite suspensions of equal concentrations were positioned in the fixed cuvette holders of the instrument. Photoluminescence was acquired using 350nm excitation wavelength and a 400nm long pass filter.

For the photoluminescence study presented in **2.5.4,** thin film samples were positioned facing both the light source and the detector at an angle of $45^{o}$. The excitation wavelength was 350nm and a 400nm long pass filter was placed in front of the detector. The composite films originated from the same synthesis which was divided into two equal parts and processed using the two precipitation alcohols. The pristine MEH-PPV film was made from solution which underwent the same processing steps with the same polymer concentration. All films were drop-cast and care was taken to ensure identical processing of all films.

### 2.4.7 Device Fabrication

Devices were fabricated using 14mmx12mm glass/ITO substrates with a 120-160nm ITO nominal thickness and $10\Omega/cm^2$ nominal resistivity purchased from Delta Technologies. Before depositing the nanocrystal films the ITO was patterned using sticky black plastic tape as a mask for wet etching. Etching was done using solution a 25:15:2 mixture of H2O: HCl: $HNO_3$ heated to $60^{o}C$. Etching was complete

after 7 minutes resulting to one 2mm wide ITO stripe across the long axis of each substrate. The substrates were subsequently cleaned by ultrasonication in deionised water, isopropanol and acetone.

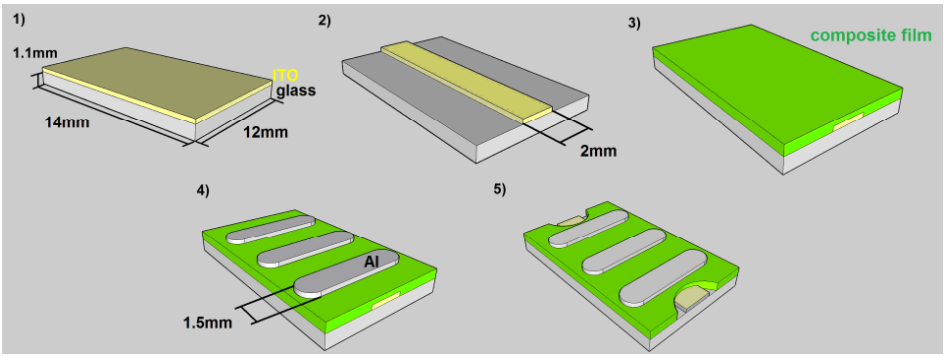


**Figure 2.3 Schematic of the fabrication steps and geometry of the solar cells (courtesy of Mr. Christopher Cattley)**

On the patterned ITO/glass substrate a PEDOT-PSS thin film (<40nm), which is a standard electron-blocking layer, was fabricated by spin casting an aqueous suspension, as purchased by Starck ltd, at 5000rpm for 20sec outside the glovebox then baked at 150$^{o}$C for 10 minutes on a hot plate.

Subsequently thin composite films were spin cast on the glass/ITO/PEDOT:PSS substrates using 0.05g/ml composite in dichlorobenzole suspensions. Spin casting at 1200 rpm for 40 sec followed by drying of the films for 20 minutes produced composite films 200nm ±20nm thick as measured with a Dektak profilometer.

Subsequently, 60-100nm thick Al contacts were thermally evaporated on to the film at a rate of 0.1nm/sec using shadow metallic masks. All NC film fabrication took place in the glovebox and Al evaporation took place in an evaporator attached to the glovebox. The top electrodes were 1.5mm wide stripes across the short substrate

axis. Three 0.03cm$^2$ area device pixels at the overlapping points of the bottom and top stripe electrodes were formed on each substrate. The major fabrication steps for the devices and the device geometry are schematically shown in Figure 2.3.

Comment [a.s15]: Experimental added

### 2.4.8 Device I-V testing

For optoelectronic measurements, devices were loaded in an air-tight inert atmosphere testing holder with a glass window for illumination.

I-V measurements were recorded with a Keithley 2400 source meter. AM1.5 80mW/cm$^2$ illumination was provided by a Newport 130-67005 solar simulator. Light intensity was adjusted using a Thorlabs S210A - Thermopile Sensor for optical power measurements.

## *2.5 Results and discussion*

### 2.5.1 CdS:MEH-PPV

The direct synthesis of CdS nanocrystals in MEH-PPV has several similarities to the synthesis of PbS nanocrystals. Firstly, the average size of the nanoparticles and the size standard deviation increase as the reaction proceeds. This is shown in Figure 2.4 which contains TEM micrographs and nanocrystal size histograms for three different synthesis batches of different reaction durations: 1 hour, 2 hours, 6 hours. For those, the average nanocrystal size develops from 3.58 ± 0.78nm to 4.76 ± 0.75nm and 6.36 ± 1.47nm where error is the standard deviation from the

statistical analysis of 100 nanoparticles for each sample. We note that as the reaction continues the standard deviation and thus the size dispersion of the nanocrystals increases. This is explained considering the Ostwald ripening effect: as the reaction proceeds and the precursor concentration is reduced small nuclei and nanoparticles progressively dissolve in favour of the larger more stable particles in the solution[32]. That results in a broadening of the size distribution.

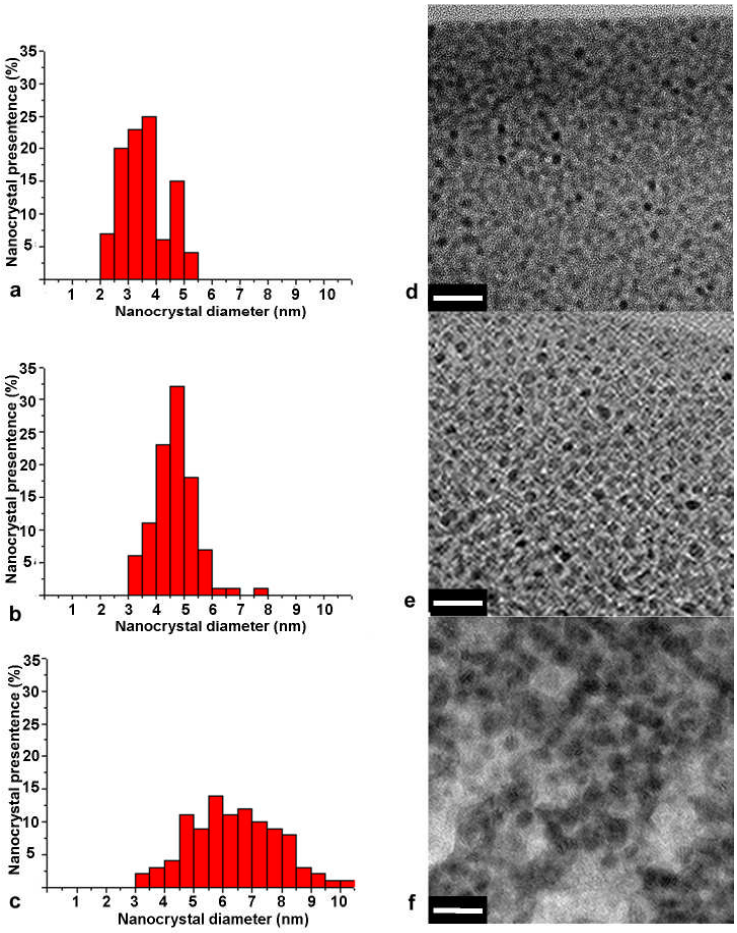


**Figure 2.4 a-c) Size distribution histograms for the CdS:MEH-PPV composites grown for 1 hour, 3 hours and 6 hours respectively. d-e) respective TEM micrographs of the aforementioned composites (scale bars are 20nm)**

**Comment [a.s16]:** Order of samples changed

As the reaction proceeds with time, the nanocrystal loading of the composite also increases and this is manifested in the spectral absorption of the composite. Figure 2.5.a shows the absorption spectra of three different reaction time aliquots from the same synthesis batch and the spectrum from a pristine MEH-PPV solution. All aliquots have the same polymer concentration as is evident from the baseline and the polymer's first excitonic peak at 500nm [52]. According to this graph the absorption in the 340-500nm region increases as the reaction proceeds and a weak peak develops at 370nm. This region lies within the absorption of CdS which has a bulk bandgap of 2.5eV [100, 101].

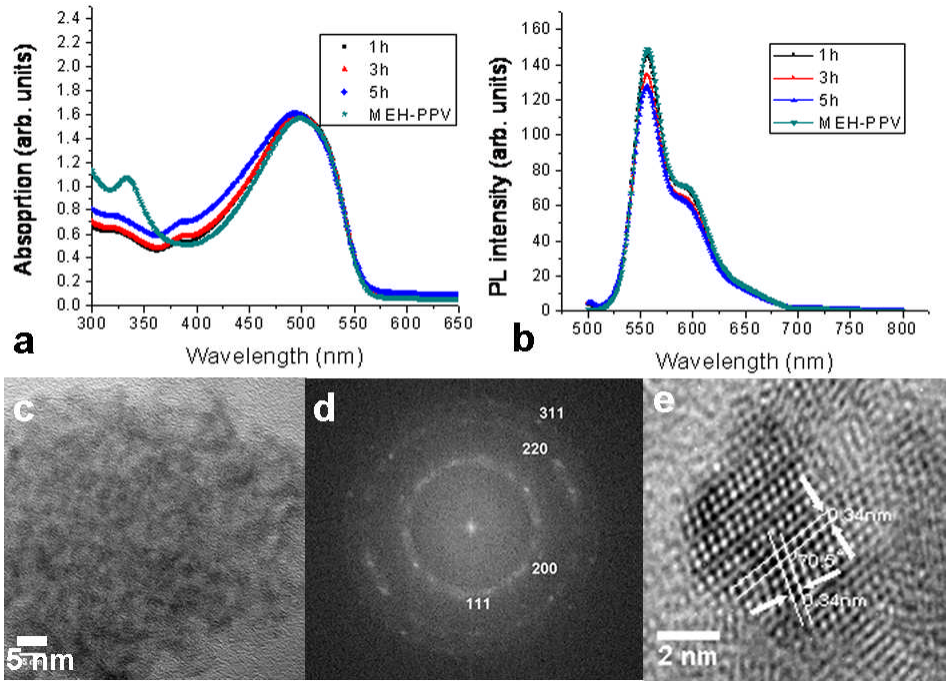


**Figure 2.5 a) Optical absorption of CdS:MEH-PPV composite solutions in toluene with different synthesis duration b) Photoluminescence spectra from the composite suspensions c) TEM micrograph of composite after post-synthesis processing d) FFT pattern of (c) with indexed polycrystalline rings. e) HREM micrograph of a CdS nanocrystal with two sets of (111) planes highlighted**

The photoluminescence spectra of the same aliquots, with excitation at 400nm, are shown in Figure 2.5.b. As the reaction proceeded the intensity of the MEH-PPV photoluminescence peak was reduced. Since the overall PL quenching is small it is unclear whether it originates from charge transfer between the polymer and the nanocrystals or some other morphological change of the polymer chains.

After precipitation, the CdS nanocrystals aggregated forming complex networks as shown in the HR micrograph in Figure 2.5.c. The Fast Fourier Transform (FFT) of the micrograph shows well resolved diffraction rings which correspond to reflections of a CdS zinc blende structure[102]. This result is supported by analysis of HR micrographs of individual CdS nanocrystalites such as the one in Figure 2.5.e. The plane spacings and interplane angles of this nanocrystal agree with less than 5% error with those of the CdS zinc blende structure[102].

### 2.5.2 CdS in conjugated oligomer

When using conjugated oligomers as templates for CdS nanocrystal growth, the latter develop with much more diverse morphologies ranging from spheres as in Figure 2.6.a to rod-shaped as in Figure 2.6.b. Figure 2.6.c shows 4 CdS nanorods being parallel to each other. FFT analysis of this nanorods-assembly further shows a near perfect crystallographic alignment of the rods parallel to their $<110>_{\text{zinc blende}}$ growth axis.

We propose that the morphological differences of the CdS nanocrystals between the MEH-PPV- and the oligomer- based methods are related to the small chain length of the oligomers compared to MEH-PPV. The small size of the

oligomers should result in smaller steric forces applied to growing CdS nuclei compared to using MEH-PPV.

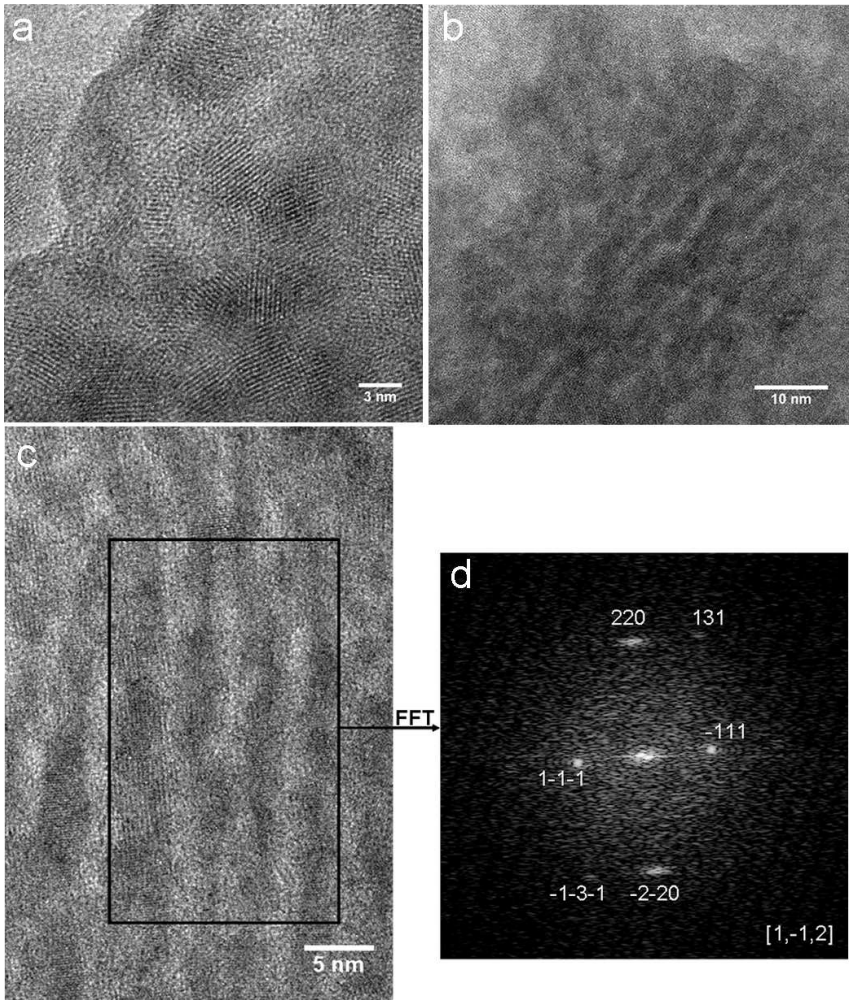


**Figure 2.6 a) TEM micrograph of CdS:oligomer composite after post-synthesis processing. b,c) Micrographs showing existence of parallel CdS rods. d) FFT pattern of the rod assembly highlighted in (c) indexed according to the zinc blende CdS structure. The pattern shows crystallographic alignment of the rods.**

### 2.5.3 PbS in conjugated dendrites

As in the case of oligomer assisted synthesis of CdS nanocrystals, conjugated dendrimer assisted synthesis of PbS nanocrystals results to nanoparticles of random morphology as shown in Figure 2.7.a. The majority of the nanocrystals are smaller than 10nm. An individual nanoparticle is imaged in Figure 2.7.b and its corresponding FFT pattern in Figure 2.7.c verifies the PbS rock salt structure manifested by the characteristic hexagonal shape across the [101] axis.

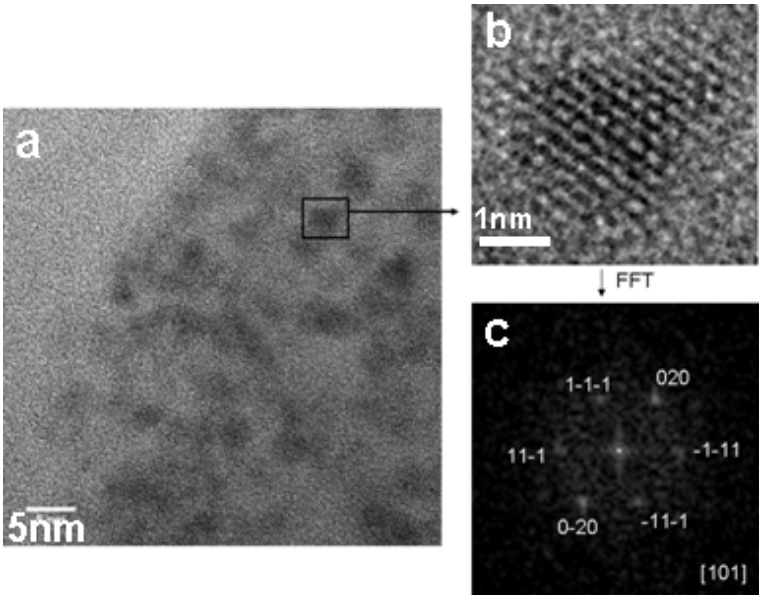


**Figure 2.7 a) TEM micrograph of a PbS:dendrimer composite b) Magnified part of (a) showing an individual nanocrystal c) FFT pattern of (b) indexed according to the PbS rock salt structure**

### 2.5.4 PbS: MEH-PPV

The resulting composites have broad optical absorption as can be seen in Figure 2.8. The extension of the composite absorption beyond the main polymer exciton peak at ~520nm is due to the presence of nanocrystals. The breadth of the

spectral features beyond 600nm indicates that a large distribution of different sized nanocrystals is present. The broadest absorption, extending beyond 1600nm, is from the composite synthesized at 175$^{o}$C. The average diameter of the nanocrystals in this composite was estimated to be 4.5nm by comparing the absorption peak at ~950nm with the theoretical results of Kang and Wise[103]. This value agrees well with the 4.5 ±0.5nm average diameter measured from TEM bright field micrographs such as the one shown in Figure 2.9.a. This micrograph comes from a specimen before the post synthesis treatment of the composite and shows well dispersed nanocrystals in the polymer with broad size distribution (~2-10nm). For this size distribution Kang and Wise[103] predict that the absorption onset should range from ~0.7-2eV ( ~600-1800nm) which is in good agreement with the broad absorption of the composite in Figure 2.8.

**Comment [a.s17]:** Added after JM request

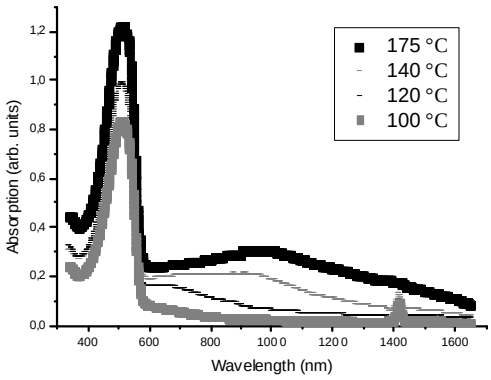


**Figure 2.8 Absorption spectra of nanocrystal/polymer composites synthesized at different temperatures for 1 hour and precipitated with methanol**

We find that using methanol to precipitate post synthesis results in an ordered aggregation of nanocrystals into colloidal particles. The majority of particles have cubic shape and are ~200nm wide, as shown in Figure 2.9.b. Precipitating with higher alcohols, such as ethanol, propanol or hexanol, results in the formation of nanorods as shown in Figures 2.10 and 2.13.a. This is interesting because as discussed

extensively in **1.5.5** plastic composites with nanocrystals of anisotropic shapes like rods may present increase photovoltaic efficiency compared to composites with spherical/cubic nanocrystals due to improved exciton separation and charge transport processes of the former compared to the latter. Thus, we sought to further investigate and understand the nanorods formation in our composites.

**Comment [a.s18]:** Added after JS request

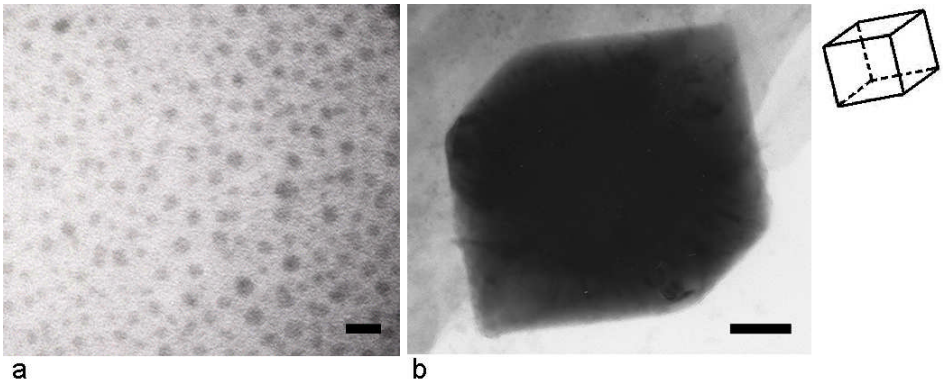


**Figure 2.9 a) Bright field TEM image of the 178°C composite before precipitation b) Cubic colloidal particle projected as indicated by the inserted sketch, formed after precipitation with methanol. (Scales are 20nm and 50nm for a and b respectively).**

### 2.5.5 Formation of PbS Rods

The micrographs in Fig. 2.10.a and 2.10.b show nanorods existing in the conjugated polymer after the precipitation of the composite with ethanol and hexanol respectively. The rectangles in Fig. 2.10.a emphasize areas with clearly distinguishable nanorods. For the ethanol and propanol treated samples, the width of these linear features ranges from 2 to 6 nm with an aspect ratio between 3 and 10. The width distribution of the rods can be attributed to the broad size distribution of the nanocrystals synthesized initially. For the hexanol sample, the nanorods' aspect ratio increases to approximately 20. Many neighbouring nanorods are aligned parallel to

each other, indicated by arrows in Fig 2.10.a and the majority of the features in 2.10.b.

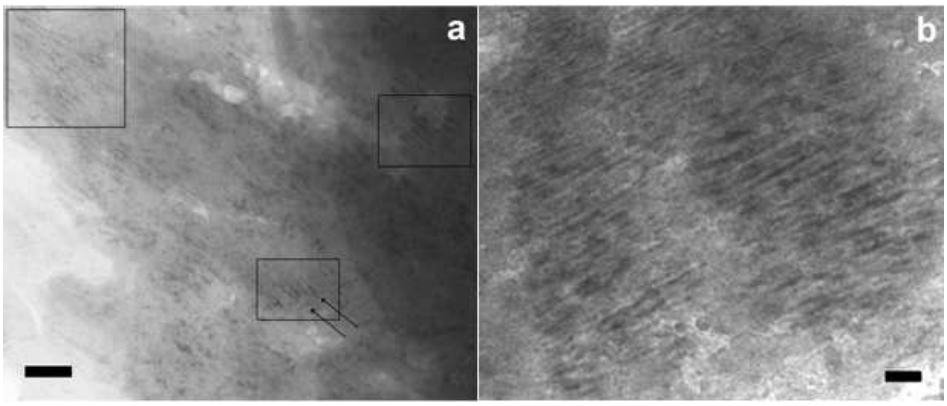


**Figure 2.10 TEM micrographs showing rod structures in polymer after the precipitation of the 175 $^{o}$C composites with (a) ethanol and (b) 1-hexanol. The scales are 40 nm**

In agreement with previous work[52] we observed that the polymer's intrinsic photoluminescence (PL) signature is quenched in the composite sample compared to an MEH-PPV control. The polymer's photoluminescence quenching appears greater in the hexanol- treated sample compared to the methanol treated sample as shown in Figure 2.11.a. We explain this phenomenon considering that the presence of the nanorods in the hexanol treated sample results in an increased surface-to-volume ratio with respect to colloidal particles like the one shown in Fig. 2.9.b . This increases the probability of exciton dissociation at the polymer-nanocrystal interface. Previous studies have shown that increased PL quenching of organic/inorganic composites is correlated to an improvement in photovoltaic performance of the latter[9].

**Comment [a.s19]:** Statement made stronger after JS request

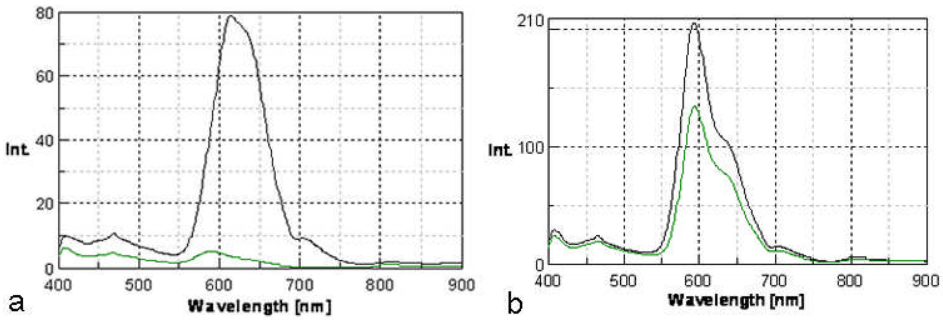


**Figure 2.11 Polymer PL spectra from a composite film (green) and a pristine MEH-PPV film (black) for composites processed with a) hexanol and b) methanol**

Despite the formation of colloidal particles and nanorods, the absorption spectrum of the nanocrystals remains the same before and after the precipitation stage as shown in Figure 2.12. This fact indicates that the morphological and quantum confinement properties of the nanocrystals are not altered by precipitation, and suggests that individual nanoparticles are coated with the polymer and nanorods consist of chains of nanocrystals rather than single crystal rod structures.

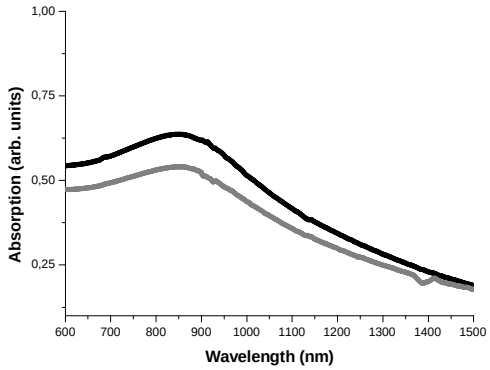


**Figure 2.12 Absorption from the PbS nanocrystals before (black line) and after (grey line) the precipitation of a composite synthesized at 160$^{o}$C for 1 hour.**

We hypothesise that the range of superstructures observed is driven by the internal electric dipole in lead chalcogenide nanocrystals, and that the aggregation

dynamics depend on the polarity of the alcohol used in precipitation:. We are not the first to have observed such an effect. Cho et al. reported that ligand-capped PbSe nanocrystals with quasi-spherical shapes can self assemble into nanorods, nanowires and nano-rings as they grow, depending on the growth temperature[104]. In their work they explain this behaviour by considering dipole interactions between the nanocrystals: a small PbSe nanocrystal with quasi-spherical shape is terminated by six {100} and eight {111} facets. The {100} facets consists of equal Pb and Se atoms but four of the {111} facets are Pb-terminated and the other four are Se terminated {111}. Depending on the spatial distribution of these facets the nanocrystal may have a net dipole moment along the <100> or <111> or <110> directions, or no dipole moment[104]. This then directs nanocrystals with the same or different dipole moments to form linear structures through head to tail attachment e.g. nanocrystals with <100> dipole moments attach and form nanowires across the same axis[104]. The results and the proposed model contained in reference[104], have recently been supported by a computational study by Zhang et al. on the dipole-induced self-assembly of nanocubes[105]. Zhang also suggests that the morphology of the nanocube aggregates is governed by the presence of face to face attractions between the nanocubes. In particular, it is predicted that when these face to face attractions increase, the nanocubes tend to form 2D and 3D structures and not individual 1D nanorods. In our case, such face to face attractions are a result of the hydrophobic behaviour of the nanocrystals in alcohol environments[105, 106].

Based on these reports[104, 105] we believe that the behaviour we observe is a manifestation of the predicted interplay between the dipole induced oriented attraction and the colloidal self assembly of the PbS nanocrystals. We hypothesise that the observed differences in aggregation of nanocrystals using different alcohol solvents is

a result of the different polarities of the alcohols: methanol promotes the aggregation of nanocrystals into 3D structures due to a strong hydrophobic driving force. The hydrophobic forces that the nanocrystals experience in methanol drives them closely packed together forming large cubic colloidal particles. When a less polar alcohol is used for precipitation the nanocrystals feel weaker face-to-face (hydrophobic) attractions. This allows for the dipole-induced self-assembly of nanocrystals to form nanorods. Our consideration of quasi-cubical PbS nanocrystals with the aforementioned faceted geometry is based on previous studies of the faceted morphology of PbS nanocrystals[47, 107] and published results on the formation of quasi-cubical PbS nanocrystals with the method used here[108].

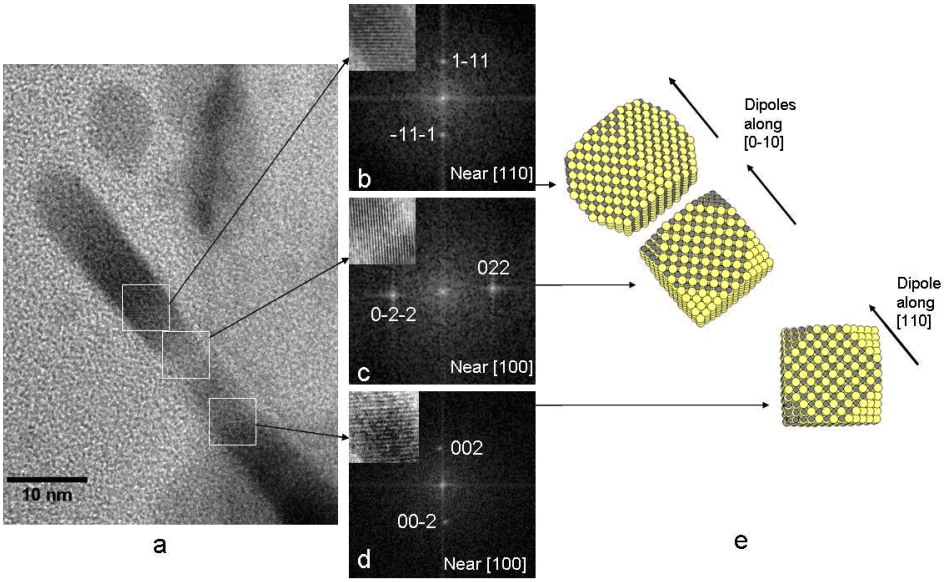


**Figure 2.13 a) High resolution image of a nanorod in the 1-propanol treated composite. b, c, d) FFT images of the nanorod's 3 highlighted square regions with indexed reflections and zone axes. e) Schematic illustration of the 3 nanocrystals in the rod's analysed regions, as projected in the image plane.**

Figure 2.13 shows a micrograph of an individual nanorod and gives an indication of the mechanism for orientated attachment. Three regions of close vicinity

which are indicated by rectangles drawn on the rod in Fig. 2.13.a are examined using high resolution TEM and three distinct crystallographic orientations are observed as shown in the insets of Figures 2.13. b, c and d. Taking the Fast Fourier Transform (FFT) of each image highlights three different planes in the three different regions (Fig. 2.13. b, c, d). The plane spacings were measured to be 0.34 nm, 0.21 nm and 0.29 nm which correspond well to the spacing of the (111), (220) and (200) planes of PbS respectively. Electron diffraction simulations indicate that the zone axes of the three regions are near the [110], [100] and [100] directions. The two adjacent nanocrystals (Fig. 2.13b and c) attach through {100} facets. This alignment of the two nanocrystals across the [0-10] axis can be explained as dipole-induced oriented attachment of PbS nanocrystals with <100> dipole moments, as previously reported[104]. The nanocrystal of the third region has its [110] axis closely aligned with the rod's axis; this can also be explained as the dipole induced orientation of a nanocrystal with a <110> dipole moment. The schematic of Fig. 2.13.e illustrates the relative orientation of the nanocrystals as projected on the image plane. The ordered alignment of the rods shown in Fig. 2.11.a and 2.11.b is consistent with the expectation that it is energetically favourable for neighbouring nanorods to have antiparallel net dipole moments[104]. An interesting task for future work would be to achieve oriented alignment of these nanorods to desired directions within composite layers. Such a capability could be important for applications such as solar cells, which requires efficient transport of carriers to electrodes[60]. Considering the dipole character of these nanorods we suggest that film deposition under an externally applied electrostatic field could lead to alignment parallel to the electric field's direction.

Finally, the observed increase of the nanorods aspect ratio for the hexanol treated composite compared to the ethanol and propanol treated composites can be

explained within the dipole-induced self-assembly context: under the less polar hexanol environment the balance between the face to face attraction and the dipole-induced attraction of the nanocrystals shifts further to the latter. As a result, more nanocrystals can avoid 3D aggregation and form rods via dipole-induced head to tail alignment. In designing polymer-rod composites for photovoltaic applications it is desirable to have control over the rods length in order to avoid short-circuiting from single rods interconnecting the anode and the cathode. The formation of the rods is a dynamic process and choice of alcohol for precipitation allows for partial control of their length. We are encouraged that the length of the nanorods presented here is less than 120 nm, since for nanocrystal-polymer bulk heterojunction solar cells the optimum thicknesses of the active layers in solar devices are close to 200nm[14]. Therefore we predict that the nanorods presented here can be utilised to form suitable percolated networks which will not short in photovoltaic applications.

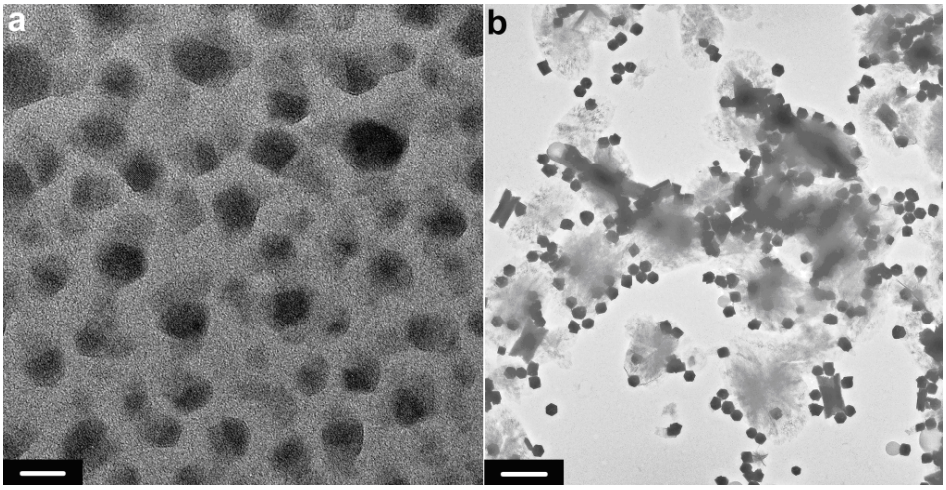


**Figure 2.14 a) As synthesized PbS nanocrystals in polymer matrix and b) PbS NC: MEH-PPV (cubes) and PbS NC: $PbSO_4$ superstructures (elongated parallelograms) after methanol induced precipitation and purification of the nanocomposites. (scale bars are 5nm and 1μm respectively)**

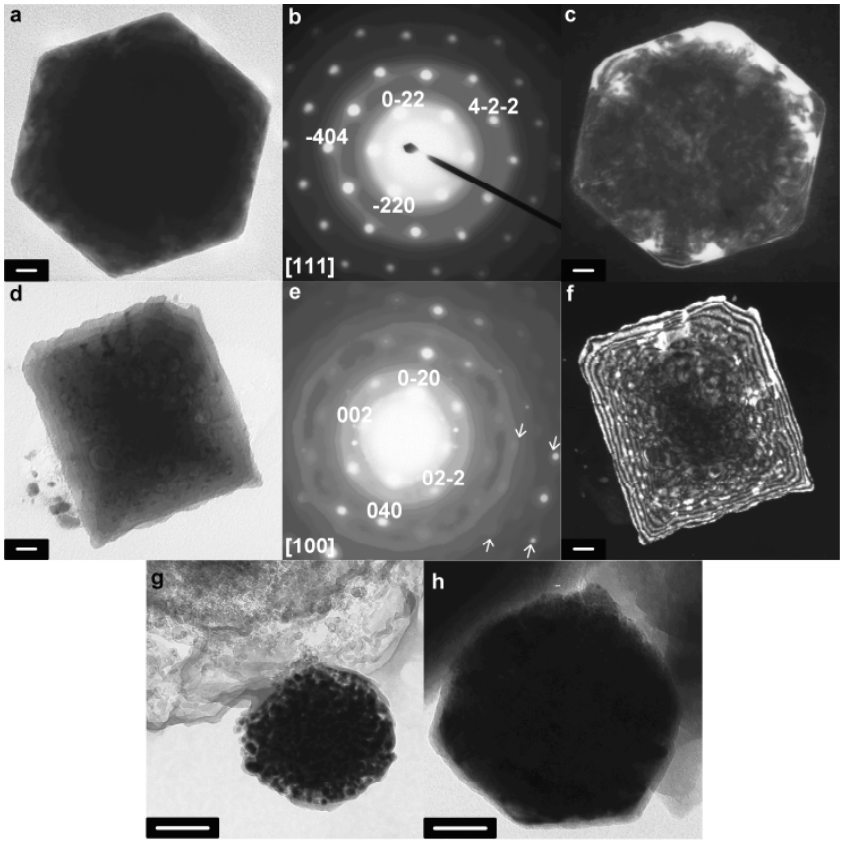


**Figure 2.15 a-c and d-f are bright field, wide angle diffraction pattern and (-4,0,-4) dark field micrograph series of two PbS NC:MEH-PPV colloidal assemblies projected along the [111] and [100] zone axes of PbS respectively g,f) Bright field of incomplete PbS:MEH-PPV colloidal particles showing the incorporation of the polymer (scale bars are 20nm for a,c,d,f, 100nm for g and 50nm for h)**

### 2.5.6 Nanocrystal alignment and formation of colloidal particles

As mentioned above post-synthesis purification of the composite via rapid addition of methanol and precipitation results in the formation of large agglomerate particles, hereafter called particles (or colloidal particles) to distinguish from the original nanocrystals. These particles have sizes ranging between 100-300nm, mean size 200nm, with standard deviation ±30nm as found by statistical study of 100 particles shown in Figure 2.14.b. This micrograph shows a number of particles surrounded by polymer/nanocrystal film. The particles present different shapes

however they are all essentially "cubic", the difference arising from different projections on the image plane e.g. when the cubes are projected across their "<111>" appear as hexagons as in figure 2.15.a while when projected along their "<100>" direction they appear as squares as in Figure 2.15.d. The crystallographic character of the particles seen in the bright field image of Figures 2.15.a and 2.15.d was studied using selective area electron diffraction and dark field imaging techniques. Both diffraction patterns in Figure 2.15 show discrete set of spots that correspond to the rock salt structure of PbS as determined by measuring the interplanar spacing and angles. The discrete set of spots indicates that the PbS NCs are aligned and the diffuse rings are due to the amorphous carbon support. The polycrystalline character of the particles becomes clear looking at the dark field images. The bright shadows inside the body of the [111]- projected particle as shown in its (-404) dark field image point to a large particle of inhomogeneous density. The corners of the particle are bright due to their smaller projected thickness. For the [100]- projected particle the dark field image is more informative: the particle consists of small nanocrystals appearing as bright spots in Figure 2.15.f. The average size of the nanocrystals is 4±2nm in close agreement with the nanocrystal size before composite precipitation. The bright fringes at the edges are thickness fringes indicating that the particular particle is not a perfect cube, rather is can be described as "Maya" type pyramid  The width of the bright fringes is equal to the nanocrystals' average size an indication that the pyramid's terraces consist of single rows of self-assembled nanocrystals. The thickness variation for this particle is also visible in its bright field image. Confirmation that the visible structure originates from the (-404) reflection is that the objects next to the bottom left corner of the particle in Fig. 2.15.d are barely visible in the dark field image of Fig. 2.15.f indicating that those particles are not aligned in the [100] zone axis. In Figure

2.15.e there are additional diffraction spots highlighted with arrows which do not correspond to the PbS structure, we attribute them to the presence of $PbSO_4$ which will be discussed later.

Further evidence for the colloidal character of the large particles is shown in the bright field images of Figures 2.15.g and 2.15.h. The first shows a dense assembly of nanocrystals in what looks like a colloidal particle at an early stage of formation when the nanocrystals have not aligned yet. The particle is located next to a polymer/nanocrystal film with the individual nanocrystals directly visible. It is worth noting the contrast between the poor spatial dispersion of the nanocrystals in Figure 2.15.g and the good dispersion in Figure 2.14.a, which suggests that the precipitation step induces crystallization. In Figure 2.15.h we see another colloidal particle at a formation stage close to completion: The top corner of the particle is incomplete as the nanocrystals visible have not been fully integrated into the assembly thus verifying that the colloidal particles are formed from assemblies of aligned nanocrystals.

We determine that the nanocrystals of the composite solution self assemble rapidly upon the addition of the alcohol forming highly crystalline cubic superstructures. Since the [100]- and [111]- diffractions of the lead sulphide's fcc structure appear from the face-on and corner-on projections of the colloidal cubes respectively, the quasi-cubic nanocrystals assemble via attachment or close facing of their {100} facets. Such faceting of lead chalcogenide nanocrystals is well known[104, 109] and may lead to the creation of intrinsic dipole moments which direct the self-assembly of nanocrystals into one dimensional structures[104]. We have reported such behaviour (**2.5.5**) to explain the formation of nanorods[109]. However as Zhang et al point out in their computational study on the assembly of nanocubes with dipole

moments, when these hydrophobic nanocrystals are present in a highly polar environment such as methanol, hydrophobic face to-face attraction dominates over electrostatic attractions leading to the faceted assembly of the nanocrystals into 3D colloidal particles[105]. We attribute the formation of the cubic superstructures to the assembly of the nanocrystals via their {100} facets.

The colloidal assembly of nanocrystals under the presence of a non-solvent is a well known phenomenon[106, 110]. In most reports however the nanocrystals are capped with long organic ligands preventing them from touching. This inhibits perfect long range crystallographic alignment of the nanocrystals manifested by the formation of bright arcs rather clear bright spots in the wide angle diffraction patterns of colloidal assemblies[111, 112].

Long range crystalline superlattices of a single kind of nanoparticles are usually formed only if the nanoparticles have a narrow size distribution[106, 111, 113]. In our case, the nanocrystals rapidly form colloidal assemblies of high crystallinity giving bright diffraction spots and are polydisperse in size. To explain this we first consider the role of the conjugated polymer. From both Figures 2.15.g and 2.15.h it can be seen that MEH-PPV is incorporated inside the colloidal particles appearing as continuous bright grey areas contrasting the black areas with the distinctive nanocrystal morphology. The MEH-PPV areas are bright due to carbon's lower electron contrast as compared to the much heavier lead. In Figure 2.15.g polymer surrounds individual nanocrystals making up the larger particle. This direct observation is in agreement with the observation that the optical absorption spectrum of the nanocrystals is the same before and after precipitation (Figure 2.12) meaning their quantum confined properties does not change despite their assembly[109]. We consider possible that the plasticity of the incorporated polymer allows it to absorb

any structural mismatch during the rapid close packing of non-uniform nanoparticles thus allowing the long range crystallinity of the superstructure. The second factor we consider to explain long range perfect crystallinity is the presence of a lead sulphate matrix surrounding the nanocrystals inside the particles.

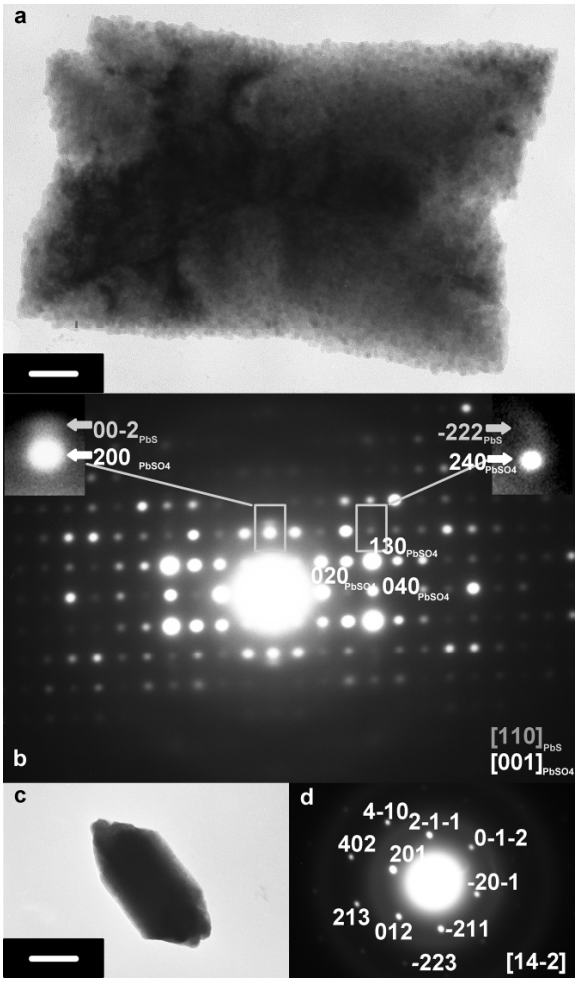


**Figure 2.16 15 a, b ) A PbS NC : $PbSO_4$ ordered assembly and its diffraction pattern showing superposition of monocrystalline-like diffraction from both PbS NC assembly and $PbSO_4$ matrix d) a similar particle projected across a different $PbSO_4$ axis and the resulting $[1,4,-2]_{PbSO4}$ diffraction pattern (scale bars for a and c are 50nm and 100nm respectively)**

In Figure 2.15.e some bright spots which do not correspond PbS planes are indicated by arrows. We attribute these spots to the presence of lead sulphate ($PbSO_4$) which is confirmed by examining the different particles present in the composite. These particles appear as elongated parallelograms in Figure 2.14.b one of which is examined in detail in Figure 2.16. In Figure 2.16.a one can see the smooth morphology of the particle as its vertical axis is thin enough to allow electrons to pass through. Regarding the morphology it is also clear that the particle is partly composed of nanocrystals appearing as spherical features in Figure 2.16.a.

The diffraction pattern from this particle, shown in Figure 2.16.b, indicates two distinct structures: the dominant one is a primitive orthorhombic structure of a large unit cell giving a plethora of diffraction spots forming an orthogonal lattice. The zone axis and the reflections attributed to this structure are noted with white letters on the diffraction patterns. The spacing of the $(100)_{PbSO4}$ and $(010)_{PbSO4}$ planes as measured from Figure 2.16.b are 6.96 ±0.03 Å and 8.47 ±0.03 Å respectively. A similar particle was tilted inside the TEM and an edge-on projection examined as shown in Figure 2.16.c. Assuming the previously described structure has an $[1,4,-2]_{PbSO4}$ diffraction pattern then the third lattice unit is calculated to be 5.38 ±0.04 Å. Modelling the $[1, 4,-2]_{PbSO4}$ diffraction of an primitive orthorhombic structure with the these lattice shows good agreement (deviation <2%) between theoretical and experimental plane spacings and interplane angles of the reflections indexed in Figure 2.16.e. The primitive orthorhombic structure is identified as the structure of $PbSO_4$ with reported lattice units a=6.96 Å, b= 8.48 Å, c= 5.4 Å[114].

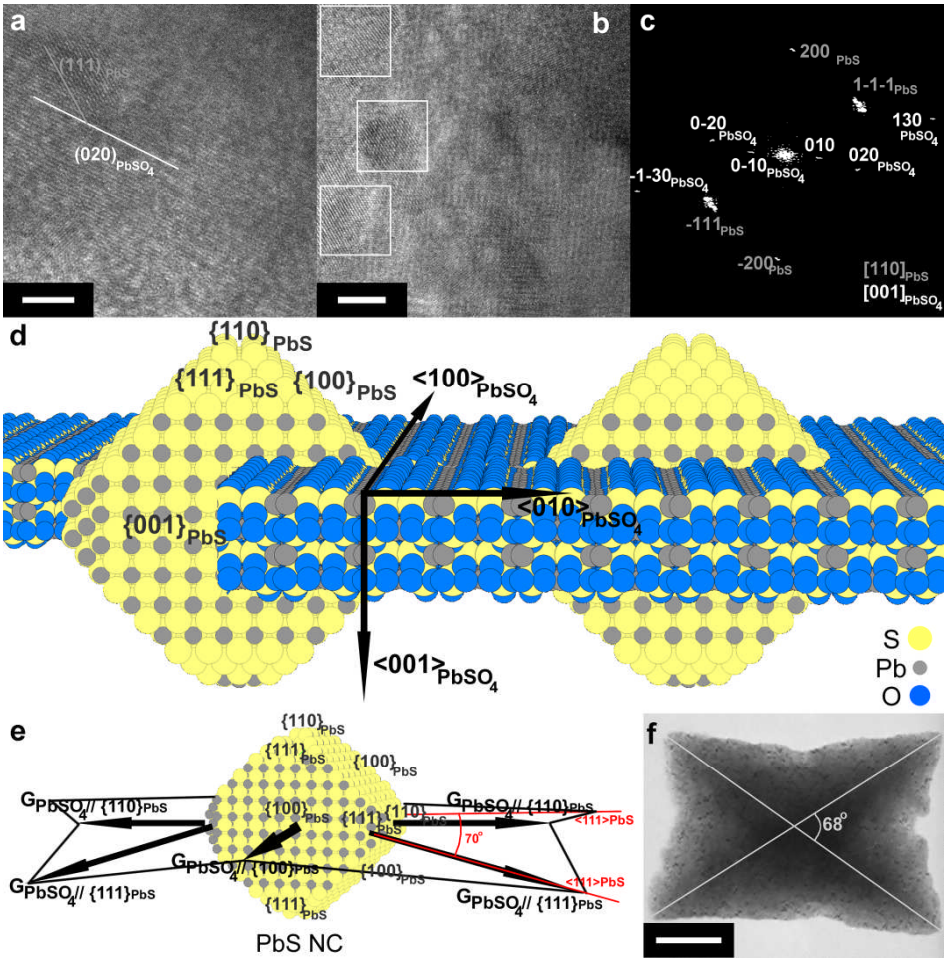


**Figure 2.17 a) High resolution micrograph showing a small PbS nanocrystal incorporated in a PbSO4 matrix and the crystallographic relationship between the two materials b) An ensemble of aligned nanocrystals in a $PbSO_4$ matrix. Different drawn boxes contain individual nanocrystals c) Combined FFT pattern of the regions marked with boxes in b, with indexed reflections. d) Schematic representation of the PbS NC :$PbSO_4$ epitaxial assembly e) Schematic representation showing the proposed different growth rates G of PbSO4 on the various facets of a PbS nanocrystal f) A PbS NC: PbSO4 assembly with the noted angle between the structure's "legs" closely matching the angle between the {111} of PbS noted with red characters in e. (scale bars are 6nm for a, 8nm for b and 100nm for f).**

The PbS reflections in Figure 2.16.b, highlighted by arrows in figure's insets, appear as bright arcs indicating that they come from the nanocrystal ensemble incorporated in the particle and the zone axis for this material is the $[110]_{PbS}$. The (2-

$20)_{PbS}$ are not visible between their spacing and their positioning coincides with the $(040)_{PbSO4}$. Therefore the pattern also provides information about the orientation of the PbS NCs with respect to the $PbSO_4$ crystal structure: inside the assembly $(002)_{PbS}$ and $(2\text{-}20)_{PbS}$ run parallel to the $(200)_{PbSO4}$ and $(040)_{PbSO4}$ respectively.

This orientation relationship is verified by high resolution transmission electron microscopy micrographs shown in Figure 2.17 which further shows epitaxial growth of the $PbSO_4$ around the PbS nanocrystals. Figure 2.17.a shows an individual PbS nanocrystal inside the sulphate matrix. The angle between $(111)_{PbS}$ and $(020)_{PbSO4}$ is measured to be $32.6^o$ in agreement with the angle measured from Figure 2.16.b. This relationship is valid for the entire nanocrystal ensemble of the large particle, Figure 2.17.b shows 3 nanocrystals, highlighted by the square boxes, in a sulphate matrix. The nanocrystals are not in direct contact to each other, still the combined Fast Fourier Transform (FFT) of the 3 regions enclosed in the boxes gives a pattern, shown in Fig. 2.17.c, matching the real diffraction pattern of Figure 2.16.b.

The above epitaxial relationship between PbS and $PbSO_4$ was first observed back in 1952 during studies on the oxidation of bulk PbS under heating at elevated temperatures[115]. It is of great surprise that the same relationship firmly holds at rapid solvent induced oxidation of nanocrystals at room temperature and seems to be responsible for crystallographic alignment of hundreds of assembled nanocrystals, as the ones consisting particle in Figure 2.16.a. To explain this phenomenon we consider the anisotropic surface reactivity of PbS in combination to the nanocrystals' surface morphology. Previous experimental and computational studies on bulk PbS have shown that PbS surface reactivity including oxidation is much stronger at corners, edges and steps compared to {100} due to presence of more dangling bonds in the first cases compared to the last[116] . For PbS facets, the oxidation rates of {111} should

be higher than that of {110} and the rate of {110) higher than that of {100}. The reason is the increase of surface dangling bonds moving from {100} to {110} to {111}. This argument combined with the fact that PbS nanocrystals are high surface-to-volume ratio materials full of {100}, {110} and {111} facets[23] can explain the V-edged orthogonal shape of the PbS NC: $PbSO_4$ assemblies: the growth rates G of $PbSO_4$ should follow the aforementioned relative reactivity of nanocrystals facets. In that case the resulted $PbSO_4$ structure around a PbS nanocrystal would have a V-edged orthogonal shape as schematically shown in Figure 2.17.e. The same applies for the outcome of sulphate formation on the facets of hundreds of assembled and aligned PbS nanocrystals. The fact that the small angle between the "legs" of the colloidal particles- $68^o$ for the particle in Figure 2.16.f.- is very close to the $70^o$ angle between lead sulphide's (100) supports the mechanism we propose.

The formation of the sulphate is attributed to the oxidizing role of methanol during the post-synthesis process of the composites and the possible presence of un-reacted precursor and $H_2O$ molecules originated from the lead acetate trihydrate. Using X-ray photoelectron spectroscopy the Sargent group has also shown that washing of PbS nanocrystals with methanol under a dry nitrogen atmosphere results to mild oxidation of the nanocrystals corresponding to appearance of 5% $PbSO_4$[96]. The strong impact of the nanocrystals' surface oxidation on their optoelectronic applications has been showed in a series of publications[96, 117, 118]. Our results suggest that oxidation of nanocrystals may also result in their crystallographic alignment and describe the epitaxial relationship between PbS and $PbSO_4$. The mechanism of sulphate growth proposed contributes to the ongoing need for modelling and understanding the electronic structure and behaviour of PbS: $PbSO_4$ nanostructures.

### 2.5.7 Solar cell Devices

Directly synthesized PbS:MEH-PPV and CdS:MEH-PPV composites with the properties described above did not give promising device results. Solar cells were prepared and tested with the methods described in **2.4.7** and **2.4.8**. Figure 2.18 shows two typical IV characteristics of these composites in dark and under 80mW/cm$^2$ AM1.5 illumination. The short circuit photocurrents of these devices were 0.005 ±0.002 mA/cm$^2$ for the PbS composites and 0.006±0.001 mA/cm$^2$ for the CdS composites. The CdS composites showed higher open circuit voltages with narrower standard deviation: 1.1 ±0.1 Volts compared to 0.7 ±0.4 Volts for PbS. The Fill Factors for these devices were around 25%. As a result the power conversion efficiencies of more than 30 devices made during the course of this study were less than 1*10$^{-5}$ %.

These low efficiencies were attributed to the observed aggregation of the nanocrystals during post synthesis processing. The formation of micron-sized aggregates does not only result in small organic-inorganic interfaces but also creates the following: i) increased surface roughness of the films ii) light scattering iii) inorganic islands causing short circuiting between the device's electrodes iv) aggregation may alter the HOMO-LUMO levels of the PbS nanocrystals affecting the PbS:MEH-PPV heterojunction character.

From the above possible effects, surface roughness and short circuiting should result in poor $V_{oc}$. Short-circuiting caused by the large aggregates should appear as a Ohmic behaviour in the dark I-V curve of the composites, however we did not observe such behaviour in our devices. This may be explained by our TEM observations that the aggregates are enclosed in polymer matrix. In general, the $V_{oc}$ of the devices was high compared to values (0.3-0.4V)[55, 66] reported in previous works

on PbS:MEH-PPV composites. Notably however, our large values are close to the $V_{oc}$ values (~1V)[119] for pristine MEH-PPV films. This is a first indication that aggregation and oxidation of the nanocrystals yields a poor type-II heterojunction with the polymer.

**Comment [a.s20]:** After J.S request

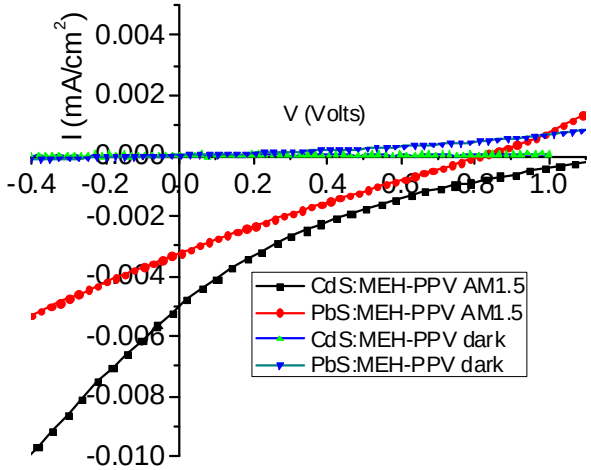


**Figure 2.18 IV characteristics of composite devices in the dark and under 80mW/cm$^2$ AM.1.5 illumination. The devices' performance is poor.**

In the relevant literature the valence band of bulk PbS is -4.9eV and the HOMO level of PbS nanocrystals with first excitonic transitions above 0.8eV is estimated to be around -5.1 to -5.3eV below the zero-vacuum level[55]. Because the HOMO energy level of MEH-PPV is -5.1eV the formation a type-II heterojunction between the two materials requires a strong quantum confinement effect on the PbS nanoparticles keeping their HOMO level below -5.1eV. This means that nanoparticles with an absorption threshold going beyond 0.8 eV (1550nm) may form a type-I and not a type-II heterojunction with MEH-PPV. Although, macroscopically we did not

observe any significant red-shift of the nanocrystals' optical absorption threshold after precipitation of the composites we can not exclude the existence of such behaviour at the nanoscale. In that case, the "affected" nanocrystals would also form a type-I heterojunction with the rest nanocrystals and this would negatively affect charge transport via the nanocrystal network.

The formation of $PbSO_4$ should also negatively affect charge separation at the PbS:MEH-PPV interface. All oxide states of on the surface of PbS act as electron traps and $PbSO_4$ is the deepest trap (-0.34eV) with a very long lifetime (2sec)[118]. Thus free electrons coming from separation of photogenerated excitons at the PbS:MEH-PPV are likely to be trapped in $PbSO_4$. We know nothing about the charge-transfer dynamics between MEH-PPV and $PbSO_4$ and this is troubling considering in that certain areas of our composite $PbSO_4$ is a matrix surrounding the PbS particles. However, considering Greenham's analysis on charge traps on the surface of nanocrystals in plastic photovoltaics[9], we can say that negative charge in any electron-filled $PbSO_4$ localised trap states would most certainly decrease the conductivity of the PbS network and charge transfer at the organic-inorganic interface. All the above, may explain the very small $I_{sc}$ current of our devices.

Two strategies aiming to prevent the aggregation or to break the aggregates were tried. The first was addition of butylamine after synthesis in order to passivate the nanocrystals with short ligands. The second was ultrasonication of the composites in order to break the aggregates. In practice neither method improved the morphology of the composites and both gave devices of worse if not no photovoltaic effect. Neither of these failed attempts came as a big surprise. The epitaxial order in the $PbS/PbSO_4$ structures of our composites indicates ionic bonds between the nanocrystals and the sulphate matrixes and we would not expect simple

ultrasonication to simply break apart nano- and micro-scale crystallites. Butylamine, is one of the shortest ligands used for PbS passivation when used nanocrystals have to be precipitated with a mild alcohol like propanol at low concentrations so they won't severely aggregate. For post-synthesis processing of our composites we need to use large excess of alcohols as precipitation of MEH-PPV is hard. Indeed, aggregation as described above in this chapter was present in the butylamine-treated composites. In addition, although this is known to partially passivate oxide species on the surface of high quality PbS nanocrystals' we would not expect it to have a great impact on the large scale $PbSO_4$ formation in our composites.

The only methods known from the literature for extensive reduction of PbS nanocrystal surfaces are wet treatments with hydrazine or EDT. However, these experiments are beyond the scope of this project for two reasons: firstly because we are aiming at a surfactant-free synthesis of nanocrystal/polymer photovoltaic composites, and secondly because use of strong lewis bases like thiols and amines generates a plethora of questions about the reaction of the latter with the conjugated polymers.

**Comment [a.s21]:** After JS request

## *2.6 Conclusions*

In this chapter a previously reported method for the single-pot surfactant free synthesis of PbS:MEH-PPV composites has been generalised for the synthesis of CdS and PbS nanocrystals in a variety of conjugated organic materials. When CdS nanocrystals are synthesized in MEH-PPV their shape is quasispherical and phase is zinc blende. When synthesized in oligomer the shapes are irregular and zinc blende

CdS rods are formed. Also ensembles of rods with the same growth axis and a high degree of crystallographic alignment have been observed.

In the synthesis of PbS nanocrystals in MEH-PPV the average size of the nanocrystals depends on the growth temperature. Post-synthesis purification of the composites with alcohol-induced precipitation results in the self assembly of the nanocrystals into a variety of structures: rods, colloidal cubes and nanocrystal/oxide assemblies. The size of the rods depends on the polarity of the alcohol used for the precipitation with higher alcohols yielding longer rods. The rods are linear assemblies of nanocrystals and a mechanistic model has been proposed to explain the rod formation. It states that dipole-induced self assembly of nanocrystals is responsible for the formation of the rods. Further, the polarity of the alcohols affects the length of the rods due to interplay between dipole-induced assembly and alcohol-induced colloidal crystalisation. The latter drives the nanocrystals into formation of cubic colloidal particles.

The cubic particles have sizes greater than 100nm and are assemblies of nanocrystals and polymer. Although the particles give monocrystaline-like diffraction patterns, bright and dark field imaging show they are clearly polycrystalline. That means that the incorporated nanocrystals present very good crystallographic alignment.

Electron microscopy shows that the nanocrystals are also oxidised during precipitation and their oxidation is related to their crystallographic alignment. Sheet-like meso-structures present in the composites are composed of hundreds of nanocrystals embedded in a PbSO4 matrix. There is a perfect epitaxial relationship between the sulphate matrix and the nanoparticles. This alignment is partly responsible for the alignment of the nanoparticles in the 3D structures of the

composite. The shape of the nanocrystal/oxide particles may be related to anisotropic oxidation of the nanocrystals.

Finally, solar cells from the nanocrystal: MEH-PPV composites were fabricated and their efficiency was tested. The efficiencies were low and this is attributed to the extended aggregation and oxidation of the PbS nanocrystals. Attempts to prevent these effects via ultrasonication of the composites and use of butylamine were not fruitful. Further experiments using strong Lewis base surfactant molecules were judged to be outside the scope of this project and alternative routes to implementation of PbS nanocrystals in photovoltaics were pursued as described in the following chapters.

**Comment [a.s22]:** Changed after JS request

# 3 Chemistry and electronic levels of PbS nanocrystal films

## *3.1 Synopsis*

This chapter signals a passage from the study of inorganic/organic composites to all inorganic solar cells based on PbS nanocrystal thin films and concerns basic research on the chemistry and energy levels of the latter. After describing the motivation behind this work we continue with a detailed X-ray photoelectron spectroscopy (XPS) study of the surface chemistry of PbS nanocrystal films processed with a number of physical and chemical methods commonly used for solar cell fabrication. Then we focus on measuring the HOMO level of these films using Ultraviolet Photoelectron Spectroscopy (UPS) and discuss the results considering physical and chemical properties.

## *3.2 Motivation*

Chapter 2 closed with presentation of device results from PbS:MEH-PPV and CdS:MEH-PPV composites that had been characterized in detail using TEM methods. Moreover these results follow a trend appeared in the relevant literature over the last 7 years[55, 66-68, 70, 71]: lead chalcogenide: polymer composites do not yield promising photovoltaic efficiencies anywhere close to the 2-3% reported for cadmium chalcogenide composites[49, 56, 59-61, 81]. One possible explanation is that PbS and PbSe nanocrystals do not form a clear type-II heterojunction with common conjugated polymers like MEH-PPV or P3HT due to the very close proximity of the HOMO energies (~ 5.3-5.4 eV) of the two materials[54, 68, 70]. One other reason is that lead

chalcogenide nanoparticles tend to aggregate severely when not passivated with organic ligands[95, 96]. Consequently, although the relevant literature from 2003-2006 was focused on plastic nanocomposites with efficiencies less than 1%[120], it turned later (2007-2009) to the utilization of all inorganic lead chalcogenide nanocrystal films in optoelectronic applications[36, 72-75, 121, 122].

PbS and PbSe nanocrystal films can be made by spin- or dip- coating substrates from nanocrystal suspensions[72, 123]. If the nanocrystals used have narrow size distribution and are free of aggregates then very smooth (<1% roughness) films of closely packed nanocrystals can be made[124]. The electronic structure of these films is determined by four parameters 1) the nanocrystal material 2) the nanocrystal size 3) the organic surfactants 4) the nanocrystals' surface chemistry. These can be realized looking in the schematic of the electronic structure of a nanocrystal array shown in Figure 3.1: the electron and hole energy levels of each nanocrystal of radius $r_{nanocrystal}$ are shifted relative to the levels of the bulk material of energy gap $E_{g\ bulk}$ due to the quantum confinement effect[120]. The nanocrystals are distanced by $L_{ligands}$ due to ligands which also act as energy barriers. However, realistically the energy barriers are of finite height and thus the nanocrystal electronic levels expand outside the nanocrystal volume[27]. If $L_{ligand}$ is small enough the $E_e$ and $E_h$ of adjacent nanocrystals overlap and electronic minibands are formed throughout the solid as in the case of quantum well superlattices[27, 91, 120]. Regardless of the creation of minibands or not, when the $L_{ligand}$ and barrier heights are small enough (or absent) to allow transport of charge carriers from one nanocrystal to the other the film is semiconducting. Generally, carrier transport is considered to occur through a hopping mechanism and the film can be considered a Mott-type conductor[125, 126]. Energy levels $E_{trap}$ lying below the first excitonic level are charge traps which inhibit transport[118]. In

nanocrystals, charge traps are mostly located on the surface of the nanocrystals and originate from dangling bonds and oxide species and their character and density are greatly influenced by the ligands passivating the surface[6, 118, 127].

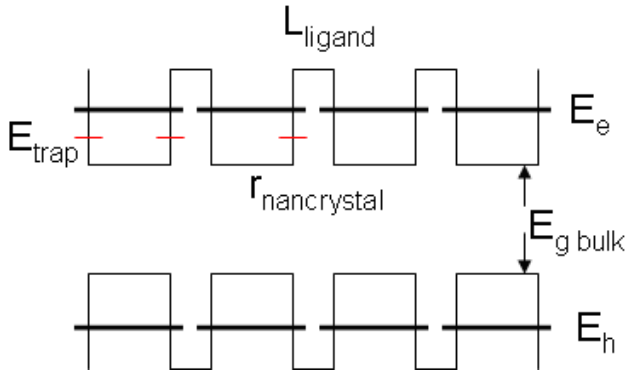


**Figure 3.1 Band diagram of a quantum dot solid (film) in which $r_{nanocrystal}$ is the radius of the nanocrystals, $L_{ligand}$ is the distance between the nanocrystals set by the ligands passivating the nanocrystals, $E_e$ and $E_h$ are the LUMO and HOMO energy levels of the nanocrystals and $E_g$ is the bandgap of the bulk material**

The knowledge of $E_e$ and $E_h$ energy levels relative to vacuum energy is necessary for the design of solar cells incorporating PbS nanocrystals because these levels determine the charge interaction between the PbS nanocrystals and the other parts of the solar cell. However these values have not been experimentally studied in a systematic way and few relevant reports exist. The energy level shift of PbSe nanoparticles as a function of their size has been studied by Jiang et al[54] using cyclic voltammetry (CV). Their results explained why PbSe/ P3HT composites shift from a type-I to a type-II heterojunction character when the size of the particles decreases <8nm: the highest occupied molecular orbital (HOMO) energy level of PbSe nanocrystals becomes <(-5.1eV) which is the HOMO value of P3HT[54]. Also the Silva group in the University of Surrey have used both ultraviolet photoelectron spectroscopy and cyclic voltammetry to study PbS nanoparticles[71, 85]. In their two papers they showed that PbS nanoparticles form a type-II heterojunction with $C_{60}$ and

a type-I heterojunction with PCBM. They also reported two different values on the PbS HOMO levels: -5.7eV from their UPS experiments[71] and -5.2eV from their CV measurements[85]. While Dissanayake et al.[85] did CV to measure the HOMO level of PbS nanocrystals, in an other recent report by Hyun et al[128] CV was used to directly measure the LUMO levels of PbS and PbSe nanocrystals of various sizes. In that work the LUMO level of PbS nanocrystals was found to shift from -3.5 to -4.2eV as the PbS nanocrystals' energy gap changed from 0.73 to 1.7eV[128]. For the same range the HOMO level was found to change much less, from -5.2 to -5eV[128]. Considering the few recent available data and it is no surprise that contrasting values of lead sulphide nanocrystals' HOMO and LUMO energy levels often appear in band diagrams of technology related reports and the reasons of this inconsistency are not clear yet[67, 71, 72, 85, 129]. Still, most technology on this material is based on the theoretical consideration that the HOMO and LUMO levels of this material shift symmetrically from their bulk material values as a function of size because the electron and hole effective masses are approximately equal for this material.[70, 103]

Comment [a.s23]: New ref added

For those reasons and ahead of utilising nanocrystal films in Schottky type solar cells, we performed a detailed characterisation of PbS nanocrystal films using X-ray Photoelectron Spectroscopy (XPS), Ultra-violet Photoelectron Spectroscopy (UPS). UPS was used for measuring the HOMO levels of the films as a function of the processing and the nanocrystal size. With XPS we studied the surface chemistry of the films as a function of two types of processes used in the literature for inducing a Mott-type insulator-to-conductor transition of nanocrystal films. These two processes are 1) thermal annealing of films to evaporate or dissociate the surfactants and 2) exchange of long ligands with shorter ones.

## *3.3 Ligand Exchange*

In almost all published reports on optoelectronic applications of lead chalcogenide nanocrystals, the nanocrystals used are synthesized using oleic acid as the surfactant molecule, and most work is based on the paper of Hines and Scholes on the synthesis of oleic acid capped PbS nanocrystals[26]. The reason for this preference is that the method of Hines and Scholes is: 1) simple 2) easily scalable to gram quantities 3) yields nanocrystals of high quantum yields (>20%) 4) yields nanocrystals of narrow size distribution and well defined excitonic peaks. However as described in **2.2** and **3.2** the long oleic acid molecules are electrically insulating and thus need to be removed/ replaced by shorter ones commonly by primary amines, thiols and alcohols.

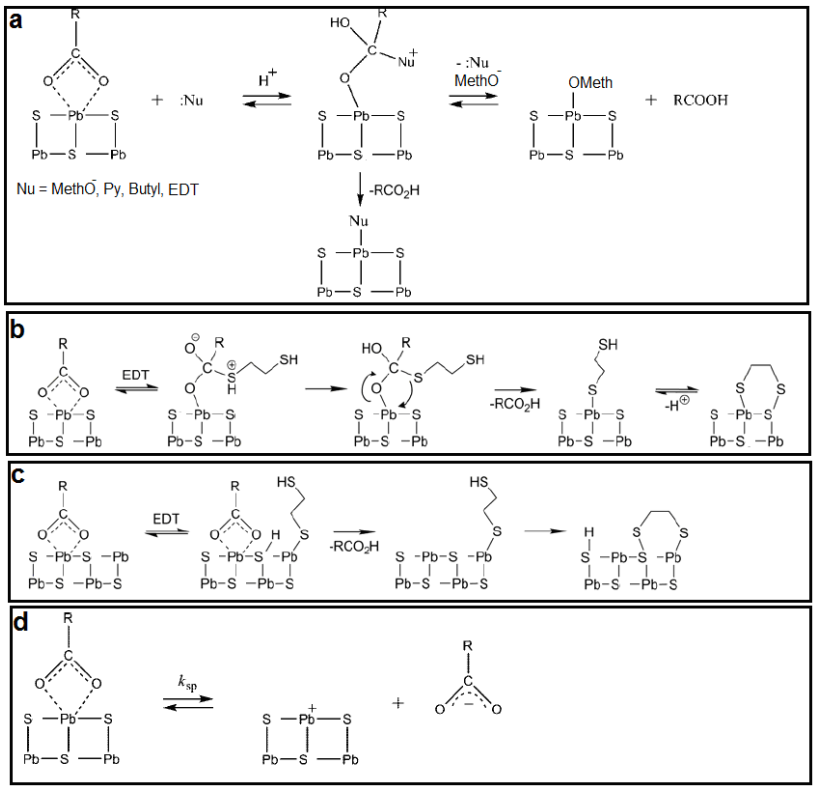


**Figure 3.2 a) oleic acid removal from the PbS surface via nucleophilic attack b) the nucleophilic attack mechanism for EDT c) oleic acid removal via nucleophile dissociation for the case of EDT a) oleic acid removal via increase of solubility product (adapted from Luther et al.[123] and and Law et al.[126])**

When oleic acid-capped nanocrystals are wetted by primary amines, alcohols or thiols- all being and called hereafter nucleophiles- oleic acid is partially or completely replaced by the nucleophiles. The most systematic study of the subject has been done by the Nozik group in NREL Colorado[123, 126] on PbSe nanocrystals and we believe their conclusions can be generalised for the case of PbS nanocrystals as presented in Figure 3.2. There are thought to be two main reaction mechanisms explaining the ligand exchange process: 1) nucleophilic attack 2) nucleophilic dissociation[123, 126]. Both mechanisms presume oleate molecules chelated to single Pb atoms on the surface of the nanocrystals.

The nucleophilic attack, presented in Figure 3.2.a refers to the desorption of oleic acid from the surface of PbS nanocrystals via the intermediate creation of a tetrahedral oleate-nucleophile complex featuring a highly basic oxygen atom. This is followed by subsequent protonation of this oxygen site and the dissorption of the oleic acid leaving the deprotonated nucleophile attached to the Pb atom. This process is enhanced at the presence of a protic solvent e.g. methanol (MethO) and explains the large exchange rates in the latter case relative to cases where non-polar or aprotic solvents e.g. acetonitrile is used. The nucleophilic attack mechanism is shown in greater detail in Figure 3.2.b for the simple case of ethanedithiol (EDT).

The nucleophilic dissocation mechanism is shown in Figure 3.2.c for the case of EDT treatment. This involves the deprotonation and attachment of the nucleophile on the surface of the nanocrystal and the subsequent protonation of the oleate which becomes oleic acid and desorbs. We note that the latest stage of both Figure3.2. b and c can be substituted by nucleophilic dissociation of neighbouring oleate molecules.

Oleate desorption can also happen purely due to the high solubility product of oleate in many of the commonly used nucleophiles. This is shown in Figure 3.2.d

Practically, the ligand exchange process can be performed on both suspended nanocrystals and nanocrystals attached to a surface as shown in Figure 3.3. This Figure schematically shows that due to the small size of the new ligands capping the nanocrystals the latter may merge as the ligand exchange proceeds and this affects their quantum confined optoelectronic properties. As we show in **3.5** this phenomenon is very common and evident in solution-based ligand exchange processes.

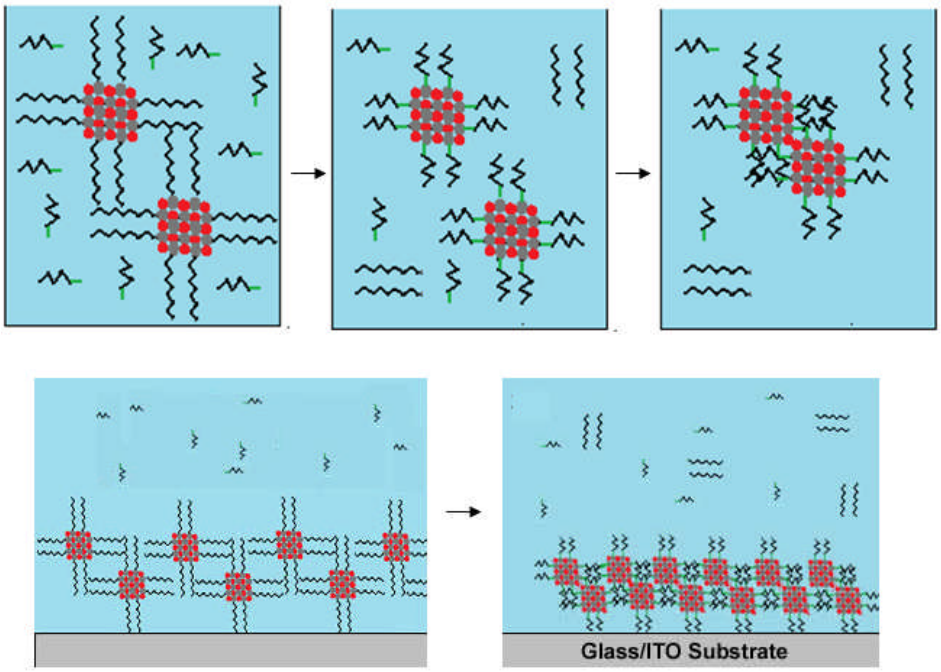


**Figure 3.3 Schematic representation of ligand exchange process on nanocrystal suspension (upper) and nanocrystal film (lower) affecting the interparticle distance**

## *3.4 Methods*

### 3.4.1 Synthesis of PbS nanocrystals

Oleic acid capped small PbS nanocrystals where synthesized with a modified version[96] of the Hines and Scholes method[26]: 0.9 g of PbO was dissolved in a solution of 3ml oleic acid and 6ml 1-octadecene at 150$^{o}$C for 1 hour under a $N_2$ atmosphere. The temperature was lowered to 80$^{o}$C and 400 μl of TMS was injected in to the solution transforming its colour to dark brown. The reaction was instantly

quenched using an ice water bath as described above. The nanocrystals were precipitated from the reaction solution adding excess acetone followed by centrifugation at 4000 rpm for 10 minutes, removal of the supernatant and re-dispersion of the nanocrystals in hexane. The above cleaning step was then repeated twice to ensure adequate cleaning of the nanocrystals. The final nanocrystalline product marked as "OA" was dried overnight and stored in a powder form for further sample preparation.

PbS nanocrystals with an excitonic peak at 920 nm we used the same synthesis and post synthesis methods with the following variations: the synthesis reaction was conducted at 140$^{o}$C using 420 μl of TMS.

### 3.4.2 Preperation of XPS-UPS samples

Solution-based ligand exchange of oleic acid with 1-butylamine (resulting in nanocrystals marked as "Butyl.-solut.") was conducted by dissolving 100mg of OA-capped NCs in 3ml of 1-butylamine and left for two days. Then the nanocrystals were extracted by a precipitation-centrifugation-drying step as described above using acetonitrile instead of acetone.

Nanocrystals marked as "Oxidised" where prepared by further processing of "Butyl. Solute." nanocrystals using an additional precipitation step using anhydrous methanol. The nanocrystals where left as a precipitate in the methanol reach[?] solution for 18 hours before extracting them.

OA- NC, Butyl.-solut. NC and Oxidised NC thin films (~200nm) on ITO covered glass substrate were produced by spin casting from 100mg/ml nanocrystal/toluene solutions. Spin casting was performed via a single step of 800

rpm for 40 sec. Solid state replacement of the oleic acid ligands from butylamine (yielding samples marked as "Butyl.- solid") was performed by immersing OA- NC thin films in a small petri dish filled with a 2:8 volume ratio 1-butylamine: acetonitrile solution for two days, then left drying overnight following a method described by Konstantatos *et al.*[96]. An "Annealed-NC" thin film was prepared by heating a OA-NC thin film in a vacuum oven at 300$^{o}$C for 1hour. All samples were transferred within 24 hours from the glovebox to the XPS-UPS facility of the University of Nottingham inside air-sealed containers and were exposed to air for 2 minutes total upon their loading in the instrumentations sample holder.

### 3.4.3 XPS-UPS

XPS and UPS are based on the photoelectric effect: when a photon of energy hv is incident on the surface of the sample it may excite an electron bound in a state at energy $E_b$ into the surrounding vacuum. If using a photodetector of a known work-function Φ located close to the surface of the material we measure the kinetic energy $E_{kin}$ of the electrons (photoelectrons) emitted from the surface we can calculate $E_b$ as follows:

$$E_b = h\nu - E_{kin} - \Phi \qquad \text{(Equation 3.1)}$$

As stated by their names the two techniques differ in the wavelength used for excitation: X-rays of energies >1MeV are used in XPS and deep ultraviolet light is used in UPS. Because of the high excitation energy of X-rays, the photoelectron spectrum (kinetic/binding energy VS intensity) in XPS contains peaks of photoelectrons originating from core states. The energy of these electrons indicates the element and the chemical substance from which they originated and the spectrum

can be used for qualitative and quantitative chemical characterisation of the sample's surface. The photoelectron peaks are analyzed by deconvolving them in terms of Lorentzian and Gaussian functions[130]. There the Gaussian distribution is the heavier part and Gaussian broadening originates from a number of experimental artifacts like the line shape of X-rays and intrinsic conditions like local chemical and structural inhomogeneities of the sample, thermal excitation processes and the instrumental response[130]. The Lorentzian distribution originates from the limited lifetime of the core hole state[130]. At the end, the peak positions and their relative areas indicate the chemical stoichiometry of the probed surface.

In UPS only photoelectrons originating from shell atomic states and valence bands can be extracted, however the energy of those can be measured with greater accuracy typically 0.1eV. UPS is regularly used to measure the absolute HOMO or work-function energy levels of materials. This is done by fitting straight lines to the onset and offset curves of the UPS spectra. The intersection of these lines with the flat background signal gives: $\Phi$ at the onset and $E_{kin\text{-}HOMO}$ at the offset. The $E_{bind\text{-}HOMO}$ can be then calculated from Equation 3.1.

In our experiments, photoelectron spectra were measured using a Kratos AXIS ULTRA with a mono-chromated Al k$\alpha$ X-ray source (1486.6eV) operated at 15mA emission current and 10kV anode potential for XPS studies and a HeIium (21.2 eV) source for UPS studies. Dr. Emily Smith from the University of Nottingham set up and operated the instrument. Samples were exposed to air for less than five minutes during loading on the instruments holder on which they were grounded via a copper clip making contact with the ITO substrates and the films. In situ argon etching was performed using a Kratos minibeam III ion gun with a stable emission at 10mA. The settings for that were 4kV, in the main chamber pressure was

approximately $3x10^{-8}$ Torr of argon gas and the sample was earthed during this procedure. Raster voltages were applied to scan the etching spot over the surface (slow setting). The etched area was approximately 5mm square at the settings used. The etch crater was not visible to the naked eye.

XPS spectra were calibrated using the C peaks. Then following the methodology of the Sargent group the photoelectron peaks were analysed by de-convolving them in Lorentzian/Gaussian products with the Lorentzian part being <20%[122]. UPS spectra were analysed as described above and in agreement with the methodology reported by Dissanayake et al[71].

### 3.4.4 STEM and Optical absoprtion

TEM samples were prepared by immersing a copper grid in a low concentration NC/toluene suspension for 5sec. TEM was performed by Dr. Rebecca Nicholls on a 3000F JEOL transmission electron microscope equipped with a Fischione high angle annular dark field (HAADF) detector. The inner semi-angle of the HAADF detector was 67 mrad.

The optical absorption spectrum of the NC films was measured using a Varian Cary 5000 UV-visible-NIR spectrometer.

## *3.5 3.5. Results and Discussion*

### 3.5.1 XPS

i) As prepared films

XPS spectra of all as prepared samples show they composed of lead, sulphur, oxygen and C as expected. The $Pb_{4f}$ double peaks, the $S_{2s}$ double peaks and the $O_{1s}$ photoelectron peaks were measured with high spectral resolution to compare the chemical states of the above elements in each sample.

Each of the $Pb_{4f}$ peaks, shown if Figure 3.4, is deconvolved into three sub peaks from three different chemical states as expected according to Konstantatos et al[118]: a peak at 137.8 eV from PbS, a peak at 138.4 eV from $PbSO_3$ and $PbSO_4$ and a peak at 139.1 eV from lead oleate (Pb-oleic acid complex). The $Pb_{4f}$ spectra of all but one of the samples are dominated by the PbS peaks, as they are more intense. They are followed by the oxide states peaks and then the oleate peaks. The only exception comes from the thermally annealed film. Due to this, the above relative intensity rule appears reversed with the lead oleate phase dominating the surface, followed by sulphate phase and PbS. All relative peak intensities for all six samples are presented in Table 3.1. From Table 3.1 it can be seen that the surface chemistry of the nanocrystals depends on their processing.

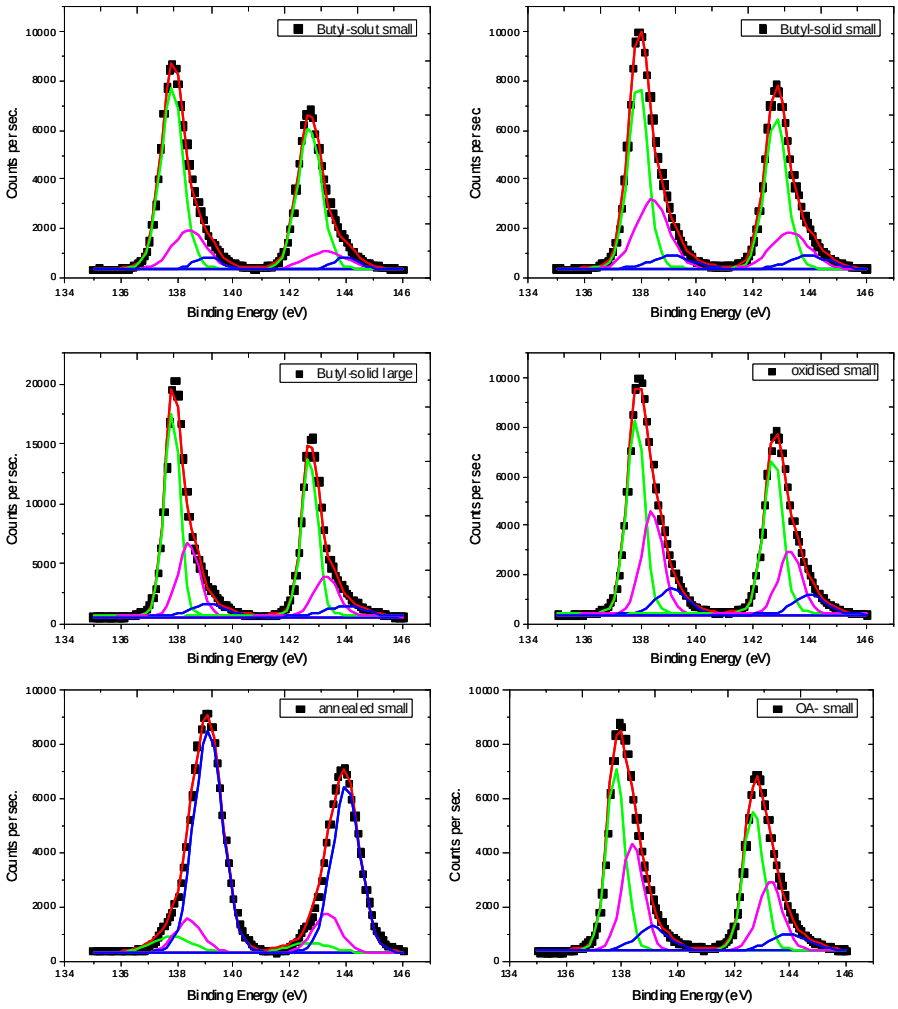


**Figure 3.4 $Pb_{4f}$ spectra of as prepared NC films indicated in legends. Each spectrum has been deconvolved considering $Pb_{4f7/2}$ peaks from PbS at 137.8 eV, from $PbSO_3$ and PbSO4 at 138.4 eV, and from Pb-carboxylate at 139.1 eV , and the respective $Pb_{f5/2}$ peaks.**

Solution based ligand exchange of oleic acid with butylamine results in a decrease of lead oleate on the surface of the nanocrystals compared to those made with oleic acid. This result agrees with previous FTIR results[131]. The process also causes a small decrease of the sulphate state on the surface of the nanoparticles. Similar sulphate reduction is observed for the solid based ligand exchanged

nanoparticles. In this case though, both sulphate and lead oleate are reduced less compared to sample solution based ligand exchanged nanoparticles. When the solution exchanged nanoparticles are precipitated in methanol, the sulphate state peak increases compared to PbS, verifying that methanol treatment oxidises the surface of the nanoparticles. Heat treatment of the nanoparticles at 300$^{o}$C completely alters the "seen" film surface. This process is known for removing oleic acid from the surface of the films decreasing the interparticle spacing and thus improving the film's electric conductivity[71, 126]. Our results however add to this picture indicating that lead oleate complexes are removed from the surface. Thermally induced detachment of the oleic acid ligands is accompanied by etching of the nanocrystal inorganic surface. Dissanayake *et al.* had reported that the main effect of heat treatment was from the formation of PbO[71]. In their analysis however they neither consider sulphate and lead oleate phases nor made a distinction between the latter and PbO.

**Table 3.1**
**Atomic ratios relative to Pb in PbS from the $Pb_{4f}$ spectrum of each sample extrapolated from the $Pb_{4f}$, $S_{3p}$ and $O_{1S}$ high resolution spectra**

| | $Pb_{4f}$ | | | | $S_{2p}$ | | | $O_{1s}$ | | | |
|---|---|---|---|---|---|---|---|---|---|---|---|
| Sample | PbS | Oxides | Pb-oleate | Pb | PbS | polysulphide | S | PbSO3 | PbSO4 | PbO | Hydroxyl. O |
| B-solut small | 1 | 0.32 | 0.09 | n/a | 0.85 | 0.13 | n/a | 0.96 | 0.39 | 0.04 | |
| B-solid small | 1 | 0.60 | 0.15 | n/a | 0.93 | 0.17 | n/a | 1.20 | 0.43 | 0.13 | 0.06 |
| B-solid large | 1 | 0.5 | 0.14 | n/a | 1.06 | 0.14 | n/a | 0.89 | 0.11 | 0.02 | 0.08 |
| Oxidised small | 1 | 0.63 | 0.21 | n/a | 1.03 | 0.18 | n/a | 1.34 | 0.22 | 0.13 | 0.06 |
| Annealed small | 1 | 1.41 | 10.01 | n/a | n/a | n/a | n/a | 26.56 | 1.16 | 1.78 | 2.99 |
| OA small | 1 | 0.68 | 0.23 | n/a | n/a | n/a | n/a | 1.65 | 0.25 | 0.12 | 0.18 |
| Etched B- solid small | 1 | n/a | 0.12 | 0.82 | 0.54 | n/a | 0.35 | n/a | n/a | n/a | n/a |

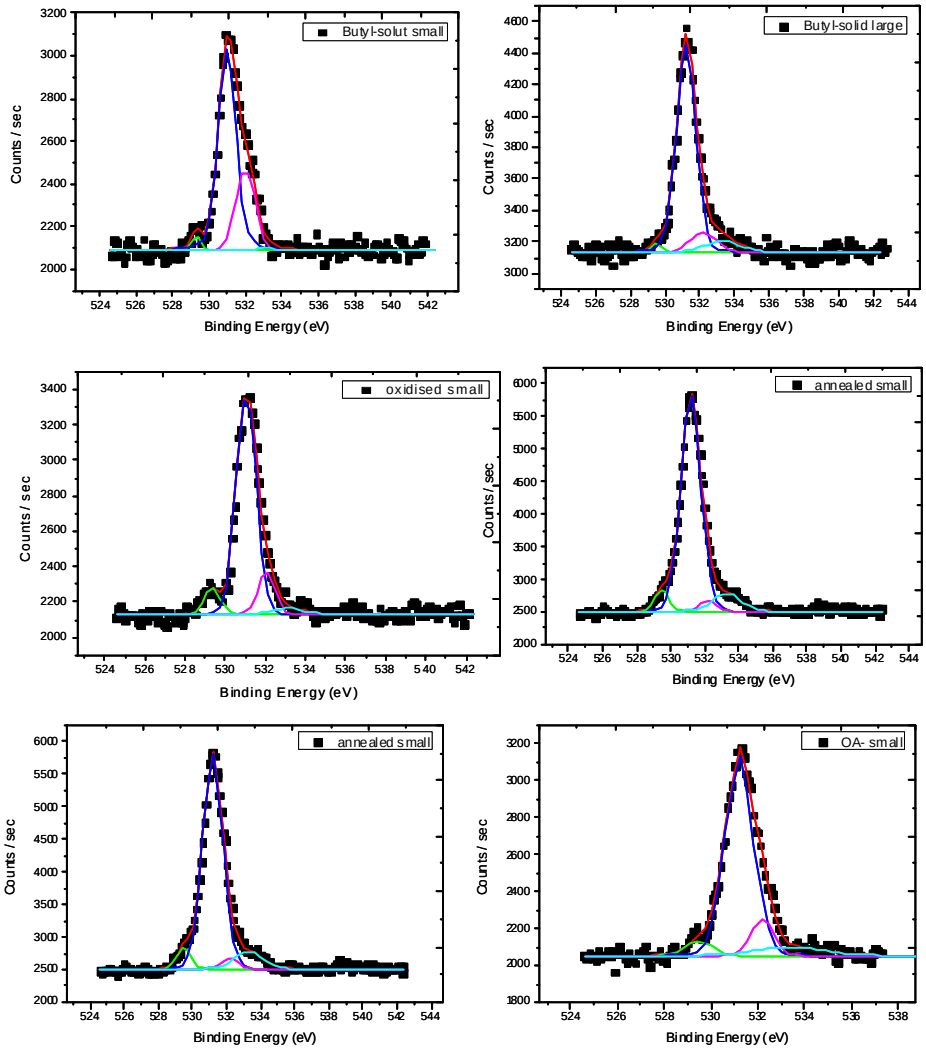


**Figure 3.5 $O_{1s}$ spectra of as prepared NC films indicated in legends. Each spectrum has been de-convolved considering peaks from PbO at 529.3 eV, from $PbSO_3$ at 530.8, $PbSO_4$ at 531.8 eV, and from hydroxylated O at 533.3 eV.**

The oxide states on the surface of the films are difficult to resolve from the $Pb_{4f}$ peaks. To do so we examine the $O_{1s}$ spectra which are shown in Figure 3.5. These spectra were analysed similarly to Klem *et al.*[122] by considering four different compounds: PbO, $PSO_3$, $PbSO_4$ and hydroxylated O from the oleic acid, each with characteristic $O_{1s}$ peaks at 529.3[132], 530.8[122], 531.8[132] and 533.3eV[133] respectively.

The spectra shows that $PbSO_3$ is the main oxygen containing compound. It is interesting that both butylamine treated small nanocrystal films have increased $PbSO_4$ relatively to $PbSO_3$, an effect which has also being observed on OA capped PbS nanoparticles treated with ethanedithiol. Since both $Pb_{4f}$ and $O_{1s}$ analysis show that the total oxide species concentrations for butylamine treated samples compared to the OA-capped particles have been decreased, we attribute the increase of $PbSO_4$ relative $PbSO_3$ to further oxidation of the $PbSO_3$ states upon the films' brief exposure to air prior to insertion into the instrument's vacuum chamber. Oleic acid is known to inhibit oxidation of PbS nanoparticle's surface from air and moisture[134]. All treated films have less OA and thus they are more vulnerable to oxidation. Finally the quantitative analysis shown in Table 3.1 verifies that methanol treatment of the nanocrystals results in an increase of oxide concentration on their surface. We note that in the annealed sample O atomic concentration relative to Pb in PbS is 25 times higher compared to the other samples, attributed to oxidation of the surface upon thermal decomposition of oleic acid. We also note the increase of the hydroxylated $O_{1s}$ peak for the annealed nanocrystals compared to the rest samples. This confirms that heat treatment resulted in the accumulation of carboxylic groups on the surface of the film.

It was unexpected that butylamine treatment would promote transformation of PbO and $PbSO_3$ to $PbSO_4$ while successive methanol would counter the effect. However, these results are verified by analysis of the S peaks. The S spectra were analysed considering possible presence of PbS, polysulphide species, $PbSO_3$ and $PbSO_4$ with peaks at 160.9, 164, 165.7, 168eV respectively [122]. Each of these was followed by its satellite at 1.2 eV separation and each pair had an area ratio close to 2:1. The quantitative data on S in PbS gives a 1:1 ratio between Pb and S in PbS

which strongly supports the validity of the quantitative analysis. Figure 3.6 compares the S spectra for butyl-solid treated nanocrystals and annealed nanocrystals. Both have significant $PbSO_3$ components; however the first have a much stronger $PbSO_4$ signal compared to the second. Finally, we note that the OA capped nanoparticles and annealed nanoparticles have a relatively weak S signal, an effect attributed to the strong organic contamination of both materials' surfaces. The surfaces' organic contamination and surface oxidation triggered us to clean film's surfaces in-situ using argon sputtering.

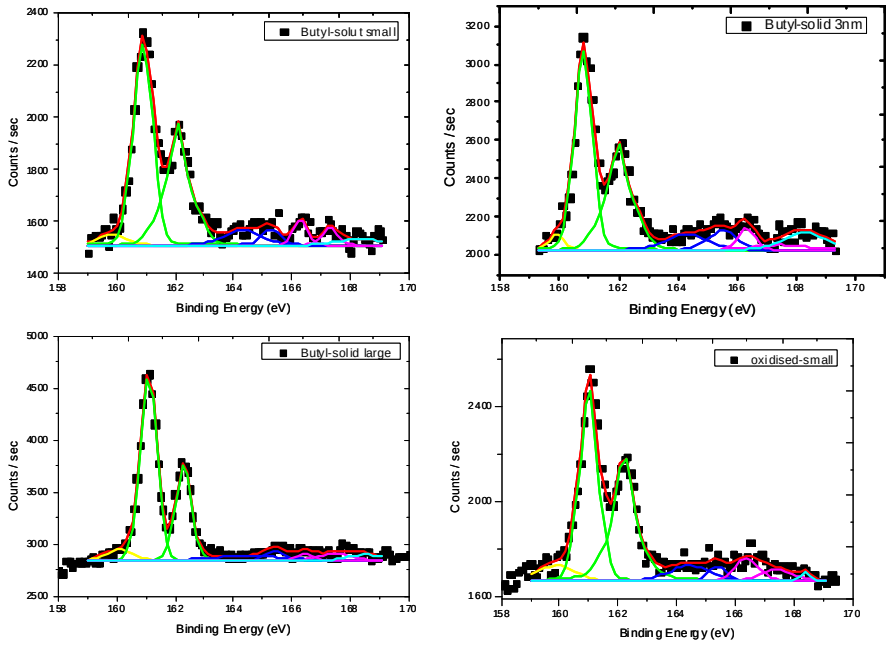


**Figure 3.6 $S_{2p}$ spectra of as prepared NC films indicated in legends. Each spectra has been deconvoluted considering $S_{2p3/2}$ peaks from PbS at 160.9 eV, from polysulphides at 163 eV, from $PbSO_3$ at 165.7 eV, $PbSO_4$ at 168 eV. Each peak is followed by the respective $S_{2p}$ peak separated by 1.2eV.**

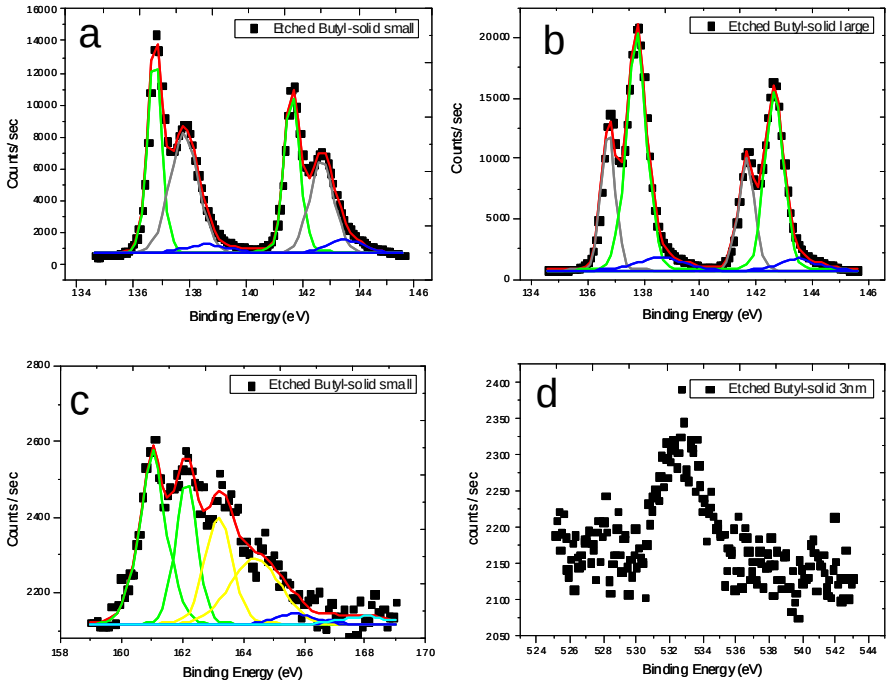


**Figure 3.7 a and b) $Pb_{4f}$ spectra of two etched samples showing creation of elemental Pb on the surface identified by a $Pb_{4f7/2}$ peak at 136.8 eV. Peaks at 137.8 and 139.1 correspond to Pb-carboxylate. c) $S_{2p}$ spectrum of an etched sample showing creation of elemental sulphur identified by a $S_{2p3/2}$ peak at 163.2 and its doublet. The other doublets correspond to PbS, $PbSO_3$ and $PbSO_4$. d) $O_{1s}$ spectrum of an Ar etched sample showing a weak $O_{1s}$ peak.**

ii) Etched films

The surface chemistry of all films after etching by Ar ions changed drastically, specifically oxygen contamination was almost eradicated, the nanocrystals were etched and carbon contamination was reduced. Oxygen removal from the films is evident from the very weak, almost disappeared $O_{1s}$ peak. From this we conclude that the oxygen content of the surface is insignificant for etched samples. In the same line, sulphate and lead-oleate components are absent from all $Pb_{4f}$ spectra of all etched samples. These are now composed of elemental Pb, PbS, and lead-oleate peaks. For

all but the large nanocrystal samples the elemental Pb component is ~0.8 times the PbS component. The $S_{2p}$ spectra of all samples are weak. This is attributed to the high energy expansion of the Pb peaks neighbouring with the $S_{2p}$ and not to disappearance. The S peaks seen in the general spectra get stronger after etching. Back to the $S_{2p}$ spectra, these show a presence of PbS, polysulphide and not surprisingly elemental sulphur. The $PbSO_3$ and $PbSO_4$ peaks are very weak as shown in Figure 3.7.

All the above data point to the conclusion that argon ions etched the inorganic surface of the films, destroying the organometallic and inorganic oxide species. Also the atomic concentration of elemental lead leaves no doubt that argon also etched part of the PbS core of the top surface nanocrystals. This is discussed in greater detail below following the UPS results.

### 3.5.2 UPS

Ultraviolet photoelectron spectroscopy was used to study how the HOMO-level of the nanocrystals changes as a function of the particles' organic passivation and the changes in the quantum confinement. The absorption spectra from the films is shown in Figure 3.8.a. It shows that OA-capped and Butylamine-solid capped nanocrystals retain a distinct first excitonic transition indicating that the nanoparticles are monodisperse in size and well separated retaining their individual band structure. Butylamine capped nanoparticles with ligand exchange done in solution lose their excitonic peak. This originates from aggregation of the nanoparticles in solution due to the short length of butylamine. As the Sargent group has shown before, the nanoparticles self-assemble across 1 dimension forming chains[96]. We have verified their observation, the STEM micrograph in Figure 3.8.d shows this linear self

assembly of the nanoparticles in contrast to the well dispersed OA capped nanocrystals shown in Figure 3.8.c. The absorption onset shifts further to the red for the annealed film with simultaneous broadening of the excitonic peak. Again this means that necking of the nanoparticles takes place as the OA is carbonylized and/or removed upon annealing. The methanol-processed butylamine capped nanoparticles aggregate further. We expected that considering the mechanisms described in Figure 3.2. Finally the 6nm nanoparticles have a large size distribution and their absorption onset extends further than the rest of the samples. We expected the ionisation potential of the films to shift to lower values as their absorption onset is red shifted as shown in Figure 3.8.a.

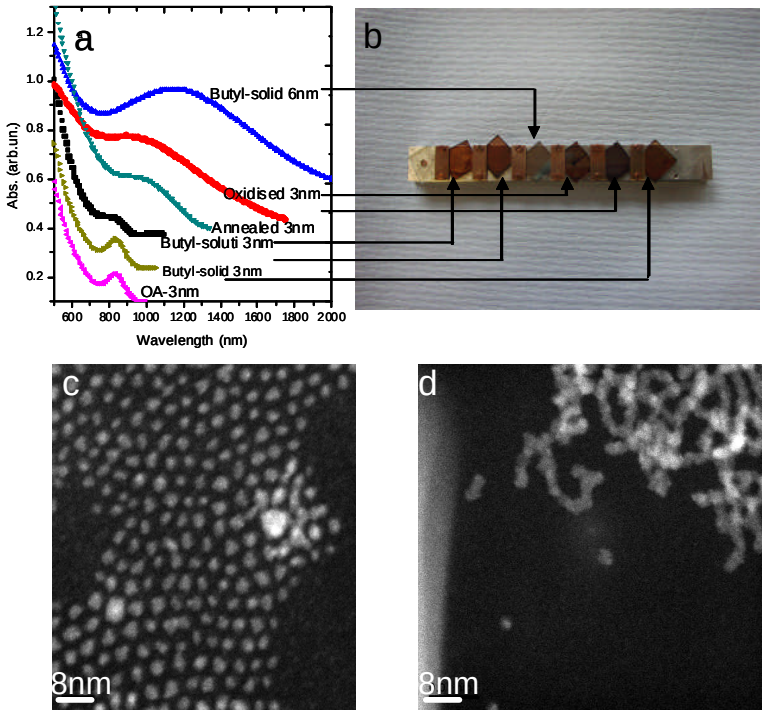


**Figure 3.8 a) Absorption spectra of nanocrystal films on ITO/glass b) Photograph of films loaded on the XPS-UPS holder. The films are grounded with copper clips c) STEM micrograph of OA-small nanocrystals d) STEM micrograph of butyl-solution small nanocrystals. The nanocrystals self assemble forming linear structures.**

The HOMO-level of the films was calculated by measuring the kinetic energy onset and offset of the photoelectrons emitted upon UV illumination using the two line method[71]. The onset corresponds to the instrument photomultiplier work function and the second to the kinetic energy of the photoelectrons emitted from the material's lowest HOMO level. The UPS spectra for the as prepared butyl-solid and the annealed films are shown in Figure 3.9.a. The onset regions are shown in Figure 3.9.b. The onset kinetic energy is identical for all samples, meaning the work function of the detector was stable during the course of the study (6.5eV). Figure 3.9c shows the offsets for these two samples. The high slope components of the offsets are used to extrapolate the kinetic energy of the electrons originating from the HOMO levels of the films[71]. For the two samples shown, the offsets are 20.6eV and 20.4eV ±0.1eV. Thus applying Equation 3.1 and knowing that the photon energy is 21.2eV the HOMO levels were calculated to be 5.9eV and 5.7eV ±0.1eV for the butyl-solid and annealed samples respectively. The differences are small but measurable.

Considering previous results in the literature, these values are satisfying. From the absorption spectra we calculate that the energy of the first excitonic transition of the butyl-solid nanoparticles is 1.4eV. Dissanayake *et al.* reported that the ionisation potential of nanocrystals with bandgap (Eg) of 1eV results in a HOMO level of 5.7eV [71]. The 0.4eV Eg difference between the exciton energies in our nanocrystals and those of Dissanayake et al[71] should be shared equally on the HOMO and LUMO shifts of the nanoparticles according to a 4-band effective mass model for PbS nanocrystals [103]. Thus the 0.2 eV difference between the two corresponding ionisation potentials is consistent with the theoretical model.

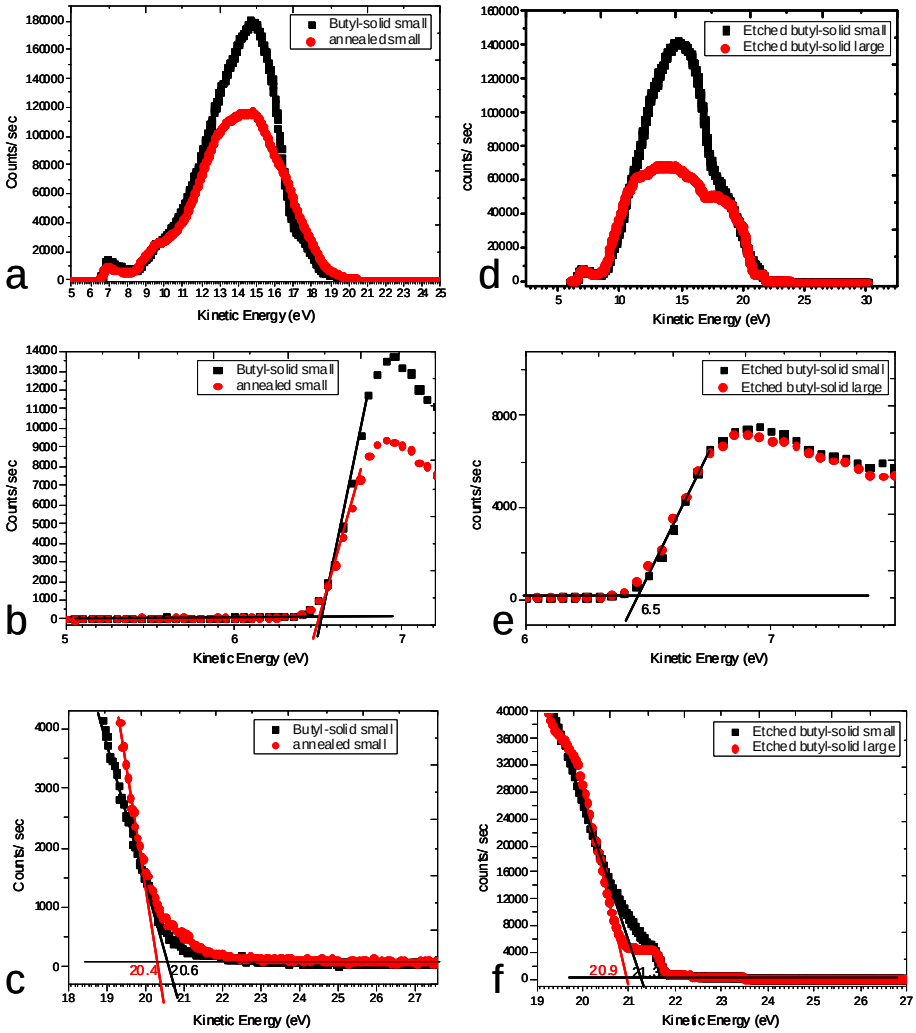


**Figure 3.9 a) Two typical UPS spectra of two studied materials b) Magnified onset of the spectra shown in (a), and identification of the photodetector's work-function Φ=6.5 eV via the two line method c) Magnified offsets of the spectra shown in (a) and measurement of the kinetic energy of the HOMO level electrons via the two line method d,e,f) The same as a,b,c for two etched samples. The energy step at $E_{kin}$~20-21eV is considered a measurement artefact because it is has been observed also in measurements from clean ITO surfaces.**

The 0.2eV difference between the butyl-solid and annealed samples also follow the energy gap shift shown in the absorption spectra, considering that the annealed particles' absorption onset goes beyond 1200nm. Excluding the oxidised

sample, the remaining as-prepared materials measured HOMO energy levels are shown in Table 3.2 and follow the qualitative progression expected from the absorption spectra. The oxidised sample gives a 5.8 eV HOMO value which fits with the rest of the data considering the position of its excitonic peak but not of its absorption onset. Although we can not explain this result we do not attribute it to an experimental artefact because the oxidised sample has a large HOMO value compared to the other samples.

**Table 3.2**
**HOMO levels of films calculated from UPS spectra. Experimental error is ±0.1 eV.**

| Sample | As prepared (eV) | Ar- etched (eV) |
|---|---|---|
| Butyl-solut. 3nm | n/a | 6.5 |
| Butyl-solid 3nm | 5.9 | 6.5 |
| Butyl-solid 6nm | 5.3 | 6.1 |
| Oxidised 3nm | 5.8 | 6.4 |
| Annealed 3nm | 5.7 | 6.4 |
| OA- 3nm | n/a | 6.6 |

Examples of the UPS spectra after etching are shown in Figures 3.9.d,e,f. for the Butyl-solid small and large nanoparticles. All argon etched films have a much higher ionisation potential as shown in Table 3.2 compared to the ones before etching. These values are beyond theoretical expectations considering the ex-situ optical and morphological data. Possible answers should be related to the effects of etching which we examined with the XPS: we showed that argon ions etched almost entirely the oxide species on the film's surfaces and also etched part of the PbS phase. If true, the second explains the high electron affinities seen in UPS because etching of the nanoparticles mean a decrease in their size and thus blue shift of their energy gaps and electron affinities. The etching induced shift of the nanoparticles' electron affinities

**Comment [a.s24]:** clarified

we report can be used in optoelectronic applications, like in the creation of quantum well structures.

The progression of the measured ionisation potential for all samples follows the morphological changes of the nanoparticles indicated by the absorption spectra. More importantly these results show that ultraviolet photoelectron spectroscopy can be used to study quantum confinement of PbS nanoparticles, and detect changes as subtle as the ones created by the organic molecules passivating the surface of the nanoparticles. The 0.6eV difference between the Butyl-solid-3nm and the Butyl-solid-6nm particles demonstrate that.

## *3.6 Conclusions*

In conclusion, we performed detail investigation of the surface chemistry and the HOMO-levels of PbS nanoparticles. We showed how these depend on various physical and chemical treatments of nanocrystals. The main findings regarding the nanocrystal chemistry are the following: thermal treatment results in accumulation of lead-oleate on the surface of the nanocrystals. It also results in heavy oxidation of the nanocrystals. Thus thermal treatment is not recommended for applications because it creates a “dirty” film surface and also oxidation is generally considered bad as oxide states act as charge traps. Butylamine treatment results in an increase of the oxide concentration relative to as-grown OA capped nanocrystals mostly because of PbO formation. It also promotes formation of $PbSO_4$ relative to $PbSO_3$. The latter is not desirable as $PbSO_4$ acts as a deeper trap state with a longer lifetime compared to $PbSO_3$[118, 122]. Methanol treatment results in further increase of the oxide states, mostly

PbO. However, it promotes the formation of $PbSO_3$ which is good for optoelectronic applications[122]. It also results in the removal of oleic acid and aggregation of nanocrystals if following a butylamine treatment.

It was also demonstrated how UPS can be used to detect changes on the ionisation potential of PbS nanocrystals as a function of nanocrystal processing. We showed that solid-based ligand exchange alters little the quantum confinement compared to that observed after solution-based ligand exchange. We also showed that the measured HOMO level dropped from 5.7 to 5.3eV when the film's absorption onset changed from 1.3 eV (950 nm) to 0.6 eV (2000 nm). This may explain the range of HOMO values for PbS nanocrystals in the literature. It also indicates that the electronic structure of a nanocrystal film will be highly inhomogeneous if the film is made with nanocrystals of broad size distribution. Finally, etching of the films with Ar atoms may clean the nanocrystal surface from oxides but it also cause a huge increase of the surface's work function due to etching of the nanocrystals. This means that Ar etching creates a potential barrier at the surface of the nanocrystal films.

# 4 PbS nanocrystal films- Schottky type solar cells

## *4.1 Synopsis*

This chapter examines the utilisation of PbS nanocrystal films, fabricated via a dip coating method, in efficient photovoltaic Schottky junctions. After a brief introduction on the Schottky junction formation mechanism the chapter focuses on the optimisation of the dip-coating fabrication method and understanding of the photovoltaic properties of the junctions as a function of fabrication parameters and device aging. Current-voltage and external quantum efficiency measurements are compared with the literature aiming to secure an experimental background for the further advancement of these solar cells following in Chapter 5.

## *4.2 Motivation*

Lead chalcogenide nanocrystal/ metal Schottky junctions have been intensively developed over the last 3 years and present some of the highest photovoltaic efficiencies (3.1%)[135] among all types of nanocrystal-based solar cells[72, 74, 120]. In addition, compared to all plastic and hybrid (organic/inorganic) solar cells, all- inorganic $PbS_xSe_{1-x}$ (x=0-1) nanocrystal Schottky cells present the highest power conversion efficiencies of infrared light: 4.2% and 2.4% at 1 micron and 1.5micron wavelengths respectively for PbS cells compared to 0.9% and $4*10^{-4}$% respectively for other the other types of nanostructured cells[120].

The above result is particularly impressive considering that the nanocrystal films used in the Schottky devices are ~200nm thick and absorb only 10-60% of the incident light depending on wavelength[120]. The good power conversion efficiencies of these devices originate from their high external quantum efficiencies (up to 90%) as opposed to the observed $V_{oc}$ (typically <0.4V) and FF (below 50%) which are lower than most competing cell architectures[120]. Recent reports also indicate realisation of multiple exciton generation in working devices[30]. It is believed that the external quantum efficiencies of these devices originate from their high electron and hole mobilities (~$10^{-3}$ $cm^2$ $V^{-1}$ $s^{-1}$)[121] and carrier diffusion lengths (100-400nm)[73, 121] which allow sufficient extraction of both majority and minority carriers from the film and more specifically from the depletion region of the Schottky barrier which typically is 150nm[73, 121] wide when using Al as the top electrode.

Most of the above literature data and technological advancements refer to thiol passivated PbS nanocrystal films and are a great improvement over initial experiments with amine passivated films ( $V_{oc}$<0.3V, $PCE_{IR}$ <1%, $\mu=10^{-5}$ $cm^2$ $V^{-1}$ $s^{-1}$)[136, 137]. It is believed that thiols improve the electronic properties by reducing oxide species, particularly $PbSO_4$, which as deep surface trap states on the surface of nanocrystals[118, 127, 137]. Up to August 2009, the are two leading research groups in the field following different methods on fabricating their films. The Sargent group fabricates amine capped PbS nanoparticle films via spin-casting method then replaces amines with thiols during a solid state ligand exchange[121], while the Nozik group focuses on PbSe nanocrystal film fabrication using a layer-by-layer dip coating method which is also based on a solid state exchange of oleic acid with thiols[126]. We decided to focus on the second method for making PbS nanocrystal films for solar cells considering it to be open to optimization for the case of PbS, compatible with

our desire for working on three-dimensional film structures for tandem cells (as will be examined in Chapter 5), and finally more attractive for potential future scaled-up applications in industry.

**Comment [a.s25]:** added after Js request

### 4.2.1 Nanocrystal/metal Schottky junction

When a p-type semiconductor of valence and conduction bands $E_v$ and $E_c$ and work function $w_p=E_{Fp}$ comes into contact with a metal of work function $w_m=E_{Fm}<E_{Fp}$ the Fermi levels of the two materials $E_{Fp}$ and $E_{Fm}$ line up as a condition for the establishment of thermal equilibrium[4, 138]. This corresponds to bending of the vacuum level $E_{vac}$ at the materials' interface and is achieved by flow of electrons from the metal to the semiconductor so as to bend $E_v$ and $E_c$ at the interface where the semiconductor and metal become negatively and positively charged respectively. This creates an electrostatic field capable of separating electrons and holes with the electrons travelling to the metal contact and the holes away of it.

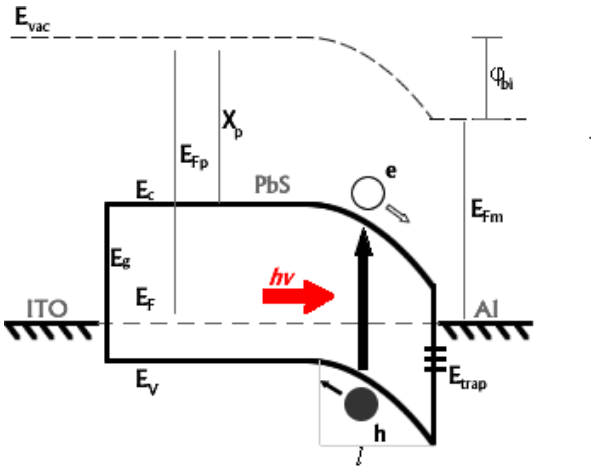


**Figure 4.1 Schottky barrier between a p-type PbS film and the top Al electrode in a ITO/PbS/Al solar cell**

Assuming an ideal interface with no trap states, the built-in electrostatic potential energy step $\varphi_{bi}$ fielding the device will be equal to the total change ($w_m$-$w_p$) of $E_{vac}$ between the two sides of the interface and the electrostatic field F at the interface will be $1/q(\nabla Evac)$. The potential difference $V_{bi}$= $\varphi_{bi}$/q is shared between both sides of the interface according to Poisson's equation: $\frac{d}{dx}(\varepsilon_s F) = q\rho(x)$ where x is the distance from the interface, $\varepsilon_s$ is the local dielectric permittivity and ρ the local charge density. Because the metal can generate a very large charge density at the interface virtually all the potential difference drops at the semiconductor. The semiconductor region required for this is called the depletion region and is net negatively charged for the case discussed here. The $E_v$ and $E_c$ in this region are changed parallel to $E_{vac}$ so the energy gap $E_g$ and electron affinity $\chi_p$ of the semiconductor are invariant. The length l of the depletion region is given by the relationship

**Comment [a.s26]:** changed

$$l = \sqrt{\frac{\varepsilon\varepsilon_o(\phi_{bi}V)}{qN}}$$

Where ε is the static dielectric constant of the nanocrystal, $\varepsilon_o$ is the dielectric permittivity of vacuum, V is the applied bias and N is the free carrier density in the nanocrystal film. Using temperature dependent capacitance-voltage and current-voltage measurements the values of the above have been measured for PbS nanocrystal films with good photovoltaic efficiency (>1%) and are: N≈$10^{16}$$cm^{-3}$, ε≈17, $\varphi_{bi}$≈ 0.3eV and l=150nm[72, 73]. We note that for PbS nanocrystal films the experimentally measured $\varphi_{bi}$ is up to 0.6V smaller than the theoretical prediction $w_m$-$w_p$ due to interfacial charge traps $E_{trap}$ and an insulating interfacial layer which can be attributed to oxidation, surfactants and nanocrystal surface states[72].

The small open circuit voltages and fill factors, <0.44Volts and <0.48 respectively for the best reported PbS devices[121, 135], limit the power conversion efficiency of the nanocrystal Schottky solar cells. Another limiting factor is that in Schottky type junctions $V_{oc}$ can not be more than $E_g/2$[4, 75]. A third drawback is that in ITO/PbS/Al solar cells the largest electric field and therefore most efficient exciton dissociation occurs at the back Al contact, whereas most excitons are generated by the ITO contact through which the light enters the device. Thus holes created at the PbS/Al interface may recombine with electrons travelling from the back to the front contact[120]. A consequence of the above is that for layers above 200nm thick the interplay between light absorption and carrier recombination turns in favour of the latter and that decreases the power conversion efficiency of the cell[120]. However, 200nm thick PbS films may absorbs small portion of incident IR light, e.g. ~ 41% and 14% for 950nm and 1550nm light respectively, and this limits the cell's photocurrent despite huge internal quantum efficiencies of up to 90%[74, 120].

There are two methods reported for fabricating PbS films for Schottky type-photovoltaics: spin coating and dip coating. The first is faster but often results in films with cracks and rough surfaces. Cracks may cause short circuiting in the solar cell and this is tackled by applying two spin casting steps with the second intended to cover cracks and pinholes created during the first step[121]. We have tried making cells with spin casting but always found that the cells formed short circuits and the results are not presented. However, we were able to fabricate working solar cells using a recently reported dip coating method[123].

### 4.2.2 The Dip coating method

A layer-by-layer dip coating method for the fabrication of high quality semiconducting nanocrystal films has been recently reported for the case of PbS, PbSe and CdSe nanoparticles[123]. It is based on the deposition of monolayers of oleic acid capped nanoparticles on a flat substrate via dipping the latter in thin hexane/nanocrystal suspensions (0.005g/ml) followed by a ligand exchange process of the long and non-polar oleic acid with a shorter polar ligand like ethylenedithiol (EDT) by dipping the substrate in an EDT/acetonitrile solution (0.01M EDT). EDT may replace oleic acid via the mechanisms discussed in **3.3** of Chapter 3. The ligand exchange process is schematically described in Figure 4.2. The ligand exchange step reduces the inter-particle spacing in the film making it semiconducting, and transforms the surface of the nanoparticles from non-polar to polar making them insoluble in hexane. This last effect allows deposition of successive layers up to the desired film thickness.

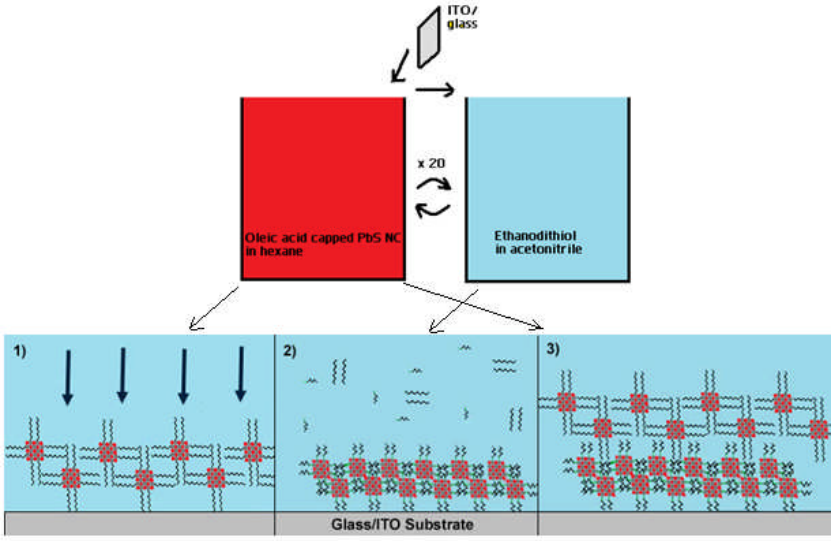


**Figure 4.2 Schematic description of the dip-coating method for fabrication of PbS nanocrystals films.**

The advantages of this method are: a) the ligand exchange occurs on nanoparticles immobilised on the film and thus it is not accompanied by uncontrolled aggregation of nanoparticles[96] as in the case of solution based ligand exchange methods examined in Chapter 3, b) the method offers fine control over film thickness c) it is easily scalable d) EDT molecules are believed to passivate some surface charge-trap states improving the film's carrier mobilities[121] and photovoltaic performance. A disadvantage of the method is that is slow compared to spin casting.

## *4.3 Experimental Methods*

### 4.3.1 PbS nanocrystal synthesis/processing

PbS nanocrystals with an excitonic peak at 780nm were synthesized as described in **3.4.1** with the following modification: 380μl of TMS were used. Compared to 3.4.1 a slightly different post-synthesis step was followed as this is described in the literature on PbS Schottky cells[75, 121]: the nanocrystals were precipitated from the reaction solution adding a 1:1 volume ratio mixture of ethyl acetate and methanol followed by centrifugation at 4000 rpm for 10 minutes, removal of the supernatant and re-dispersion of the nanocrystals in hexane. The above cleaning step was repeated twice to ensure adequate cleaning of the nanocrystals.

To make PbS nanocrystals with an excitonic peak at 920nm we used the same synthesis and post synthesis methods with the following variations: the synthesis reaction was conducted at 140$^{o}$C using 420μl of TMS.

### 4.3.2 Device fabrication

We fabricated devices composed of glass/ITO/PbS films/Al with the geometry, glass/ITO substrate preparation and Al thermal-vapour deposition as described in **2.4.7** and Figure 2.3.

**Comment [a.s27]:** Changed to avoid repetition

Thin films of PbS nanocrystals were fabricated via the dip-coating method described elsewhere[2] using 0.007g/ml nanocrystal/hexane solutions and a second 0.01M ethyldithiol in acetonitrile solution. For depositing a ~6nm monolayer, etched ITO/glass substrate was vertically dipped by hand (holding the substrate from its corners) in the NC solution, then slowly (~0.3cm/sec) retracted out of the solution and left to dry for 20sec. The film was subsequently dipped quickly in to the EDT solution for 3sec then retracted quickly (~1cm/sec) and left to dry for 30sec more. The above process was repeated to increase the film thickness. On each repeat the device was rotated by 90 degrees.

### 4.3.3 Device Testing and Repeatability

Device I-V testing at dark and 80mW/cm$^2$ AM.1.5 illumination was conducted as described in **2.4.8**. Each of the I-V results reported was verified for at least three working devices in total from two different substrates. Results from fully optimised 200nm PbS film devices reported in **4.4.2** originate from measurements on six devices from two different substrates.

For spectral response measurements (EQE Vs wavelength) a Keithley 64585 picoammeter was used to record the photocurrent of the devices at short circuit conditions under different wavelengths. Monochromatic illumination in the 400nm-1800nm optical range was provided by a Newport 50W Quartz Tungsten Halogen

(model 101-70527) coupled to a Cornerstone™ 130 1/8m motorized monochromator. Each of a 400nm, a 650nm and a 1000nm long-pass optical filter was placed in front of the monochromator's exit port during measurements at each of the 400-680nm, 680-1100nm, 1100-1800nm optical ranges respectively. Light was focused, over illuminating the device pixels using a set of confocal lenses. Illumination spot-to-device area mismatch was considered when calculating EQE. Light intensity was measured using two calibrated Newport diode photodetectors: a Si detector for 400nm-1100nm optical range and a Ge detector for the 1100-1800nm range. To calculate $I_{sc}$ from the EQE measurements, we used the AM1.5 1 sun standard data provided in Renewable Research Data Centre of NREL laboratories website[3] considering light intensity mismatch for 80mW/cm$^2$

**Comment [a.s28]:** Does this make sense now?

### 4.3.4 Optical absorption

Optical absorption measurements of nanocrystal/hexane solutions and thin films were conducted using a Varian Cary 5000 UV-visible-NIR spectrometer using quartz cuvettes for the solutions and ITO/glass substrates for films. All nanocrystal spectra were referenced against blank samples located at the reference port of the instrument.

## *4.4 Results and Discussion*

### 4.4.1 The effect of EDT and optimization

We started fabrication of solar cells using 0.4M EDT in acetonitrile solution. The purpose of this was to investigate whether high concentrations of EDT, compared

to the 0.01M concentration used by Luther et al, are beneficial for the optoelectronic properties of the PbS films. The I-V curves in the dark and under illumination of a 200nm PbS film device with ITO and Al as electrodes are shown in Figure 4.3. It is obvious that the device exhibits no photovoltaic effect. Although the device is not short circuited and under applied bias behaves as a photoconductor, its I-V response is almost linear with little difference between forward and reverse bias. At this point we define forward bias as the application of a positive voltage at the ITO electrode in agreement with previous reports and will use this definition for the remaining of the Chapter.

The lack of observed rectifying behaviour implies the absence of a significant Schottky barrier at the nanocrystal/Al interface. We considered three possible reasons causing that: 1) necking of the nanocrystals during the ligand-exchange process and subsequent loss of quantum confinement and reduction of the film's $E_g$ 2) presence of interface trap states attributed to surfactant molecules and/or charge trap states on the nanocrystals' inorganic surface 3) insufficient p-type doping of the nanocrystals.

All three of the above mechanisms can be the result of high EDT coverage of the nanoparticles: EDT is a small molecule and replacement of oleic acid with EDT is generally accompanied by a red-shift of the nanocrystals' absorption onset and excitonic peak[123], the ligand exchange process may leave lead oleate molecules on the surface of the films and EDT reduces the majority (hole) carriers concentration in PbS nanocrystal films[121]. As an obvious next step, we fabricated films varying the duration time of dipping them in the 0.4M EDT solution. Figure 4.4.a shows the resulting dark I-V curves of the devices. Films dipped in EDT for 3sec have a much better rectifying behaviour compared to the 15sec ones, and surprisingly their conductivity at +1V

bias, at which the Schottky barrier is expected to be eliminated, is higher than the one of the 15sec device despite the fact that in the second device less oleic acid molecules acting as insulators around the nanocrystals' surface are expected to be present. This behaviour can be associated with cracks on the films: a) less EDT is believed to cause less cracks[121] b) cracks act as short circuiting spots and inhibit diode behaviour.

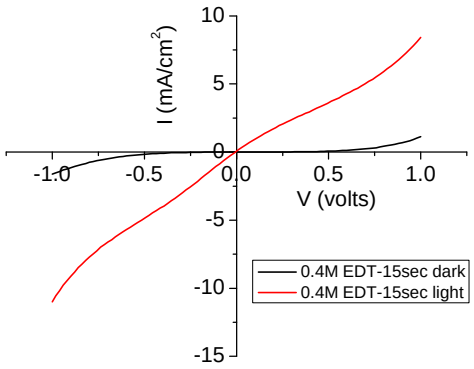


**Figure 4.3 Current-voltage measurements of a 200nmPbS device at dark and under 80mW/cm$^2$ AM.1.5 illumination. Device was fabricated using 0.4M EDT solution**

A quick way of comparing the diode behaviour of the devices is looking at their $I_{1V}/I_{-1V}$ ratios. That is because a Schottky type-cell follows the simple diode equation:

$$I = I_o(e^{\frac{Vq}{nkT}} - 1)$$

Where I the current under an applied bias V, $I_o$ the leakage current, q the elementary charge, k is Boltzmann's constant, T the temperature and n is the diode's ideality factor with minimum n=1 for ideal diodes. From this equation we derive that:

$$\left|\frac{I_{1V}}{I_{-1V}}\right| = e^{\frac{2q}{nkT}}$$

where we have used the fact that at 300K, $kT$ << 1 eV. Thus in the simplest model that the devices follow this equation in the voltage range -1V to 1V, the highest the absolute value of the $I_{1V}/I_{-1V}$ ratio is, the smallest the ideality factor of the diode. Thus Figure 4.4.b shows that the less EDT is used for fabricating the device's the better their diode-like behaviour is.

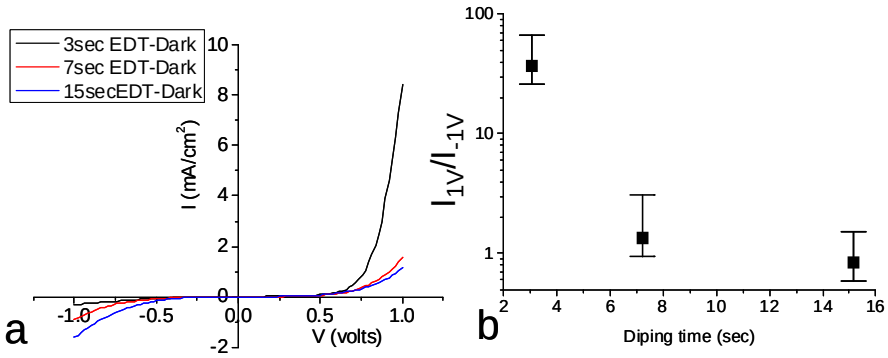


**Figure 4.4 a) I-V and b) $I_{1V}/I_{-1V}$ for 200nm thick devices made with varying dipping time in 0.4M EDT. Points represent average values and bars' limits the minimum and maximum measured values.**

**Comment [a.s29]:** I would prefer not to quantitavely use Shockley equation for poor devices

To further understand whether the improvement in diode behaviour is associated with the amount of oleic acid bonded on the nanocrystals after EDT treatment, we compared a device with a second one for which an additional treatment in a 0.01M pyridine in acetonitrile solution was used during film fabrication. Pyridine is an aromatic amine which readily dissolves oleic acid and lead oleate, is a non-solvent for PbS nanocrystals and compared to EDT should have a lower affinity to PbS nanocrystal surface, as has been reported for PbSe[123, 126]. In addition amines do not reduce oxide species from the surface of PbS nanocrystal films as EDT does[118, 122, 137]. Thus after the EDT step, which results in ~100% removal of oleic acid[123], pyridine's main effect on the films is expected to be removal of the small amount of remaining oleic acid. The EDT and EDT + pyridine treated films' photoresponse

curves are shown in Figure 4.5. The pyridine step caused a symmetric I-V response from the film. This result supports the idea that strong dependence of the films' diode behaviour to EDT treatment is mainly associated with the amount of oleic acid removed from the nanocrystals and not the changes on the nanocrystals' inorganic surface.

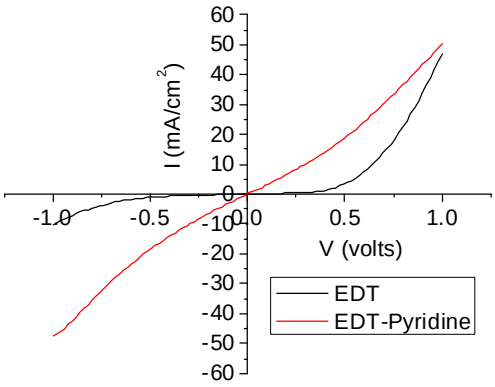


**Figure 4.5 I-V response in the dark showing the effect of additional treatment of devices with pyridine**

The amount of EDT replacing oleic acid controls the interparticle distance and the electronic coupling between the nanocrystals. We sought to investigate this by optical absorption spectroscopy. Figure 4.6.a shows the absorption spectrum of two nanocrystal sample solutions in hexane- one with a first exciton peak at 780nm and the other at 920nm. Figure 4.6.b shows the absorption of nanocrystal films fabricated by 3 dipping cycles of the EDT dip coating method with two different EDT concentrations using the 780nm nanocrystals. In agreement with previous reports, this figure shows that the nanocrystals' excitonic peak is red shifted and strongly broadened in films because of electronic coupling between the nanocrystals. Nevertheless, the absorption spectra of the two films are identical which indicates that

using 0.4M EDT does not alter the energy gap of the nanocrystals more than when using 0.03M EDT. Thus, the difference in the diode behaviour of films made with different EDT concentrations shown in Figure 4.7 is not related to any change of the electronic coupling of the nanocrystals in the films.

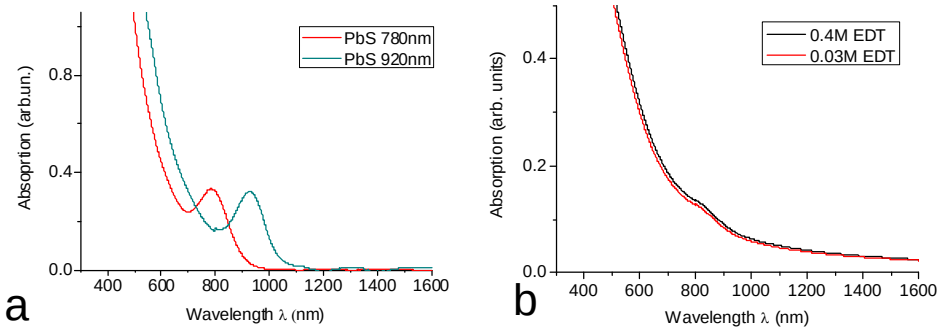


**Figure 4.6 a) Absorption spectra of two nanocrystal batches in hexane b) absorption spectra of PbS 920nm films prepared with different EDT solutions**

Figures 4.7.a and b show a dramatic improvement of the devices diode behaviour when using 0.01M EDT compared to 0.1M. It also shows improvement when changing the EDT dipping time from 7 to 3sec. Based on the above analysis we conclude that using more than 0.01M EDT for film fabrication yields devices with poor Schottky junctions. This is most likely associated to the amount of oleic acid removed from the nanocrystals. Since our data indicate that this phenomenon is not connected to change in the film's bandgap or the specific chemical changes known to be caused by EDT on the inorganic surface of PbS nanocrystals, we consider that is plausible this phenomenon be connected to the previously reported role of EDT (and amines) as an electron trap itself[121]. In this case, the functionality of the device will depend on the interplay between the positive role of EDT as a short ligand and a

reducing agent passivating $PbSO_4$ electron trap surface states, and its negative role as an electron trap itself. This model can explain our observations.

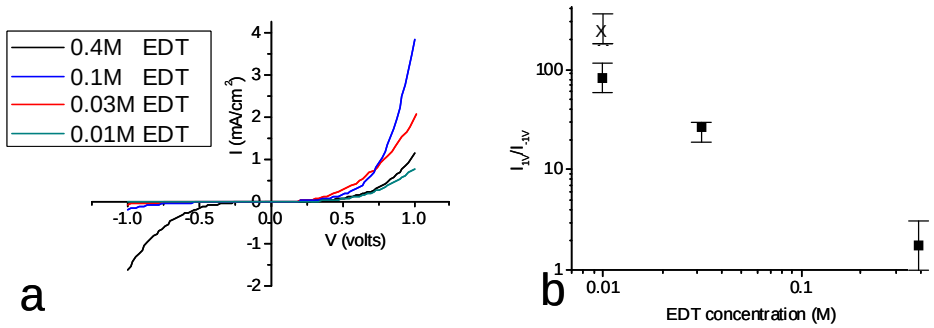


**Figure 4.7 a) I-V and b) $I_{1V}/I_{-1V}$ for 200nm thick devices made with dipping for 7sec (3sec for point marked with x) in different concentrations EDT/acetonitrile solutions. Points represent average values and bars' limits the minimum and maximum measured values**

**Comment [a.s30]:** I would prefer not to quantitavely use Shockley equation for poor devices

### 4.4.2 Optimizing Film thickness

We get the best photovoltaic response when dipping the films in 0.01M EDT. This agrees with the works reported by the Nozik and Sargent group on both dip-coating and spin-coating methods[75, 121]. Figure 4.8 shows the I-V curves of 3 devices fabricated with 0.01M EDT with three different nanocrystal film thicknesses: 140nm, 200nm, 300nm. The best power conversion efficiency (PCE), 0.31±0.01%, was obtained by the 200nm device, as compared to the 0.12±0.01%, 0.28±0.01% and for the 140nm and 300nm respectively. We explain the observed dependence of PCE, $I_{sc}$ and $V_{oc}$ considering the literature values of the Schottky depletion region width which is 150nm[72], the electron diffusion length which is 150nm[121]. These values determine that charge collection in the 200nm device benefits from both carriers photogenerated in Schottky region and carriers generated away from it drifting and diffusing to the

electrodes before recombining[120]. When decreasing the film thickness to 140nm the Isc drops slightly mainly because the film is fully depleted and does not offer photogenerated carriers outside the depletion region. Voc also drops because the device s fully depleted. On the other side in the 300nm device Isc drops significantly because the non-depleted film region too thick and holes travelling from the back (Al) to the front (ITO) contacts recombine in that region[75, 120]. Voc should remain unchanged compared to the 200nm, however it is increased probably because various morphological defects causing shorts in the films become less important for thicker films.

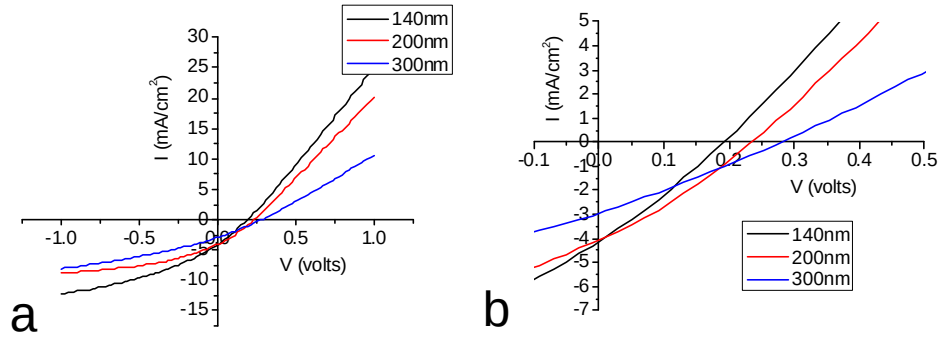


**Figure 4.8 a) I-V curves of varying thickness PbS solar cells under 80mW/cm$^2$ A.M. 1.5 illumination b) magnification of a close to the axis origin**

### 4.4.3 The effect of nanocrystal size

The experiments discussed so far were conducted using the 780nm nanocrystals. In our effort to improve the device characteristics we also used nanocrystals with an excitonic peak at 920nm as shown in Figure 4.6.a. As shown in Figure 4.9.a, the I-V curves the 920nm devices shows larger $I_{sc}$ and smaller $V_{oc}$ compared to the devices with the 780nm nanocrystals. The drop in $V_{oc}$ is attributed to the smaller bandgap of the 920nm nanocrystals which lowers the work function and

hence lowers the Schottky barrier. The same has been well presented before for PbSe nanocrystals Schottky junctions[75]. The device parameters for the two sets of devices can be found in Table 5.1 of Chapter 5.

The rise of $I_{sc}$ can be attributed to two effects. The first is the broader absorption spectrum of the 920nm nanocrystals which should result in a broader spectral photoresponse. This is verified by the measured external quantum efficiency (EQE) as a function of wavelength shown in Figure 4.9.b. This Figure also indicates that the excitonic photoconversion peak of the 920nm nanocrystals is sharper than the one of the 780nm nanocrystals. For the latter we discussed above that it is associated with similar broadening of the excitonic absorption peak because of the ligand exchange process and the small length of EDT. Previous experiments have shown that the nanocrystals the larger the broadening of the absorption spectrum[96]. By comparing Figures 4.6.a. and b. and Figure 4.9.b we can verify this.

**Comment [a.s31]:** Literature does not provide explanation

Broadening of the nanocrystals' absorption spectrum upon film deposition means that the nanocrystals forming the film lose their nearly identical electronic structure which is defined by their narrow size distribution and is manifested by their sharp first excitonic peak when in solution. The electronic properties of the film, especially the carrier mobilities, are critically influenced by this and the subsequent ability of electronic coupling between neighbouring nanoparticles. As discussed in **3.2** the electronic coupling is enhanced when the nanoparticles have the same energy levels. So, when the size uniformity is disturbed this has a negative impact on the electrical properties of the nanocrystal film and this is a second reason why the 920nm film gives a higher $I_{sc}$ e.g. this is why the ~920nm peak in Figure 4.9 is not just better defined but also higher.

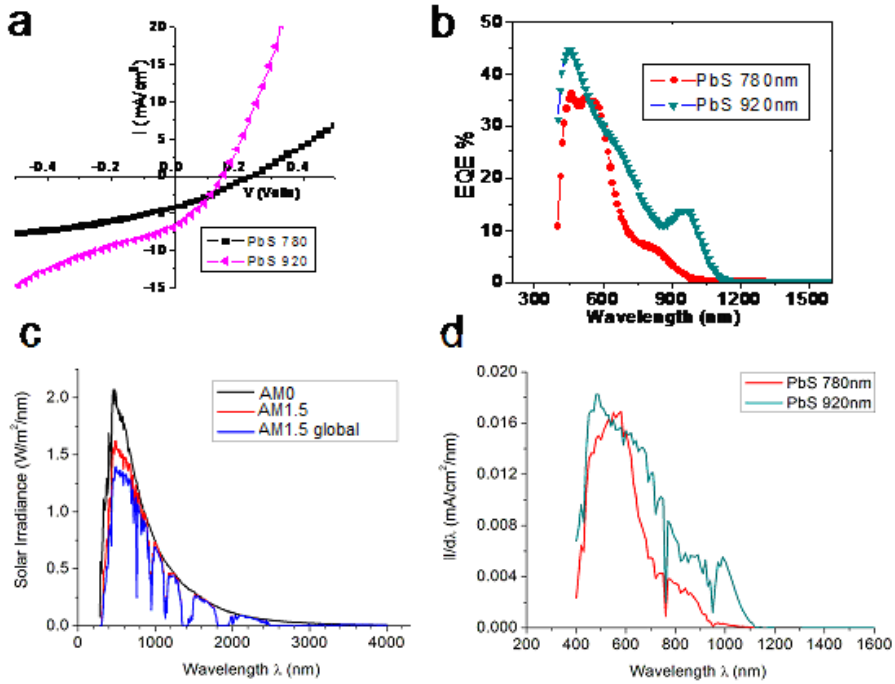


**Figure 4.9 a) 80mW/cm$^2$ AM.1.5 I-V curves of devices made with the 780 and 920nm PbS nanocrystals b) external quantum efficiency measurements for the two devices c) Various types of solar irradiance d) Photocurrent density spectral response of the devices**

The validity of the EQE measurements was verified by using them to calculate $I_{sc}$ and compare this value with the directly measured one. To calculated this we used the 100mW/cm$^2$ AM.1.5 global flux solar spectrum ($I_{opt}/d\lambda$) shown in Fig 4.9.c provided by NREL laboratories website[139]. Then, from the EQE measurements shown in Fig 4.9.b, we calculated the photocurrent density flux $I_{sc}/d\lambda$, as follows

$$I_{sc}/d\lambda = 0.8*EQE*I_{opt}/d\lambda$$

where the 0.8 factor accounts for the fact that our solar simulation I-V measurements were under 80mW/cm$^2$ AM1.5 illumination. Results are shown in Fig 4.9.d. We then calculated $I_{sc}$ by integrating:

$$I_{sc} = \int_{400}^{1800} I_{sc} \frac{1}{d\lambda} * d\lambda \,.$$

For the devices studied the directly measured $I_{sc}$ under 80mW/cm$^2$ AM1.5. The calculated values of $I_{sc}$ were 4.35 and 6.49 mA/cm$^2$ for the 780 and 930 nm devices respectively, compared with the directly measured values of 4.37 and 6.59 mA/cm$^2$. The two sets of values were in good agreement.

The characteristics of the optimised PbS devices, presented in Table 5.1 of Chapter 5, have both similarities and differences with similar PbS nanocrystal/ Al Schottky junctions reported in the literature. The short circuit currents are comparable with the 10-14 mA/cm$^2$ produced by the Nozik, Sargent and Alivisatos groups for devices utilising nanocrystals with excitonic peaks at >1400nm[75, 121, 135]. We used smaller nanocrystals but considering the observable dependence of $I_{sc}$ with nanocrystal size we expect that >10mA/cm$^2$ photocurrents can be obtained when using larger nanocrystals. However, our open circuit voltages of 0.33 V are smaller than the 0.4-0.44 V reported by the other groups. We consider two possible reasons for this important difference. The first is associated with poor environmental conditions often observed in the glovebox used for the experiments during the duration of this study. Although precautions where taken to keep good water and oxygen free conditions while processing materials and devices, environmental conditions were often poor during time in between experiments when materials were stored in the glovebox. This certainly caused oxidation of the nanocrystals used and negatively affected the quality of the Schottky junctions in our devices.

**Comment [a.s32]:** Removed comment on shortcircuiting

### 4.4.4 Aging of solar cells

As mentioned in the experimental methods the devices were loaded in an air-tight holder before being removed from the glovebox and tested. This procedure

aimed at preventing oxidation of the nanocrystals and devices because oxide species on the surface of PbS nanocrystals act as deep electron traps[118]. The oxidation process however also depends on the ligands passivating the nanocrystals. Amine capped PbS nanocrystal devices have a 0.3-5 hour lifetime at ambient conditions[74, 86]. However, contrasting results have been reported when using thiols: the Sargent group has reported that when treating butylamine capped PbS and PbSe nanocrystals with small thiols their lifetime increase -from an hour to > 2months and this is associated with the specific oxide species induced by this process[36, 140]. On the other hand, the Nozik group has reported that PbS Schottky devices made like ours have very small lifetimes on ambient conditions, <5minutes[75]. Our devices behave similarly to the ones of Nozik and this is shown Figure 4.10. It is evident that the devices produced by the EDT dip coating method are very sensitive to oxidation. This is a problem that has to be addressed in the future development of this fabrication method and the solution is likely to include an amine based ligand exchange step and oxygen treatment of the films prior to the Al deposition.

**Comment [a.s33]:** Negative comment removed

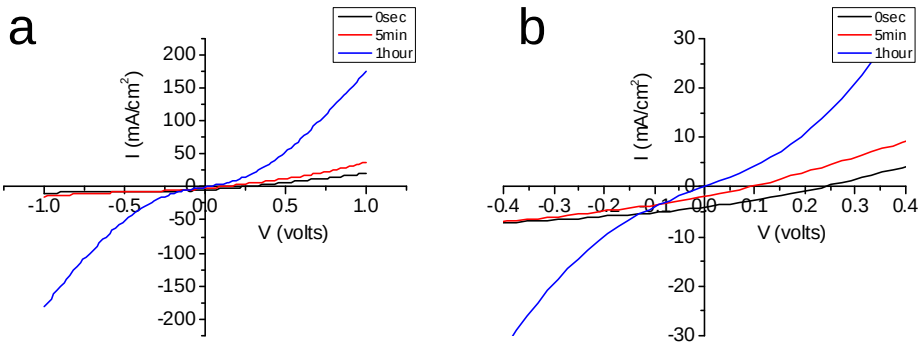


**Figure 4.10 a) Time evolution of I-V from an illuminated Schottky junction device at ambient conditions b) magnified part of a. at the axis origin**

## *4.5 Conclusions*

We have successfully reproduced a dip-coating method for the fabrication of all inorganic nanocrystal solar cells. The performance of the PbS nanocrystal/ Al Schottky junctions depends critically on the amount of EDT replacing oleic acid on the surface on the nanocrystals during device fabrication. Complementary to the relevant literature we have shown that overtreatment of the nanocrystal films with EDT yields poor Schottky junctions.

The optimum film thickness for the solar cells is 200nm. The dependence of the device characteristics on the PbS film thickness agrees with the literature. The obtained photocurrents follow closely the relevant state of the art literature and originate from high the external quantum efficiency of the devices. The spectral photoresponse extends into the near-infrared spectrum and can be tuned by the nanocrystal size. The open circuit voltages of our devices are smaller than literature values, propably because of oxidation or other contamination in the glove box we used. However small values $V_{oc}$ are an intrinsic problem of this type of cells. This problem is addressed in Chapter 5. Finally the solar cells are highly unstable under ambient conditions.

**Comment [a.s34]:** corrected

# 5 PbS/SnS nanocrystal heterojunction photovoltaics

## *5.1 Synopsis*

Chapter 5 examines a method for increasing the efficiency of Schottky-junction PbS nanocrystals solar cells. It employs the use of SnS nanocrystals between the lead nanocrystals and the transparent conductive electrode as schematically shown in Figure 5.1. The chapter starts with the motivation behind this work, followed by the presentation of the SnS nanocrystal synthesis and characterisation. Then, using different top electrodes and film thicknesses, we focus on the study of SnS:PbS bilayer solar cells. The results indicate that the two materials form a type-II heterojunction. The chapter continues with optimisation of the bilayer devices and systematic comparison between single and bilayer devices showing that bilayer devices are more efficient.

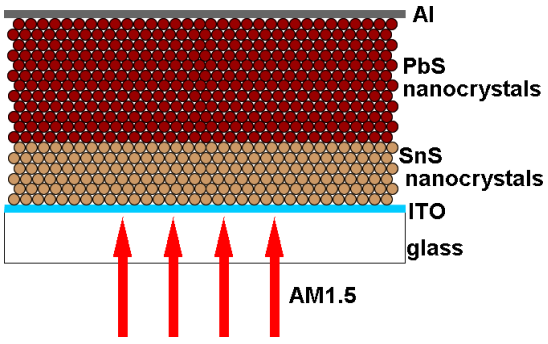


**Figure 5.1 Schematic representation of a SnS-PbS nanocrystal bilayer device**

## *5.2 Motivation*

Lead chalcogenide nanocrystal Schottky junction solar cells[73, 75, 120] have achieved impressive short circuit currents >20mA $cm^{-2}$ [75]. However the overall power conversion efficiency is limited by small open circuit voltages generated at the metal-nanocrystal Schottky barrier as demonstrated in Chapter 4. This chapter examines a solution to this problem by employing a Tin Sulphide (SnS) – Lead Sulphide (PbS) nanocrystal heterojunction within the active layer of the cell.

The Schottky barrier formed between low work function metals such as calcium or aluminium, and p-type lead chalcogenide nanocrystal films has been extensively studied[72, 75]. The barrier height for aluminium is between 0.1 and 0.3eV and depends on the nanocrystal material, size, surface chemistry and device processing conditions[74, 75]. Mild oxidation of PbS in the presence of thiols has been shown to improve the $V_{oc}$ of such devices to 0.43V[121, 141], though it should be noted that thiol-passivated PbSe devices show contrasting results[36, 75]. These $V_{oc}$ values limit the power conversion efficiencies of PbS and PbSe Schottky-type cells to around 1.8% despite having up to ~70% external quantum efficiencies at 500-550nm optical wavelengths (37% for 975nm IR)[36, 73]. One other limiting factor is that the Schottky barrier is formed at the back contact and creates a depletion width of only around 150 nm[73]. This limits the optimum active layer thickness to 230 nm which is not sufficient for complete absorption of incident solar light[73]. Both problems could be solved by using a second nanomaterial to form a type-II heterojunction with PbS NCs. In the past organic materials like MEH-PPV[55] and $C_{60}$[71, 86] have been shown to work to some extent with PbS. An alternate approach would be to use a second nanocrystalline semiconductor to form a nanocrystal bilayer[57].

**Comment [a.s35]:** yes double checked that

We have chosen SnS to form a good junction with PbS. SnS nanocrystals have two structural phases, namely zinc blende and orthorhombic[142]. The bulk orthorhombic SnS has a weak indirect band gap at ~1.1 eV[143] and a strong direct band gap at ~1.43 eV[144]. The equivalent band gaps for zinc blende SnS are ~1.24eV and 1.77eV respectively[142]. Therefore SnS is potentially photovoltaic in a wide wavelength range and is transparent the infrared spectrum where PbS is efficient. Thus studying and improving the optoelectronic properties of SnS nanocrystals in a photovoltaic SnS-PbS heterojunction could potentially improve the cells' photoresponse across a wide wavelength range. Furthermore, SnS has some unique characteristics: i) it is non toxic ii) both its constituents Sn and S are abundant and cheap iii) it has a large absorption coefficient $10^4 cm^{-1}$ near the fundamental absorption edge[145]. Thus any advantages made in the course of this study on SnS nanocrystals can be used in future studies of non-toxic cheap solar cells. In addition, SnS is regarded as an enviromentaly and chemically stable material, resistive to oxidation[146].

Comment [a.s36]:

Bulk CdS/SnS/PbS multilayer solar cells with $V_{oc}$ = 0.32 V and $I_{sc}$ = 1.6 $mA/cm^2$ [147] have been demonstrated before but little is known about the alignment of the energy bands in a SnS/PbS heterojunction. There have been studies of the electronic structure of $SnS_2$[148] but the electronic structure of SnS is not well understood; in particular quantum confinement effects, structural phase effects, absolute energy values of the ionization potential and the electron affinity referenced to zero vacuum energy. For the above reasons synthesis, characterisation and utilisation of SnS nanocrystals in photovoltaics is both interesting and useful.

Furthermore, the dip coating method for film fabrication which was explored for PbS nanocrystals in Chapter 3 should be also applicable for colloidal SnS nanocrystals as a IV-VI semiconductor. Fabricating SnS-PbS nanocrystal bilayer

junctions via the dip coating method opens possibilities for fabricating more complex device architectures, such as alternating layers (e.g. SnS-PbS-SnS-PbS-…) and other multilayer structures necessary for tandem cell technology.

## *5.3 Experimental Methods*

### 5.3.1 Synthesis of SnS nanocrystals

In a 25ml vial furnished with a thermocouple and a magnetic stirrer, 0.444g of $SnCl_2$ dihydrate, 6ml of oleic acid and 5ml of octadecane were mixed for 40 minutes under vigorous stirring, heating at 150$^{o}$C and nitrogen flow. This allowed dehydration of the salt complex as was indicated by water bubbles coming off the solution. By the end of this step bubbling had stopped and the anhydrous salt was a fine powder attached to the sides of the vial. Then 2ml of oleylamine was injected in the solution completely dissolving the salt within 30 minutes. The temperature was set to the desired value, between 80$^{o}$C and 170$^{o}$C, and keeping $O_2$ free conditions 200μl of TMS were injected in to the solution causing rapid nucleation of SnS nanocrystals, as manifested by a change of the solution's colour from transparent to dark brown. Then, the reaction was instantly (<5sec) quenched by dipping the vial in an ice bath causing the temperature of the vial to drop below 40$^{o}$C in less than 20 seconds.

### 5.3.2 Post synthesis processing of SnS nanocrystals

The product solution was transferred to a 50ml plastic centrifuge tube. SnS nanocrystals were precipitated from the reaction solution by adding 40ml of a

premade 3:1 volume ratio mixture of ethyl acetate and methanol followed by a 10 minute centrifuge at 4000rpm. The supernatant solution was then removed and the brown precipitate was either re-dissolved in hexane for device fabrication or further cleaned using a 2:1 volume ratio mixture of Ethyl acetate and Acetonitrile (denoted as EAA). In this second cleaning step the EAA solution was added to the centrifuge vial dissolving residues of oleic acid and oleylamine still present to the wall of the vial and in the precipitate, without dissolving the SnS nanocrystals. To enhance this effect, after adding the EAA solution, the vial was gently shaken before removing all of the solution. This procedure was repeated 2 times before final drying and redispersion of the nanocrystals in hexane. All material processing took place in an oxygen free (<10ppm $O_2$) dry (<4ppm $H_2O$) glovebox.

### 5.3.3 Synthesis and processing of PbS NCs

PbS nanocrystals with excitonic peaks at 780nm and 920nm were prepared and processed as dedcribed in **3.4.1** and **4.3.1**.

### 5.3.4 TEM, Optical Spectroscopy, XRD

TEM samples were prepared by dipping lacy carbon films in light hexane/ nanocrystal solutions, then leaving them to dry for 1 minute. Low magnification TEM and HRTEM was performed using a 4000HR JEOL microscope equipped with a Gatan camera.

Optical absorption measurements of nanocrystal/hexane solutions were conducted using a Varian Cary 5000 UV-visible-NIR spectrometer using quartz cuvettes.

XRD was conducted by Mr. Christopher Cattley on a Philips th2th diffractometer using monocrystalline Si substrates on which SnS NC synthesized at 170°C were drop cast from a 0.1mg/ml hexane solution.

### 5.3.5 Device fabrication and testing

Solar cell Devices were prepared as described in **2.4.7** and **4.3.2 using two** 0.007g/ml solutions, one of SnS nanocrystals in hexane and one of PbS nanocrystals in hexane. The IV and spectral responce of the devices were tested as described in **2.4.8** and **4.3.3**.

## *5.4 Results and Discussion*

### 5.4.1 Characterisation of SnS nanocrystals

X-ray diffraction (Figure 5.2.a) of drop cast SnS nanocrystals on silicon and comparison with reference structures[142] shows co-existence of orthorhombic (a= 3.99 Å, b= 4.34 Å and c= 11.2 Å) and zinc blende (a=b=c=5.845 Å) phases, with the latter dominating. Such coexistence has been reported before for oleylamine assisted synthesis of SnS nanocrystal at growth temperatures below 200$^{o}$C[142]. Unmatched peaks in Figure 5.2.a are attributed to un-reacted precursors and possible side products, as previously reported[142]. The minor presence of orthorhombic phase

nanocrystals is also verified by HREM imaging of individual nanocrystals as in Figure 5.2.b,c.

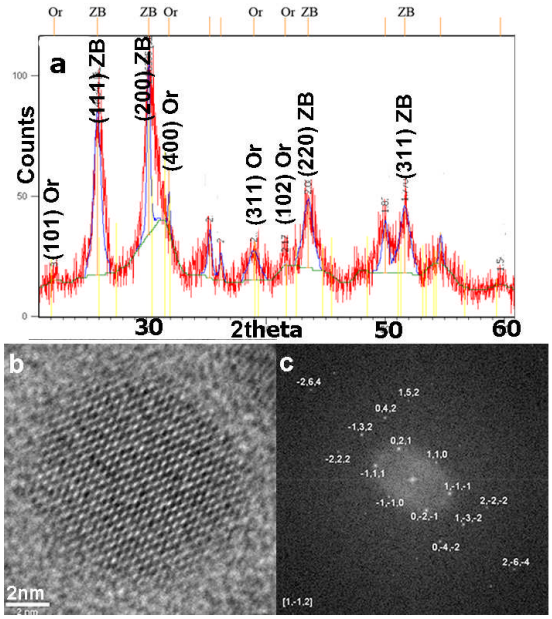


**Figure 5.2 a) XRD pattern of SnS nanocrystals grown at 170°C with positions of orthorhombic (Or) and zinc blende (ZB) reflections indexed b) HREM micrograph of an orthorhombic SnS NC and c) its FFT pattern indexed**

Transmission electron microscopy of as-prepared SnS nanocrystals (Figure 5.3.a,c) shows them to be well dispersed, which suggests they are well passivated by oleylamine/oleic acid molecules. The nanocrystal size depends on the reaction temperature, 9.6nm ±1.5nm for 170°C and 6.8nm ±1.5nm for 120°C as shown in Figure 5.4 while the shapes are irregular but most nanocrystals appear quasispherical.

Optical absorption of a nanocrystal suspension (Figure 5.5.a) shows an absorption onset at 1.47eV (845 nm) and the flat baseline beyond 845 nm suggests an absence of any bulk or aggregated material which would cause light scattering. The blue shift of the absorption onset compared to the 1.1-1.24eV absorption onset of bulk SnS suggests that bandgap of the SnS nanocrystals is increased due to the quantum confinement effect similarly to what is reported elsewhere for SnS nanocrystals[146, 149].

When we tried further cleaning of the nanocrystals by applying a second precipitation step (with alcohol) the nanoparticles aggregated and became insoluble to hexane which indicates that the surface ligands were stripped-off when precipitated more than once. Similarly alcohol-induced stripping of oleic acid from the surface of PbS nanocrystals has been reported before[7] and can be explained by the mechanism presented in **3.3**.

Thin nanocrystals films were fabricated using the ethylenedithiol (EDT) dip-coating method reported before for PbS and PbSe nanoparticles[4]. To test whether the EDT dip coating method is applicable for SnS nanoparticles, TEM samples of as prepared SnS nanocrystals were dipped in a 0.01M EDT in acetonitrile solution for 5 sec. TEM imaging shows that, as compared to Figure 5.3. a and b, the interparticle distance is greatly reduced after EDT treatment as shown in Figure 5.3.c and d. This demonstrates the effectiveness of the ligand exchange method on SnS.

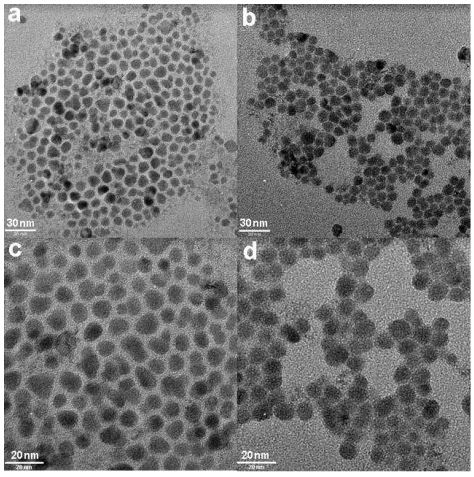


**Figure 5.3 TEM micrographs of SnS nanocrystals passivated with oleylamine (a,c) and passivated with EDT following a ligand-exchange process on the TEM grid (b,d).**

The current-voltage (I-V) characteristics of a 400nm SnS film sandwiched between ITO and Al in the dark and under 80mW/cm$^2$ AM.1.5 solar illumination are shown in Figure 5.5.b. These measurements show that the SnS nanocrystal films act as photoconductors with a 130 times increase in current under 1V bias. There is negligible open circuit voltage ($V_{oc}$) and short circuit photocurrent ($I_{sc}$) indicating the absence of any significant Schottky barrier formed at the NC/electrodes interfaces.

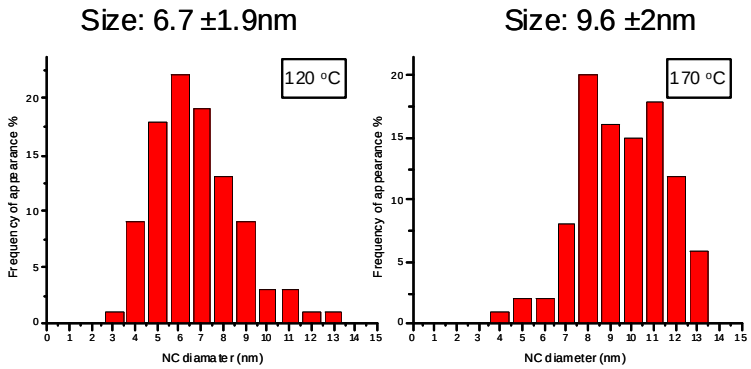


**Figure 5.4 Size distribution histograms showing control of SnS nanocrystals' size with growth temperature**

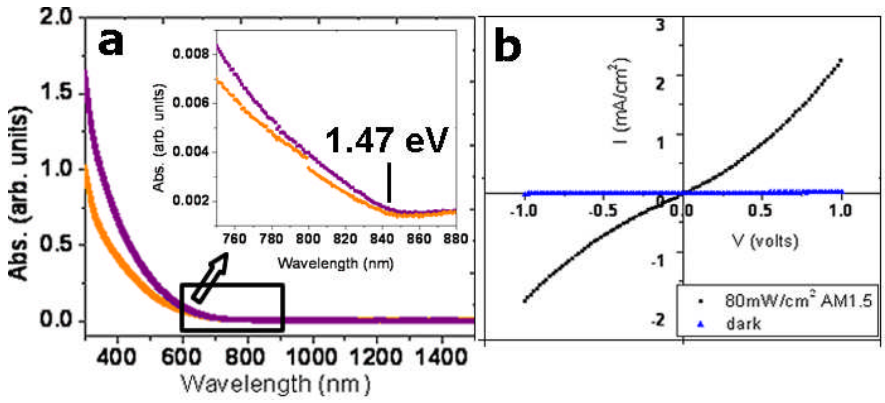


**Figure 5.5 a) Absorption of SnS nanocrystals grown at 120°C suspended in hexane in two different concentrations. The inset zooms in to the absorption onset b) I-V characteristics of an ITO/400nm SnS NC/ device in the dark and under A.M. 1.5 illumination.**

### 5.4.2 Study of SnS-PbS heterojunction

The first bilayer devices examined were made of 140nm SnS/ 140nm PbS thin films with the following two architectures: ITO/SnS/PbS/Al and ITO/PbS/SnS/Al using PbS with a 780 nm first excitonic peak and SnS NC synthesized at 120$^{o}$C. Both bilayer devices exhibited largely increased $V_{oc}$ and fill factor values (FF) compared to a control ITO/140nmPbS/Al devices as shown in Figure 5.6.a. The power conversion efficiencies (PCE) of the two bilayer types were 0.26% and 0.07% larger than the 0.02% of the control devices, despite the bilayer's smaller $I_{sc}$. We note, that our control device has a significant lower $V_{oc}$ compared to the same devices present in Chapter 4 which presented $V_{oc}$= 0.19V and 0.12% PCE. We attribute this difference to the 10-15ppm $O_2$ level in the glovebox during the dates we conducted the current experiments. Despite this, the bilayer device we discuss here is more efficient than the "un-oxidised" 140nm devices presented in Chapter 4. That triggers us to seek further investigation in the future on whether the SnS:PbS devices are more stable compared to control PbS devices.

**Comment [a.s37]:** added after JS note

Notably, the two bilayer types had different polarities at short circuit conditions: in the SnS/PbS type, Al acted as the cathode while in the PbS/SnS, the Al was the anode. For the control PbS devices Al was the cathode, i.e. under open circuit conditions photogenerated electrons flow to Al, as reported before[72, 75]. We sought to further investigate the same polarity of the bilayers using gold as the back contact. Au has a lower work function than ITO and the electric field generated between ITO and Au is in the opposite direction to ITO/Al one[75]. In addition the PbS/Au contact is ohmic[72]. Indeed the ITO/PbS/Au device where ITO was the cathode exhibited a small $I_{sc}$ =0.49 mA/cm$^2$ and negligible $V_{oc}$, FF and PCE. However bilayer devices acted as solar cells with $V_{oc}$ and $I_{sc}$ as shown in Figure 5.6.b and again polarities as in the case

of Al. This data and the relative differences of $I_{sc}$ and $V_{oc}$ of the bilayers depending on the electrodes strongly indicates a type-II heterojunction between SnS and PbS as schematically proposed in Figure 5.6.c in which, for clarity of presentation, the Schottky barrier formed between PbS and Al has been omitted. We note that we don't have any direct data from experiments or from the literature on the valence and conduction band energies of SnS and thus we can not state specific values for the energy levels showed in Figure 5.6.c We only have indirect information on the band possible alignment between SnS and PbS and this is discussed further down in **5.4.4.**

Comment [a.s38]:

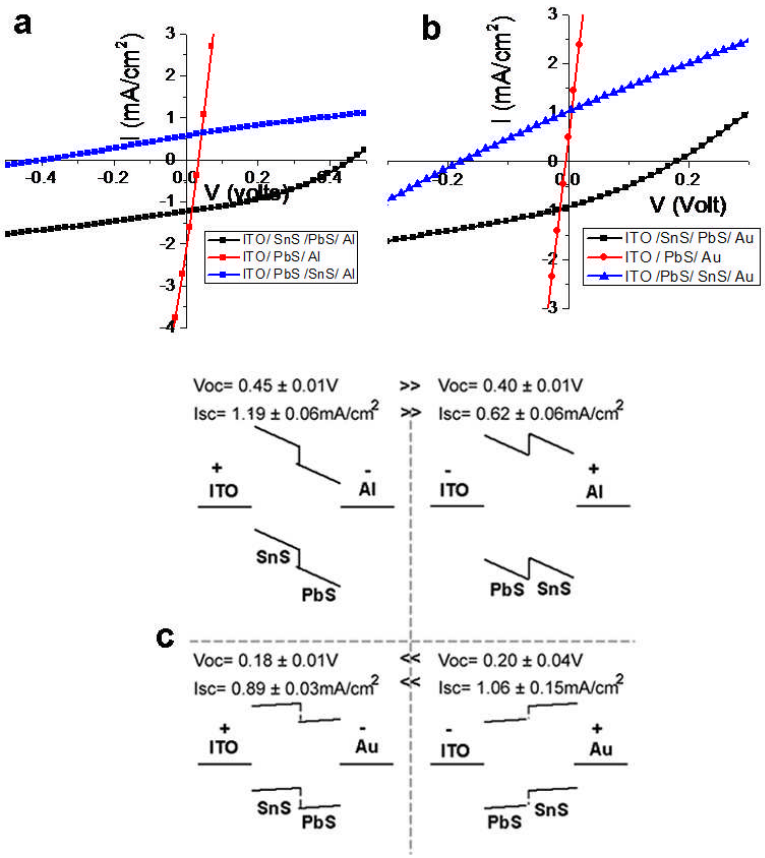


**Figure 5.6 a.b) I-V measurements of 140nm SnS/140nm PbS bilayer and control PbS devices with Al and Au as back contacts c) schematic representation of the proposed type-II heterojunction in the devices at open circuit conditions**

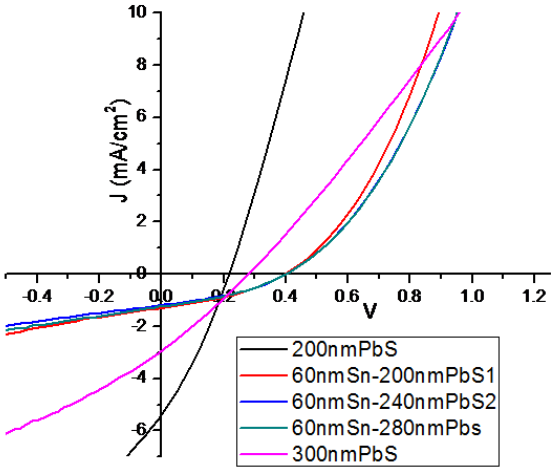


**Figure 5.7 I-V measurements of PbS and SnS-PbS devices with various PbS thicknesses under 80mW/cm$^2$ A.M.1.5 illumination**

The bilayer devices yield smaller photocurrents than the photocurrents from PbS only devices. To investigate the origin of this drawback we fabricated devices of various SnS and PbS thickness. When the PbS thickness was varied between 200 and 300nm the $I_{sc}$ and $V_{oc}$ of the device remained the same (Figure 5.7). This was different to what was observed for PbS control devices where the photocurrents had dropped for the same thickness variation. We mentioned in Chapter 3, that this drop of $I_{sc}$ for PbS devices is due to increased recombination of holes travelling from the PbS/Al interface to the ITO. The fact that this does not happen for the bilayer devices indicates that the hole transport is impeded by the SnS layer, irrespective of the PbS thickness. This is a major factor in the bilayers' small photocurrents. This is strange considering that bulk SnS is a p-type semiconductor with high hole mobility (~500 cm$^2$/Vs)[150] and we would expect the SnS nanoparticle films to be p-type semiconductor as well. In nanoparticle films, the decreased conductivity may be also

caused by traps and barrier heights from the surfactant molecules on the surface of the nanoparticles.

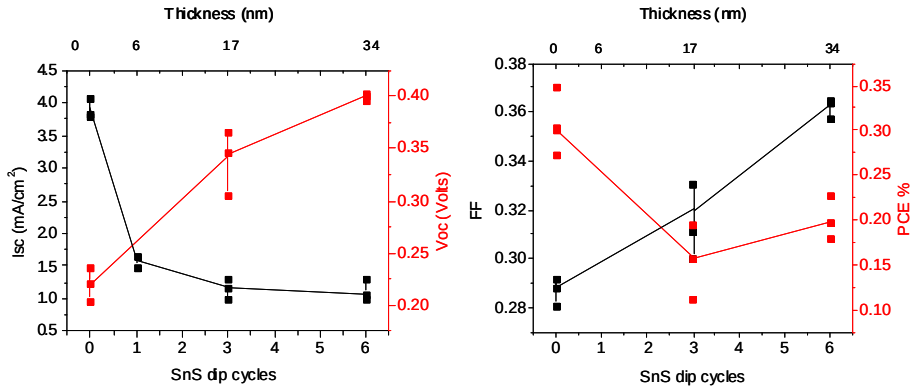


**Figure 5.8 Dependence of bilayers' characteristics on SnS layer thickness (PbS layer is 200nm)**

Experiments with varying SnS thickness (Figure 5.8) showed that even a ~6nm thick SnS layer is sufficient to decrease the bilayers $I_{sc}$ by 60% compared to the control PbS device. At the same time increasing the SnS thickness increases the $V_{oc}$ and fill factor (FF). Regarding the evolution of the power conversion efficiency with increasing SnS thickness, there seems to be an interplay between the increase in $V_{oc}$ and FF and the drop in $I_{sc}$- due to this interplay and for the 200nm thick PbS layer, the power conversion efficiency drops when we add up to three monolayers of SnS nanoparticles, then it slowly increases as we increase SnS thickness. However we should note that bilayer devices with 140nm thick PbS layers have larger power conversion efficiencies compared to 140nm thick pure PbS devices, because of the very poor $V_{oc}$ and FF of the latter.

### 5.4.3 Optimization of heterojunctions

To further study bilayers and compare with control devices we focused on ITO/60nmSnS/200nm PbS/Al since 200nm PbS film thickness is nearly optimum for ITO/PbS/Al solar cells. Two sets of devices were initially fabricated using PbS nanocrystals with an excitonic peak at 780nm and two batches of SnS nanocrystals synthesized at 80$^{o}$C and 120$^{o}$C. The device characteristics of the bilayer and control devices are shown in Figures 5.9.a, 5.10.a and Table 1. Average values and standard deviations in Table 1 refer to 3 devices for each bilayer type and 6 for each control type. The $V_{oc}$ of the bilayer devices appears to depend on the temperature of the SnS synthesis, which we showed controls the nanocrystal size, with the smaller SnS nanocrystals giving higher $V_{oc}$. Both bilayer sets exhibited more than double the $V_{oc}$ but less than half the $I_{sc}$ of the control devices and the overall power conversion efficiencies of the bilayers was also smaller.

**Table 5.1**

**Device characteristics for control and bilayer devices with 200nmPbS and 60nmSnS thick films**

| | Voc (Volt) | Jsc (mA/cm^2) | FF | PCE % |
|---|---|---|---|---|
| PbS 780nm | 0.22 ± 0.01 | 4.1 ± 0.2 | 29 ± 1 | 0.31 ± 0.01 |
| 120C SnS:PbS 780nm | 0.4 ± 0.0 | 1.12 ± 0.15 | 36 ± 1 | 0.2 ± 0.01 |
| 80C SnS:PbS 780nm | 0.44 ± 0.01 | 0.87 ± 0.17 | 24 ± 1 | 0.16 ± 0.02 |
| 80C EAA SnS:PbS 780nm | 0.45 ± 0.0 | 1.84 ± 0.13 | 30 ± 1 | 0.31 ± 0.01 |
| PbS 920nm | 0.12 ± 0.03 | 7.22 ± 0.85 | 32 ± 2 | 0.37 ± 0.11 |
| 80C EAA SnS:PbS 920nm | 0.35 ± 0.02 | 4.15 ± 0.45 | 27 ± 2 | 0.5 ± 0.01 |

Looking for ways to improve the $I_{sc}$ of the bilayer devices we considered that conductivity of the SnS film may have been limited by organic impurities since post-synthesis cleaning of SnS nanocrystals was limited to one precipitation step because of the alcohol induced ligand stripping effect. We sought to further clean the nanoparticles by washing them with mixture of ethyl acetate and acetonitrile (EAA). Ethyl acetate further removed much of the extra oleic acid/oleylamine while acetonitrile kept the nanoparticles precipitated preventing them from aggregating. The effectiveness of this cleaning step was visible to the naked eye, making the nanoparticle powder appear dryer, but still dispersible in hexane. The impact on the bilayer performance was great; EAA treatment doubled $I_{sc}$ while $V_{oc}$ remained the same as shown in Figure 3a and Table1. These results fit to the type-II model proposed; $V_{oc}$ is determined by charge interaction between SnS and PbS and the PbS/Al Schottky barrier and is independent of organic impurities in the SnS film. We hypothesise that the $I_{sc}$ is improved by increasing SnS charge mobility when organic impurities are minimised although as yet we have no direct evidence for this. Plotting the devices characteristics under dark as logI-V as shown in Figure 5.9.b we can measure[72] and compare the ideality factors of the devices which are 1.32 for the control and 2.4 and 2.07 for the bilayer and EAA bilayer respectively. In the same graph we observe that while in the control device the logI-V curve deviates quickly from the linear fitting predicted by a simple diode equation[72], the latter holds for a larger forward bias in the case of the bilayers. One feasible explanation is that in the bilayer, electrons leaking through the PbS/Al Schottky barrier at forward bias conditions are blocked at the SnS/PbS interface. For clarity of presentation in Figure 5.9.c we draw the band diagram of the bilayer device as we estimated to be: with a Schottky barrier at the PbS/Al interface and a type-II heterojunction at the SnS/PbS

interface. We emphasize that we don't have data on the SnS HOMO-LUMO values but our devices' behaviour suggest that the SnS is the electron donor (and hole acceptor) of the heterojunction. In Figure 5.9.c the ITO and Al energy levels and the PbS/Al barrier are taken from the literature[72].

**Comment [a.s39]:** added after JS comment

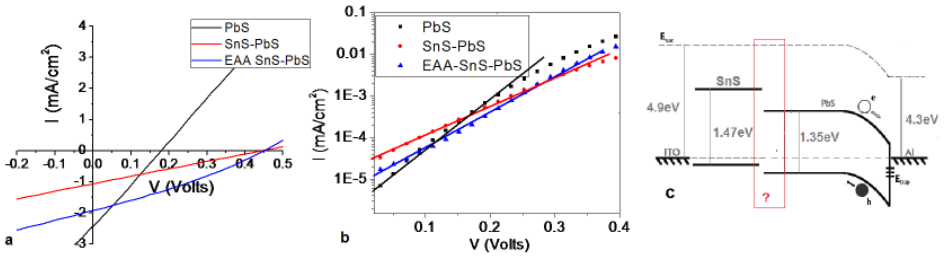


**Figure 5.9 a) I-V for 60nmSnS/200nm thick bilayer and control devices b) logI-V dark characteristics for the same devices c) Schematic representation of our estimate on the band-alignment in the ITO/SnS/PbS/Al devices.**

To further improve device performance we used PbS with a 920nm excitonic peak. Bilayer and control devices exhibited higher $I_{sc}$ compared to PbS 780nm devices and spectral measurements in Figure 5.10.b showed that this is due to the broadening of the spectral response. We note that these EQE measurements were validated by using them to calculate $I_{sc}$ under 80mW/cm$^2$ AM1.5, the calculated values had less than 5% deviation from the real $I_{sc}$ measured. We also note that the shape of the bilayers' spectral response looks similar to the control devices indicating that the photocurrent is mainly produced at the PbS layer. EQE measurements also indicate that the bilayers' $I_{sc}$ is limited by the SnS conductivity because the EQE at wavelengths beyond 840nm where SnS does not attenuate light, is 40% less than that of the control. Despite this, the bilayers had higher PCE under AM1.5 because of their improved $V_{oc}$. We believe that there is further scope for improving $I_{sc}$ of the bilayers by improving synthesis and post synthesis processing of the SnS nanocrystals.

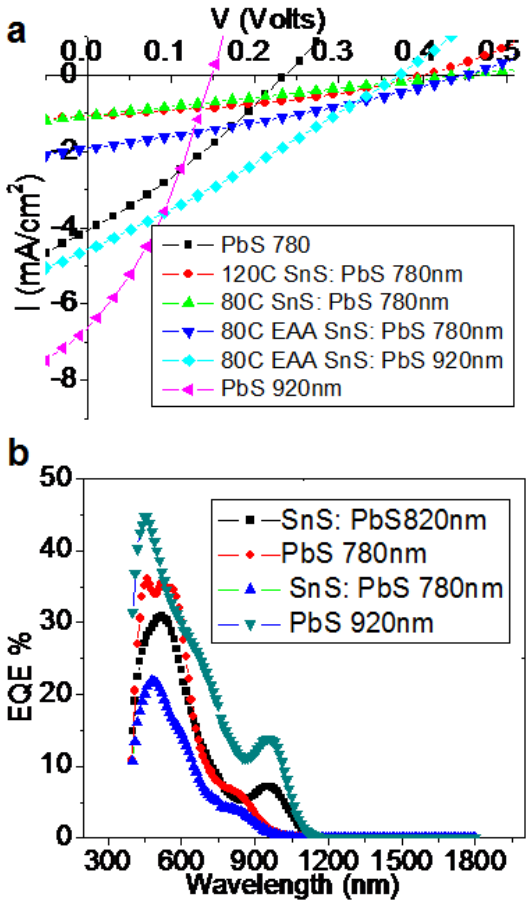


**Figure 5.10 a) I-V for 60nmSnS/200nmPbS thick bilayer and control devices using various PbS and SnS nanocrystal batches b) external quantum efficiency spectral measurements for selected devices.**

### 5.4.4 Discussion of the SnS-PbS heterojunction

So far we presented the following evidence supporting the idea that SnS and PbS nanocrystals form a type-II heterojunction:

1. The polarity of the bilayer devices depends on the bilayer order and not the electric field build up from the device electrodes;

2. The Isc of the bilayers doubles when SnS nanocrystals are further cleaned without a reduction in the $V_{oc}$. This can be explained by considering that the cleaning improves the hole transport in the SnS layer.

A question arising is whether this type-II model can be supported by previous published work on the energy levels of PbS and SnS. The electron affinity of bulk PbS is 4.7eV[151, 152], the bandgap is 0.4eV[153] and thus ionization potential is 5.1eV as schematically shown in Figure 5.10. Unfortunately little is known about the energy levels of SnS: the bandgaps for bulk SnS are 1.1 eV for orthorhombic and 1.2 eV for zinc blende SnS[142]. The valence band structure of orthorhombic SnS referenced to Fermi levels of photodetectors has been studied by many[154-156] but without any mention of the valence band energy levels referenced to the vacuum. Thus, this data can not be used to compare the levels of SnS with PbS unless the valence bands of the two materials have been studied on the same instrument.

In 1977 Shalvoy et al[155] did this experiment and reported that the first two valence photoelectron peaks below the detector's Fermi level for the two materials are 1.5 eV and 2.5 eV for orthorhombic SnS and 1.4 eV and 2.7 eV for PbS. The relative differences of the two peaks between the two materials are -0.1 eV and 0.2 eV. If we accept that this data indicates the valence band offsets between SnS and PbS we can draw the valence and conduction band of orthorhombic SnS as shown in Figure 5.10.

For the case of zinc blende SnS there is no experimental work comparing its electronic structure to PbS or orthorombic SnS. However Ichimura has recently reported density of states calculations on SnS that suggest the valence band energy level of bulk rock salt SnS is 0.73 eV lower than the valence band level of zinc blende SnS[157]. The orthorombic SnS should be closer to the rock salt case as the orthorhombic structure can be considered a distortion of the rock salt structure[157].

Ichimura suggested that the orthorhombic SnS valence level can be considered to be in between those of zinc blend and rock salt. So the level of zinc blende phase may be higher than the level of the orthorombic phase by up to 0.73eV. Based on this report we draw in Figure 5.11 the valence and conduction levels of zinc blend SnS as 0.7eV wide uncertainty bands to compare with PbS and orthorhombic SnS.

We continue this discussion considering quantum confinement effects in nanocrystals and how these may affect the HOMO-LUMO levels and the heterojunction band alignment. The 780 nm excitonic peak of the PbS nanocrystals corresponds to a 1.6 eV energy gap. This is 1.2 eV larger than the 0.4 eV bulk bandgap. Kang and Wise[103] have suggested that for PbS nanocrystals the 1.2 eV difference should be shared to equal shift of the valence and conduction energy levels of the nanocrystals relative to the bulk energy levels. This model means that the HOMO and LUMO levels of the 780 nm nanocrystals should be 5.7 and 4.1 eV respectively below the vacuum level. The latter values are supported by our finding that the HOMO level of ligand exchanged nanocrystals with excitonic peak at 850 nm is 5.7eV.

Let us consider now quantum confinement in SnS. We found that the SnS nanocrystals grown at 120$^{o}$C have an absorption onset at 1.47 eV. Their difference from bulk SnS is 0.3 eV and 0.2 eV for orthorombic and zinc blende phases respectively. Here we investigate whether SnS and PbS form a type-II heterojunction so let us consider for generality the extreme case that all quantum confinement in SnS goes to its valance band maximum level i.e. the HOMO level of the 120$^{o}$C orthorhombic and zinc blende SnS nanocrystals is 0.3 eV and 0.2 eV lower (on a negative energy axis) than the respective bulk materials as drawn in Figure 5.11.

To conclude Figure 5.11 contains measured energy levels of PbS, measured bandgaps of SnS and the estimated energy level values of bulk and nanocrystalline SnS based on the relative literature. This schematic suggests that i) bulk PbS forms a type-I heterojunction with orthorhombic SnS and a type-II junction with zinc blende SnS ii) PbS nanocrystals form a type-II junction with bulk and nanocrystalline SnS iii) the ionization potential offsets between PbS and SnS is larger for zinc blende SnS.

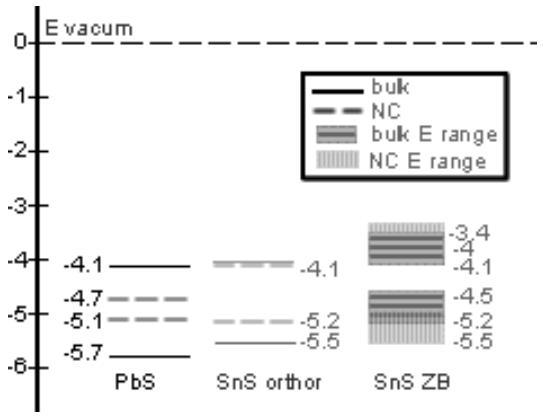


**Figure 5.11 Proposed band levels for PbS and SnS as discussed in the text.**

## *5.5 Conclusions*

We have developed an anhydrous organometallic route for the synthesis of SnS nanocrystals for photovoltaics. The size of the nanocrystals can be controlled by the growth temperature and their organic passivation can be altered with a ligand exchange route during layer by layer film fabrication. Characterisation of the structure and optoelectronic properties of the material has been reported and a notable result is that SnS nanocrystal films are photoconductive. The nanocrystals were successfully combined with PbS nanocrystals in bilayer heterojunction solar cells which are more efficient than single junction PbS control devices.

The bilayers have larger $V_{oc}$ and fill factors than the control devices and this gives the former higher power conversion efficiency. The $V_{oc}$ depends on both SnS and PbS nanocrystal size. Experiments on devices with different top electrodes indicate that the two materials form a type-II heterojunction. The same model is supported by drastic improvements in the $I_{sc}$ of the bilayers without compromising their $V_{oc}$ when the post-synthesis chemical processing of the SnS nanocrystals is optimised. These and other experiments on bilayers of various thicknesses indicate that the efficiency of the bilayer devices is currently limited by the conductivity in the SnS film, although the latter is not measured yet. Nevertheless the bilayers are highly efficient in the IR, may convert power up to 35% more efficiently and subsequently there is further scope for improvement and development.

# 6 Conclusions

## *6.1 Overall Conclusions*

We have performed a series of experiments on the synthesis, characterisation and photovoltaic application of inorganic semiconductor nanocrystals specifically CdS, PbS and SnS. We investigated two main approaches, the direct synthesis and application of nanocrystal/polymer composites and the surfactant assisted synthesis and application of nanocrystals. The experimental findings presented so far help us give answers to the questions raised at the beginning of this thesis (**1.1)** and will be discussed in the context of these central questions as follows below (**6.1.1**-**6.1.4**). The future work that we believe will complement this thesis and go beyond where we stopped is described in **6.2**. The Chapter and the thesis closes with an epilogue in **6.3** on my view of our work and my thinking on the question stated at the end of Chapter 1: what is the best material combination and device architecture for utilising nanocrystals in solar cells?

### 6.1.1 How can nanocrystal/polymer composites be directly synthesized and with what properties?

We have developed a method for the direct synthesis of PbS and CdS nanocrystals in a variety of conjugated macromolecule aromatic suspensions. The size of the nanocrystals can be controlled as a function of the reaction's temperature and duration. Formation of nanocrystals with anisotropic shapes is also possible. Post synthesis processing of these composites towards solar cell fabrication is challenging:

for PbS:MEH-PPV composites post-synthesis purification via alcohol induced precipitation results to the self-assembly of the nanocrystals in 2- and 3- dimensional structures. Based on detailed TEM investigation we propose that the PbS rods formed during the precipitation step are the result of an interplay between dipole-induced self assembly and face-to-face aggregation of the nanocrystals. Because of this interplay the size of the rods can be partially controlled by the polarity of the alcohol used for precipitation. When the highly polar methanol is used face-to-face interactions between the nanocrystals dominate and only 3D cubic colloidal particles are formed containing crystallographically aligned nanocrystals and most-likely polymer chains. The degree of crystallographic alignment of the nanocrystals in these 3D structures is remarkable, and is related to oxidation of nanocrystals. In a certain type of colloidal particles, hundreds of aligned nanocrystals are enclosed in a single lead sulphate crystal matrix epitaxially formed in between the nanocrystals. This the first evidence of oxidation-induced crystallographic alignment of nanocrystals. Due to the extent of nanocrystal aggregation/self-assembly and oxidation, bulk heterojunction solar cells of the synthesized organic/inorganic composites did not show promising photovoltaic performance although there have been evidence showing type-II charge transfer processes between the nanocrystals and the polymer.

### 6.1.2 How does the surface chemistry of nanocrystals affect their functionality in solar cells and how can it be controlled?

We have fabricated PbS nanocrystals films and changed their surface chemistry using various ligand exchanged processes found in the relevant literature on optoelectronic applications of nanocrystal films. In most applications original long

ligands like oleic acid molecules covering nanocrystals need to be replaced by shorter ligands or removed via annealing of the film. Ex-situ conducted XPS spectroscopy showed us that in general $PbSO_4$, $PbSO_3$ and PbO are present on the surface of PbS nanocrystals. Replacement of the oleic acid with butylamine is accompanied by further oxidation of the nanocrystals with formation of additional PbO and $PbSO_4$. Further treatment with methanol results in additional oleic acid removal and further oxidation of the nanocrystals via an increased growth of $PbSO_3$. Thermal annealing of nanocrystal films seems to remove oleic acid from the bulk of the film but is accompanied with two very undesirable effects: accumulation of oleic acid and lead oleate molecules on the surface of the film and heavy oxidation of the surface of the nanocrystals. The surface of nanocrystal films can be cleaned from oxide species via Ar ion etching however this is accompanied by creation of elemental Pb and S on the films and possibly etching of the PbS phase.

The above chemical effects are accompanied by important changes of physical properties: removal of oleic acid causes aggregation and/or decrease of interparticle spacing as evident the by red-shifts of the nanocrystal films' absorption onsets and excitonic absorption peaks. These changes are small when the ligand exchange is done on nanocrystal films and large when it is done in dissolved nanocrystals. In every treatment, the change of the nanocrystals' energy gap was accompanied by lowering of their HOMO level, from 5.9eV down to 5.3eV, as this was measured by ultraviolet photoelectron spectroscopy. The HOMO level is important because it determines the character of the heterojunction nanocrystals form with other semiconductor materials. We have therefore investigated engineering of the nanocrystals surface chemistry and electronic functionality by changing the organic ligands attached to the nanocrystals' surface.

### 6.1.3 How can different semiconductor nanocrystals be combined for the creation of improved all inorganic-nanocrystal solar cells?

Different semiconductor nanocrystals can be combined as in bulk semiconductor technology for the creation of efficient all inorganic heterojunctions. We have showed that for the case a bilayer heterojunction between SnS and PbS nanocrystals. We have optimised a fabrication method for the layer-by-layer deposition of these two materials to creation of 3D layered-structures. Via measurements of the photovoltaic properties of solar cell devices we have shown strong evidence of a type-II heterojunction formed between SnS and PbS nanocrystals. This model explains the directionality of the bilayers' photocurrents in solar cells with different electrode combinations. It also explains the higher $V_{oc}$ of the bilayers compared to the $V_{oc}$ of PbS Schottky-type control devices and the improvements achieved for the $I_{sc}$ of the bilayers. In addition, the efficiency of the bilayers is higher than the efficiency of the PbS-only control devices and considering the early stage of development of SnS nanocrystals we believe that there is further scope for improvement of the bilayer efficiency. All the above indicate that the study of all-inorganic nanocrystal heterojunctions has a great technological potential.

### 6.1.4 What is the best way of utilising PbS nanocrystals as an infrared photoactive material in low-cost solar cells- in plastic or in all inorganic cells?

In contrast to our unfruitful experiments on nanostructured organic/inorganic solar cells, we have presented two types of PbS nanocrystal-based solar cells with high external quantum efficiencies in the IR, nearly 20% for PbS Schottky-type cells.

Although the ~0.5% power conversion efficiencies of our all-inorganic cells are behind the ~3% reported in the literature for similar devices, they are among the highest reported for all types of PbS nanocrystal based solar cells. Ours and others data show the potential of PbS nanocrystal films as both good photo-absorbing and charge transport media in solar cells. The above force us to suggest that PbS nanocrystals are better utilized in all-inorganic devices.

## *6.2 Future Work*

For the immediate future, I plan to continue working the synthesis and photovoltaic applications of semiconductor nanocrystals. In my intentions is to further investigate certain aspects of the work presented in this thesis. Firstly, the XPS-UPS study presented here should be expanded for case of thiol-assisted layer-by-layer fabricated SnS and PbS nanocrystal films. This would help us optimise the SnS nanocrystals and understand the heterojunction character of SnS-PbS bilayer devices. A detailed comparative XPS investigation of thiol, butylamine and thiol-butylamine treated PbS nanocrystal films may also help us through some light on the controversial literature regarding the photostabilty of PbS nanocrystal films in solar cells. It would also be interesting, to perform a comparative study of the HOMO levels of PbS and SnS nanocrystals from both UPS and cyclic voltammetry techniques, for a range of nanocrystal sizes and chemical treatments.

The optoelectronic electronic properties of PbS and SnS nanocrystal films, like their charge carriers mobilities and concentrations and optical absorption coefficients, should also be studied for a range of nanocrystal sizes and chemical treatments. That would help us both to further understand the operating principles of

our bilayer devices and to find ways to optimise them. Experiments towards this direction are Hall effect measurements, time-of-flight measurements, impedance spectroscopy, and field effect transistor fabrication and testing. In addition the charge transfer processes between SnS and PbS nanocrystals should be directly studied using techniques like photoluminescence quenching and transient-photoluminescence decay measurements.

When available the above can be combined for the solid investigation of many material combinations and device architectures. We have investigated the photovoltaic application of primarily zinc blende SnS nanocrystals and the same should be done for orthorhombic SnS. In addition, the heterojunction character between the two SnS phases is a very interesting topic for future investigation towards the creation of non-toxic nanocrystal solar cells. Other non-toxic and potentially air-stable nanostructured chalcogenide and oxide nanocrystals should be also studied. Beyond the classic bilayer architecture, inorganic nanocrystals can be used to make bulk heterojunction films and alternating film structures towards creation of tandem solar cells. The dip-coating method we used can be applied for this purpose.

## *6.3 Epilogue*

Today using a standard Shlenk line, a centrifuge, a glovebox, an evaporator and lots of chemicals one is able to synthesize many kinds of semiconductor nanocrystals and make photovoltaic devices with them. One of the great pleasures of this scientific field is to watch a photovoltaic device being built up within a day, from solutions prepared by basic off-the-shelf chemicals and the expertise of a student. It

becomes more exciting when realising that each of these materials and devices is a case-study in the basic laws of quantum mechanics, electronics and physical chemistry- this field is a truly interdisciplinary one where no-one coming from the classic areas of physics, chemistry or electrical engineering can claim adequate background knowledge. On the contrary, this is a new field of science and technology being increasingly enriched by the findings of many different kinds of science published every week. A career in this field requires constant attention to the literature, ongoing learning of theories-courses-fields outside one's main scientific area and cooperation with other scientists.

It also requires vision addressing the two really hard challenges of the field: to make air-stable and non toxic nanocrystal- solar cells. This is necessary not only for the large scale commercialisation of the investigated technology but also for the well being of the researchers. I spent most of my time in the lab to control the environmental conditions during handling my nanocrystal samples and numerous multistep experiments failed when the environmental conditions were compromised at any stage of the experiments. Facing these problems often required long hours of work to complete series of experiments. More importantly however, I worked with lots of toxic chemicals. I took all the legally and ethically required precautions to avoid being in any way affected by these chemicals and doing so I realised more and more how bad these chemicals can be for the human and the environment.

For the above reasons my personal opinion on the question "what is the best material combination and device architecture for utilising nanocrystals in solar cells?" is that any combination of non-toxic and air-stable photovoltaic materials is very good and requires further studying. Although, the efficiencies of polymer/nanocrystal solar cells are being constantly increased conjugated polymers are still very unstable at

ambient conditions. All inorganic cadmium and lead chalcogenide nanocrystal based cells are also being improved in terms of both stability and efficiency however these materials are highly toxic. So probably the best nanocrystal solar cells are yet to be presented.

# Bibliography

1. Kumar, S.; Scholes, G. D., Colloidal nanocrystal solar cells. *Microchimica Acta* **2007**.
2. In ASTM standard table for reference solar spectral irradiances G 179-03, w. a. o.
3. Kittel, C., *Introduction to Solid State Physics*. 7th ed.; John Wiley & Sons, Inc.: 1996.
4. Nelson, J., *THE PHYSICS OF SOLAR CELLS*. 1 ed.; Imperial College Press: London, 2003.
5. Gaponenko, S. V., *Optical Properties of Semiconductor Nanocrystals*. CAMBRIDGE UNIVERSITY PRESS: Cambridge, 1998.
6. Alivisatos, A. P., Perspectives on the Physical Chemistry of Semiconductor Nanocrystals. *J. Phys. Chem.* **1996,** *100* (31), 13226-13239.
7. Bube, R. H., *Photovoltaic Materials*. 1 ed.; Imperial College Press: SERIES ON PROPERTIES OF SEMICONDUCTOR MATERIALS, 1998.
8. Waldauf, C.; Scharber, M. C.; Schilinsky, P.; Hauch, J. A.; Brabec, C. J., Physics of organic bulk heterojunction devices for photovoltaic applications. *Journal of Applied Physics* **2006,** *99* (10), 104503-6.
9. Greenham, N. C.; Peng, X.; Alivisatos, A. P., Charge separation and transport in conjugated-polymer/semiconductor-nanocrystal composites studied by photoluminescence quenching and photoconductivity. *Physical Review B* **1996,** *54* (24), 17628.
10. Korosak, D.; Cvikl, B., On the role of the interface charge in non-ideal metal-semiconductor contacts. *Applied Surface Science* **2005,** *250* (1-4), 63-69.
11. Martin A. Green, K. E. D. L. K. Y. H. W. W., SHORT COMMUNICATION Solar cell efficiency tables (version 28). *Progress in Photovoltaics: Research and Applications* **2006,** *14* (5), 455-461.
12. Sun, S. S. a. N. S. S., 14 Semiconductor Dot Based Nanocomposite Solar Cells, in Organic Photovoltaics: Mechanisms, Materials and Devices. 2005, Taylor and Francis Group, LLC: Florida.
13. Spanggaard, H. a. F. C. K., A brief history of the development of organic and polymeric photovoltaics. Solar Energy Materials And Solar Cells, 2004. 83(2-3): p. 125-146.
14. Coakley, K. M.; McGehee, M. D., Conjugated Polymer Photovoltaic Cells. *Chem. Mater.* **2004,** *16* (23), 4533-4542.
15. Scholes, G. D.; Rumbles, G., Excitons in nanoscale systems. *Nat Mater* **2006,** *5* (9), 683-696.
16. Hoppe Harald; Sariciftci, N. S., Organic solar cells: An overview. *J. Mater. Res.* **2004,** *19* (7), 1924-1945.
17. Gratzel, M., Dye-sensitized solar cells. *Journal of Photochemistry and Photobiology C: Photochemistry Reviews* **2003,** *4* (2), 145-153.
18. Meng, Q. B.; Takahashi, K.; Zhang, X. T.; Sutanto, I.; Rao, T. N.; Sato, O.; Fujishima, A.; Watanabe, H.; Nakamori, T.; Uragami, M., Fabrication of an Efficient Solid-State Dye-Sensitized Solar Cell. *Langmuir* **2003,** *19* (9), 3572-3574.
19. Kim, J. Y.; Lee, K.; Coates, N. E.; Moses, D.; Nguyen, T.-Q.; Dante, M.; Heeger, A. J., Efficient Tandem Polymer Solar Cells Fabricated by All-Solution Processing. *Science* **2007,** *317* (5835), 222-225.

20. Schwartz, B. J., CONJUGATED POLYMERS AS MOLECULAR MATERIALS: How Chain Conformation and Film Morphology Influence Energy Transfer and Interchain Interactions. *Annual Review of Physical Chemistry* **2003,** *54* (1), 141-172.
21. Friend, R. H.; Gymer, R. W.; Holmes, A. B.; Burroughes, J. H.; Marks, R. N.; Taliani, C.; Bradley, D. D. C.; Santos, D. A. D.; Bredas, J. L.; Logdlund, M.; Salaneck, W. R., Electroluminescence in conjugated polymers. *Nature* **1999,** *397* (6715), 121-128.
22. Colladet, K.; Nicolas, M.; Goris, L.; Lutsen, L.; Vanderzande, D., Low-band gap polymers for photovoltaic applications. *Thin Solid Films* **2004,** *451-452*, 7-11.
23. Markov, D. E., University of Groningen, The Netherlands: Excitonic Process in Polymer Based Optoelectronic Devices.
24. Woggon, U., *Optical Properties of Semiconductor Quantum Dots*. 1 ed.; Springer: Berlin, 1997.
25. Jamie, H. W.; Elizabeth, T.; Andrew, R. W.; Norman, R. H.; Halina, R.-D., Time-resolved photoluminescence spectroscopy of ligand-capped PbS nanocrystals. *Nanotechnology* **2005,** (2), 175.
26. M.A. Hines, G. D. S., Colloidal PbS Nanocrystals with Size-Tunable Near-Infrared Emission: Observation of Post-Synthesis Self-Narrowing of the Particle Size Distribution. *Advanced Materials* **2003,** *15* (21), 1844-1849.
27. Nozik, A. J., SPECTROSCOPY AND HOT ELECTRON RELAXATION DYNAMICS IN SEMICONDUCTOR QUANTUM WELLS AND QUANTUM DOTS. *Annual Review of Physical Chemistry* **2001,** *52* (1), 193-231.
28. Ellingson, R. J.; Beard, M. C.; Johnson, J. C.; Yu, P.; Micic, O. I.; Nozik, A. J.; Shabaev, A.; Efros, A. L., Highly Efficient Multiple Exciton Generation in Colloidal PbSe and PbS Quantum Dots. *Nano Lett.* **2005,** *5* (5), 865-871.
29. Murphy, J. E.; Beard, M. C.; Norman, A. G.; Ahrenkiel, S. P.; Johnson, J. C.; Yu, P.; Micic, O. I.; Ellingson, R. J.; Nozik, A. J., PbTe Colloidal Nanocrystals: Synthesis, Characterization, and Multiple Exciton Generation. *J. Am. Chem. Soc.* **2006,** *128* (10), 3241-3247.
30. Sukhovatkin, V.; Hinds, S.; Brzozowski, L.; Sargent, E. H., Colloidal Quantum-Dot Photodetectors Exploiting Multiexciton Generation. *Science* **2009,** *324* (5934), 1542-1544.
31. Manna, L.; Scher, E. C.; Alivisatos, A. P., Shape Control of Colloidal Semiconductor Nanocrystals. *Journal of Cluster Science* **2002,** *13* (4), 521-532.
32. Yin, Y.; Alivisatos, A. P., Colloidal nanocrystal synthesis and the organic-inorganic interface. *Nature* **2005,** *437* (7059), 664-670.
33. Joo, J.; Na, H. B.; Yu, T.; Yu, J. H.; Kim, Y. W.; Wu, F.; Zhang, J. Z.; Hyeon, T., Generalized and Facile Synthesis of Semiconducting Metal Sulfide Nanocrystals. *J. Am. Chem. Soc.* **2003,** *125* (36), 11100-11105.
34. Warner, J. H.; Cao, H., Shape control of PbS nanocrystals using multiple surfactants. *Nanotechnology* **2008,** *19* (30), 305605.
35. Pan, B.; He, R.; Gao, F.; Cui, D.; Zhang, Y., Study on growth kinetics of CdSe nanocrystals in oleic acid/dodecylamine. *Journal of Crystal Growth* **2006,** *286* (2), 318-323.
36. Koleilat, G. I.; Levina, L.; Shukla, H.; Myrskog, S. H.; Hinds, S.; Pattantyus-Abraham, A. G.; Sargent, E. H., Efficient, Stable Infrared Photovoltaics Based on Solution-Cast Colloidal Quantum Dots. *ACS Nano* **2008,** *2* (5), 833-840.
37. Talapin, D. V.; Murray, C. B., PbSe Nanocrystal Solids for n- and p-Channel Thin Film Field-Effect Transistors. *Science* **2005,** *310* (5745), 86-89.

38. Trindade, T.; O'Brien, P., A single source approach to the synthesis of CdSe nanocrystallites. *Advanced Materials* **1996,** *8* (2), 161-163.
39. Watt, A.; Rubinsztein-Dunlop, H.; Meredith, P., Growing semiconductor nanocrystals directly in a conducting polymer. *Materials Letters* **2005,** *59* (24-25), 3033-3036.
40. Young-wook Jun, J.-s. C. J. C., Shape Control of Semiconductor and Metal Oxide Nanocrystals through Nonhydrolytic Colloidal Routes. *Angewandte Chemie International Edition* **2006,** *45* (21), 3414-3439.
41. Peng, X.; Wickham, J.; Alivisatos, A. P., Kinetics of II-VI and III-V Colloidal Semiconductor Nanocrystal Growth: "Focusing" of Size Distributions. *J. Am. Chem. Soc.* **1998,** *120* (21), 5343-5344.
42. Manna, L.; Scher, E. C.; Alivisatos, A. P., Synthesis of Soluble and Processable Rod-, Arrow-, Teardrop-, and Tetrapod-Shaped CdSe Nanocrystals. *J. Am. Chem. Soc.* **2000,** *122* (51), 12700-12706.
43. Peng, X., Mechanisms for the Shape-Control and Shape-Evolution of Colloidal Semiconductor Nanocrystals. *Advanced Materials* **2003,** *15* (5), 459-463.
44. Peng, X.; Manna, L.; Yang, W.; Wickham, J.; Scher, E.; Kadavanich, A.; Alivisatos, A. P., Shape control of CdSe nanocrystals. *Nature* **2000,** *404* (6773), 59-61.
45. Ravirajan, P.; Peiro, A. M.; Nazeeruddin, M. K.; Graetzel, M.; Bradley, D. D. C.; Durrant, J. R.; Nelson, J., Hybrid Polymer/Zinc Oxide Photovoltaic Devices with Vertically Oriented ZnO Nanorods and an Amphiphilic Molecular Interface Layer. *J. Phys. Chem. B* **2006,** *110* (15), 7635-7639.
46. Manna, L.; Milliron, D. J.; Meisel, A.; Scher, E. C.; Alivisatos, A. P., Controlled growth of tetrapod-branched inorganic nanocrystals. *Nat Mater* **2003,** *2* (6), 382-385.
47. Lee, S.-M.; Jun, Y.-w.; Cho, S.-N.; Cheon, J., Single-Crystalline Star-Shaped Nanocrystals and Their Evolution: Programming the Geometry of Nano-Building Blocks. *Journal of the American Chemical Society* **2002,** *124* (38), 11244-11245.
48. Peumans, P.; Yakimov, A.; Forrest, S. R., Small molecular weight organic thin-film photodetectors and solar cells. *Journal of Applied Physics* **2003,** *93* (7), 3693-3723.
49. Huynh, W. U.; Dittmer, J. J.; Alivisatos, A. P., Hybrid Nanorod-Polymer Solar Cells. *Science* **2002,** *295* (5564), 2425-2427.
50. Huynh, W. U.; Dittmer, J. J.; Teclemariam, N.; Milliron, D. J.; Alivisatos, A. P.; Barnham, K. W. J., Charge transport in hybrid nanorod-polymer composite photovoltaic cells. *Physical Review B* **2003,** *67* (11), 115326.
51. Watt, A.; Eichmann, T.; Rubinsztein-Dunlop, H.; Meredith, P., Carrier transport in PbS nanocrystal conducting polymer composites. *Applied Physics Letters* **2005,** *87* (25), 253109-3.
52. Watt, A. A. R.; Meredith, P.; Riches, J. D.; Atkinson, S.; Rubinsztein-Dunlop, H., A PbS quantum-cube: conducting polymer composite for photovoltaic applications. *Current Applied Physics* **2004,** *4* (2-4), 320-322.
53. Afzaal, M.; O'Brien, P., Recent developments in II-VI and III-VI semiconductors and their applications in solar cells. *Journal of Materials Chemistry* **2006,** *16* (17), 1597-1602.
54. Jiang, X.; Schaller, R. D.; Lee, S. B.; Pietryga, J. M.; Klimov, V. I.; Zakhidov, A. A.; , PbSe nanocrystal/conducting polymer solar cells with an infrared response to 2 micron. *Journal of Materials Research* **2007,** *22* (8), 2204-2210.

55. McDonald, S. A.; Konstantatos, G.; Zhang, S.; Cyr, P. W.; Klem, E. J. D.; Levina, L.; Sargent, E. H., Solution-processed PbS quantum dot infrared photodetectors and photovoltaics. *Nat Mater* **2005,** *4* (2), 138-142.
56. W.U. Huynh, J. J. D. W. C. L. G. L. W. A. P. A., Controlling the Morphology of Nanocrystal-Polymer Composites for Solar Cells. *Advanced Functional Materials* **2003,** *13* (1), 73-79.
57. Gur, I.; Fromer, N. A.; Geier, M. L.; Alivisatos, A. P., Air-Stable All-Inorganic Nanocrystal Solar Cells Processed from Solution. *Science* **2005,** *310* (5747), 462-465.
58. Gur, I.; Fromer, N. A.; Alivisatos, A. P., Controlled Assembly of Hybrid Bulk-Heterojunction Solar Cells by Sequential Deposition. *J. Phys. Chem. B* **2006,** *110* (50), 25543-25546.
59. Sun, B.; Snaith, H. J.; Dhoot, A. S.; Westenhoff, S.; Greenham, N. C., Vertically segregated hybrid blends for photovoltaic devices with improved efficiency. *Journal of Applied Physics* **2005,** *97* (1), 014914-6.
60. Sun, B.; Marx, E.; Greenham, N. C., Photovoltaic Devices Using Blends of Branched CdSe Nanoparticles and Conjugated Polymers. *Nano Lett.* **2003,** *3* (7), 961-963.
61. Gur, I.; Fromer, N. A.; Chen, C. P.; Kanaras, A. G.; Alivisatos, A. P., Hybrid Solar Cells with Prescribed Nanoscale Morphologies Based on Hyperbranched Semiconductor Nanocrystals. *Nano Lett.* **2007,** *7* (2), 409-414.
62. Zhou, Y.; Li, Y.; Zhong, H.; Hou, J.; Ding, Y.; Yang, C.; Li, Y., Hybrid nanocrystal/polymer solar cells based on tetrapod-shaped CdSexTe1-x nanocrystals. *Nanotechnology* **2006,** *17* (16), 4041-4047.
63. Kumar, S.; T, N., First solar cells based on CdTe nanoparticles/MEH-PPV composites *Journal of Materials Research* **2004,** *19*, 1990.
64. Wise, F. W., Lead Salt Quantum Dots: the Limit of Strong Quantum Confinement. *Acc. Chem. Res.* **2000,** *33* (11), 773-780.
65. Schaller, R. D.; Petruska, M. A.; Klimov, V. I., Effect of electronic structure on carrier multiplication efficiency: Comparative study of PbSe and CdSe nanocrystals. *Applied Physics Letters* **2005,** *87* (25), 253102-3.
66. Zhang, S.; Cyr, P. W.; McDonald, S. A.; Konstantatos, G.; Sargent, E. H., Enhanced infrared photovoltaic efficiency in PbS nanocrystal/semiconducting polymer composites: 600-fold increase in maximum power output via control of the ligand barrier. *Applied Physics Letters* **2005,** *87* (23), 233101-3.
67. Watt, A. A. R.; Blake, D.; Warner, J. H.; Thomsen, E. A.; Tavenner, E. L.; Rubinsztein-Dunlop, H.; Meredith, P., Lead sulfide nanocrystal: conducting polymer solar cells. *Journal of Physics D: Applied Physics* **2005,** *38* (12), 2006-2012.
68. Cui, D.; Xu, J.; Zhu, T.; Paradee, G.; Ashok, S.; Gerhold, M., Harvest of near infrared light in PbSe nanocrystal-polymer hybrid photovoltaic cells. *Applied Physics Letters* **2006,** *88* (18), 183111-3.
69. Gunes, S.; Fritz, K. P.; Neugebauer, H.; Sariciftci, N. S.; Kumar, S.; Scholes, G. D., Hybrid solar cells using PbS nanoparticles. *Solar Energy Materials and Solar Cells* **2007,** *91* (5), 420-423.
70. Maria, A.; Cyr, P. W.; Klem, E. J. D.; Levina, L.; Sargent, E. H., Solution-processed infrared photovoltaic devices with > 10% monochromatic internal quantum efficiency. *Applied Physics Letters* **2005,** *87* (21), 213112-3.
71. Dissanayake, D. M. N. M.; Hatton, R. A.; Lutz, T.; Giusca, C. E.; Curry, R. J.; Silva, S. R. P., A PbS nanocrystal-C[sub 60] photovoltaic device for infrared light harvesting. *Applied Physics Letters* **2007,** *91* (13), 133506-3.

72. Clifford, J. P.; Johnston, K. W.; Levina, L.; Sargent, E. H., Schottky barriers to colloidal quantum dot films. *Applied Physics Letters* **2007,** *91* (25), 253117-3.
73. Johnston, K. W.; Pattantyus-Abraham, A. G.; Clifford, J. P.; Myrskog, S. H.; Hoogland, S.; Shukla, H.; Klem, E. J. D.; Levina, L.; Sargent, E. H., Efficient Schottky-quantum-dot photovoltaics: The roles of depletion, drift, and diffusion. *Applied Physics Letters* **2008,** *92* (12), 122111-3.
74. Johnston, K. W.; Pattantyus-Abraham, A. G.; Clifford, J. P.; Myrskog, S. H.; MacNeil, D. D.; Levina, L.; Sargent, E. H., Schottky-quantum dot photovoltaics for efficient infrared power conversion. *Applied Physics Letters* **2008,** *92* (15), 151115-3.
75. Luther, J. M.; Law, M.; Beard, M. C.; Song, Q.; Reese, M. O.; Ellingson, R. J.; Nozik, A. J., Schottky Solar Cells Based on Colloidal Nanocrystal Films. *Nano Letters* **2008,** *8* (10), 3488-3492.
76. W. J. E. Beek, M. M. W. R. A. J. J., Efficient Hybrid Solar Cells from Zinc Oxide Nanoparticles and a Conjugated Polymer. *Advanced Materials* **2004,** *16* (12), 1009-1013.
77. Beek, W. J. E.; Wienk, M. M.; Janssen, R. A. J., Hybrid polymer solar cells based on zinc oxide. *Journal of Materials Chemistry* **2005,** *15* (29), 2985-2988.
78. Oey, C. C.; Djurii, A. B.; Wang, H.; Man, K. K. Y.; Chan, W. K.; Xie, M. H.; Leung, Y. H.; Pandey, A.; Nunzi, J. M.; Chui, P. C., Polymer-TiO2 solar cells: TiO2 interconnected network for improved cell performance. *Nanotechnology* **2006,** *17* (3), 706-713.
79. Zeng, T.-W.; Lin, Y.-Y.; Lo, H.-H.; Chen, C.-W.; Chen, C.-H.; Liou, S.-C.; Huang, H.-Y.; Su, W.-F., A large interconnecting network within hybrid MEH-PPV/TiO2 nanorod photovoltaic devices. *Nanotechnology* **2006,** *17* (21), 5387-5392.
80. K.M. Coakley, Y. L. M. D. M. K. L. F. G. D. S., Infiltrating Semiconducting Polymers into Self-Assembled Mesoporous Titania Films for Photovoltaic Applications. *Advanced Functional Materials* **2003,** *13* (4), 301-306.
81. Sun, B.; Greenham, N. C., Improved efficiency of photovoltaics based on CdSe nanorods and poly(3-hexylthiophene) nanofibers. *Physical Chemistry Chemical Physics* **2006,** *8* (30), 3557-3560.
82. Kang, Y.; Park, N.-G.; Kim, D., Hybrid solar cells with vertically aligned CdTe nanorods and a conjugated polymer. *Applied Physics Letters* **2005,** *86* (11), 113101-3.
83. Lin, Y.-T.; Zeng, T.-W.; Lai, W.-Z.; Chen, C.-W.; Lin, Y.-Y.; Chang, Y.-S.; Su, W.-F., Efficient photoinduced charge transfer in TiO2 nanorod/conjugated polymer hybrid materials. *Nanotechnology* **2006,** *17* (23), 5781-5785.
84. Kanaras, A. G.; Sonnichsen, C.; Liu, H.; Alivisatos, A. P., Controlled Synthesis of Hyperbranched Inorganic Nanocrystals with Rich Three-Dimensional Structures. *Nano Lett.* **2005,** *5* (11), 2164-2167.
85. Dissanayake, D. M. N. M.; Lutz, T.; Curry, R. J.; Silva, S. R. P., Measurement and validation of PbS nanocrystal energy levels. *Applied Physics Letters* **2008,** *93* (4), 043501-3.
86. Dissanayake, D. M. N. M.; Hatton, R. A.; Lutz, T.; Curry, R. J.; Silva, S. R. P., The fabrication and analysis of a PbS nanocrystal:C60 bilayer hybrid photovoltaic system. *Nanotechnology* **2009,** *20* (24), 245202.
87. Wu, X.; Keane, J. C.; R.G.Dhere; DeHart, C.; Albin, D. S.; Duda, A.; Gessert; Asher; Levina; Sheldon In *16.5%-Efficient CdS/CdTe polycrystalline thin-film solar cell*, Seventeenth European Photovoltaic Solar Energy Conference: Proceedings of the International Conference, Munich, Germany, October 22–26; McNelis, B., Ed. Munich, Germany, 2001; pp 995–1000.

88. Wu, Y.; Wadia, C.; Ma, W.; Sadtler, B.; Alivisatos, A. P., Synthesis and Photovoltaic Application of Copper(I) Sulfide Nanocrystals. *Nano Letters* **2008,** *8* (8), 2551-2555.
89. Sun, B.; Findikoglu, A. T.; Sykora, M.; Werder, D. J.; Klimov, V. I., Hybrid Photovoltaics Based on Semiconductor Nanocrystals and Amorphous Silicon. *Nano Letters* **2009,** *9* (3), 1235-1241.
90. Choi, J. J.; Lim, Y.-F.; Santiago-Berrios, M. E. B.; Oh, M.; Hyun, B.-R.; Sun, L.; Bartnik, A. C.; Goedhart, A.; Malliaras, G. G.; AbrunÌƒa, H. c. D.; Wise, F. W.; Hanrath, T., PbSe Nanocrystal Excitonic Solar Cells. *Nano Letters* **2009**.
91. Nozik, A. J., Quantum dot solar cells. *Physica E: Low-dimensional Systems and Nanostructures* **2002,** *14* (1-2), 115-120.
92. T. S. Mentzel; V. J. Porter; S. Geyer, K. M.; M. G. Bawendi; Kastner, M. A., Charge transport in arrays of PbSe nanocrystals. *arXiv:0708.1135v1* **2007**.
93. Watt, A.; Thomsen, E.; Meredith, P.; Rubinsztein-Dunlop, H., A new approach to the synthesis of conjugated polymer-nanocrystal composites for heterojunction optoelectronics. *Chemical Communications* **2004,** (20), 2334-2335.
94. Thomsen, E. A. Characterisation of materials for organic photovoltaics. University of St Andrews, St Andrews, 2008.
95. Warner, J. H., Self-Assembly of Ligand-Free PbS Nanocrystals into Nanorods and Their Nanosculpturing by Electron-Beam Irradiation. *Advanced Materials* **2008,** *20* (4), 784-787.
96. Konstantatos, G.; Clifford, J.; Levina, L.; Sargent, E. H., Sensitive solution-processed visible-wavelength photodetectors. *Nat Photon* **2007,** *1* (9), 531-534.
97. Nenadovic, M. T.; Comor, M. I.; Vasic, V.; Micic, O. I., Transient bleaching of small lead sulfide colloids: influence of surface properties. *The Journal of Physical Chemistry* **2002,** *94* (16), 6390-6396.
98. Patel, A. A.; Wu, F.; Zhang, J. Z.; Torres-Martinez, C. L.; Mehra, R. K.; Yang, Y.; Risbud, S. H., Synthesis, Optical Spectroscopy and Ultrafast Electron Dynamics of PbS Nanoparticles with Different Surface Capping. *The Journal of Physical Chemistry B* **2000,** *104* (49), 11598-11605.
99. Watt, A. A. R.; Rubinsztein-Dunlop, H.; Meredith, P., A New Approach to the Synthesis of Nanocrystal Conjugated Polymer Composites. *Synthetic Metals* **2005,** *154* (1-3), 57-60.
100. Rolo, A. G.; Conde, O.; Gomes, M. J. M., Structural and optical studies of CdS nanocrystals embedded in silicon dioxide films. *Thin Solid Films* **1998,** *318* (1-2), 108-112.
101. Wang, Y.; Herron, N., Quantum size effects on the exciton energy of CdS clusters. *Physical Review B* **1990,** *42* (11), 7253.
102. Yu, Y.-M.; Kim, K.-m.; O, B.; Lee, K.-S.; Choi, Y. D.; Yu, P. Y., Band gap energy and exciton peak of cubic CdS/GaAs epilayers. *Journal of Applied Physics* **2002,** *92* (2), 1162-1164.
103. Kang, I.; Wise, F. W., Electronic structure and optical properties of PbS and PbSe quantum dots. *J. Opt. Soc. Am. B* **1997,** *14* (7), 1632-1646.
104. Cho, K. S.; Talapin, D. V.; Gaschler, W.; Murray, C. B., Designing PbSe Nanowires and Nanorings through Oriented Attachment of Nanoparticles. *J. Am. Chem. Soc.* **2005,** *127* (19), 7140-7147.
105. Zhang, X.; Zhang, Z.; Glotzer, S. C., Simulation Study of Dipole-Induced Self-Assembly of Nanocubes. *J. Phys. Chem. C* **2007,** *111* (11), 4132-4137.

106. Zhang, H.; Edwards, E. W.; Wang, D.; Mohwald, H., Directing the self-assembly of nanocrystals beyond colloidal crystallization. *Physical Chemistry Chemical Physics* **2006,** *8* (28), 3288-3299.
107. S.-M. Lee, S. N. C. J. C., Anisotropic Shape Control of Colloidal Inorganic Nanocrystals. *Advanced Materials* **2003,** *15* (5), 441-444.
108. Alexandros Stavrinadis; Richard Beal; Jason M. Smith; Hazel E. Assender; Andrew A. R. Watt, Direct Formation of PbS Nanorods in a Conjugated Polymer. *Advanced Materials* **2008,** *20* (16), 3105-3109.
109. Alexandros Stavrinadis, R. B. J. M. S. H. E. A. A. A. R. W., Direct Formation of PbS Nanorods in a Conjugated Polymer. *Advanced Materials* **2008,** *20* (16), 3105-3109.
110. Murray, C. B.; Kagan, C. R.; Bawendi, M. G., Self-Organization of CdSe Nanocrystallites into Three-Dimensional Quantum Dot Superlattices. *Science* **1995,** *270* (5240), 1335-1338.
111. Liu, Z.; Liang, J.; Xu, D.; Lu, J.; Qian, Y., A facile chemical route to semiconductor metal sulfide nanocrystal superlattices. *Chemical Communications* **2004,** (23), 2724-2725.
112. Brown, L. O.; Hutchison, J. E., Formation and Electron Diffraction Studies of Ordered 2-D and 3-D Superlattices of Amine-Stabilized Gold Nanocrystals. *J. Phys. Chem. B* **2001,** *105* (37), 8911-8916.
113. M. Nagel, S. G. H., A. Frömsdorf, A. Kornowski, Horst Weller Synthesis of Monodisperse PbS Nanoparticles and Their Assembly into Highly Ordered 3D Colloidal Crystals. *Z. Phys. Chem.* **2007,** *221* (3/2007), 427-437.
114. Hill, R., Rietveld refinement round robin. I. Analysis of standard X-ray and neutron data for PbSO4. *Journal of Applied Crystallography* **1992,** *25* (5), 589-610.
115. Hagihara, H., Surface Oxidation of Galena in Relation to its Flotation as Revealed by Electron Diffraction. *J. Phys. Chem.* **1952,** *56* (5), 610-615.
116. Kim, B. S.; Hayes, R. A.; Prestidge, C. A.; Ralston, J.; Smart, R. S. C., Scanning tunnelling microscopy studies of galena: the mechanism of oxidation in air. *Applied Surface Science* **1994,** *78* (4), 385-397.
117. Ethan J. D. Klem, D. D. M., Larissa Levina, Edward H. Sargent, Solution Processed Photovoltaic Devices with 2% Infrared Monochromatic Power Conversion Efficiency: Performance Optimization and Oxide Formation. *Advanced Materials* **2008,** *20* (18), 3433-3439.
118. Konstantatos, G.; Levina, L.; Fischer, A.; Sargent, E. H., Engineering the Temporal Response of Photoconductive Photodetectors via Selective Introduction of Surface Trap States. *Nano Lett.* **2008,** *8* (5), 1446-1450.
119. Li, Y.; Hou, Y.; Jin, H.; Shi, Q.; Wang, Y.; Feng, Z., Photovoltaic properties of MEH-PPV/TiO2 nanocomposites. *Chinese Science Bulletin* **2008,** *53* (18), 2743-2747.
120. Sargent, E. H., Infrared photovoltaics made by solution processing. *Nat Photon* **2009,** *3* (6), 325-331.
121. Barkhouse, D. A. R.; Pattantyus-Abraham, A. G.; Levina, L.; Sargent, E. H., Thiols Passivate Recombination Centers in Colloidal Quantum Dots Leading to Enhanced Photovoltaic Device Efficiency. *ACS Nano* **2008,** *2* (11), 2356-2362.
122. Klem, E. J. D.; MacNeil, D. D.; Levina, L.; Sargent, E. H., Solution Processed Photovoltaic Devices with 2% Infrared Monochromatic Power Conversion Efficiency: Performance Optimization and Oxide Formation. *Advanced Materials* **2008,** *20* (18), 3433-3439.

123. Luther, J. M.; Law, M.; Song, Q.; Perkins, C. L.; Beard, M. C.; Nozik, A. J., Structural, Optical, and Electrical Properties of Self-Assembled Films of PbSe Nanocrystals Treated with 1,2-Ethanedithiol. *ACS Nano* **2008,** *2* (2), 271-280.
124. Sean Hinds; Larissa Levina; Ethan J. D. Klem; Gerasimos Konstantatos; Vlad Sukhovatkin; Edward H. Sargent, Smooth-Morphology Ultrasensitive Solution-Processed Photodetectors. *Advanced Materials* **2008,** *20* (23), 4398-4402.
125. Remacle, F., On Electronic Properties of Assemblies of Quantum Nanodotsâ€ *The Journal of Physical Chemistry A* **2000,** *104* (20), 4739-4747.
126. Law, M.; Luther, J. M.; Song, Q.; Hughes, B. K.; Perkins, C. L.; Nozik, A. J., Structural, Optical, and Electrical Properties of PbSe Nanocrystal Solids Treated Thermally or with Simple Amines. *Journal of the American Chemical Society* **2008,** *130* (18), 5974-5985.
127. Konstantatos, G.; Sargent, E. H., PbS colloidal quantum dot photoconductive photodetectors: Transport, traps, and gain. *Applied Physics Letters* **2007,** *91* (17), 173505-3.
128. Hyun, B.-R.; Zhong, Y.-W.; Bartnik, A. C.; Sun, L.; Abrunì*f*a, H. D.; Wise, F. W.; Goodreau, J. D.; Matthews, J. R.; Leslie, T. M.; Borrelli, N. F., Electron Injection from Colloidal PbS Quantum Dots into Titanium Dioxide Nanoparticles. *ACS Nano* **2008,** *2* (11), 2206-2212.
129. HyoJoong Lee; Henry C. Leventis; Soo-Jin Moon; Peter Chen; Seigo Ito; Saif A. Haque; Tomas Torres; Frank Nüesch; Thomas Geiger; Shaik M. Zakeeruddin; Michael Grätzel; Md. Khaja Nazeeruddin, PbS and CdS Quantum Dot-Sensitized Solid-State Solar Cells: ldquoOld Concepts, New Resultsrdquo. *Advanced Functional Materials* **2009,** *9999* (9999), NA.
130. R. Hesse; P. Streubel; R. Szargan, Product or sum: comparative tests of Voigt, and product or sum of Gaussian and Lorentzian functions in the fitting of synthetic Voigt-based X-ray photoelectron spectra. *Surface and Interface Analysis* **2007,** *39* (5), 381-391.
131. Konstantatos, G.; Howard, I.; Fischer, A.; Hoogland, S.; Clifford, J.; Klem, E.; Levina, L.; Sargent, E. H., Ultrasensitive solution-cast quantum dot photodetectors. *Nature* **2006,** *442* (7099), 180-183.
132. Nowak, P.; Laajalehto, K.; Kartio, I., A flotation related X-ray photoelectron spectroscopy study of the oxidation of galena surface. *Colloids and Surfaces A: Physicochemical and Engineering Aspects* **2000,** *161* (3), 447-460.
133. Whelan, C. M.; Ghijsen, J.; Pireaux, J.-J.; Maex, K., Cu adsorption on carboxylic acid-terminated self-assembled monolayers: a high-resolution X-ray photoelectron spectroscopy study. *Thin Solid Films* **2004,** *464-465*, 388-392.
134. Chen, S.; Liu, W., Oleic acid capped PbS nanoparticles: Synthesis, characterization and tribological properties. *Materials Chemistry and Physics* **2006,** *98* (1), 183-189.
135. Ma, W.; Luther, J. M.; Zheng, H.; Wu, Y.; Alivisatos, A. P., Photovoltaic Devices Employing Ternary PbSxSe1-x Nanocrystals. *Nano Letters* **2009,** *9* (4), 1699-1703.
136. Klem, E. J. D.; MacNeil, D. D.; Cyr, P. W.; Levina, L.; Sargent, E. H., Efficient solution-processed infrared photovoltaic cells: Planarized all-inorganic bulk heterojunction devices via inter-quantum-dot bridging during growth from solution. *Applied Physics Letters* **2007,** *90* (18), 183113-3.
137. Klem, E. J. D.; Shukla, H.; Hinds, S.; MacNeil, D. D.; Levina, L.; Sargent, E. H., Impact of dithiol treatment and air annealing on the conductivity, mobility, and

hole density in PbS colloidal quantum dot solids. *Applied Physics Letters* **2008,** *92* (21), 212105-3.
138. Brubec, R. H., *Photovoltaic Materials*. Imperial College Press: London, 1998.
139. Renewable Research Data Centre, N. R. l. N., http://rredc.nrel.gov/solar/spectra/am1.5/, http://rredc.nrel.gov/solar/spectra/am1.5/.
140. Clifford, J. P.; Konstantatos, G.; Johnston, K. W.; Hoogland, S.; Levina, L.; Sargent, E. H., Fast, sensitive and spectrally tuneable colloidal-quantum-dot photodetectors. *Nat Nano* **2009,** *4* (1), 40-44.
141. Ethan J. D. Klem, D. D. M. L. L. E. H. S., Solution Processed Photovoltaic Devices with 2% Infrared Monochromatic Power Conversion Efficiency: Performance Optimization and Oxide Formation. *Advanced Materials* **2008,** *20* (18), 3433-3439.
142. Eric C. Greyson, Jeremy E. B. Teri W. O., Tetrahedral Zinc Blende Tin Sulfide Nano- and Microcrystals13. *Small* **2006,** *2* (3), 368-371.
143. Johnson, J. B.; Jones, H.; Latham, B. S.; Parker, J. D.; Engelken, R. D.; Barber, C., Optimization of photoconductivity in vacuum-evaporated tin sulfide thin films. *Semiconductor Science and Technology* **1999,** (6), 501.
144. Chamberlain, J. M.; Merdan, M., Infrared photoconductivity in p-SnS. *Journal of Physics C: Solid State Physics* **1977,** (19), L571.
145. Ghosh, B.; Das, M.; Banerjee, P.; Das, S., Fabrication of the SnS/ZnO heterojunction for PV applications using electrodeposited ZnO films. *Semiconductor Science and Technology* **2009,** *24* (2), 025024.
146. Hickey, S. G.; Waurisch, C.; Rellinghaus, B.; EychmuÌˆller, A., Size and Shape Control of Colloidally Synthesized IVâˆ’VI Nanoparticulate Tin(II) Sulfide. *Journal of the American Chemical Society* **2008,** *130* (45), 14978-14980.
147. Nair, D. A. M. T. S. N. P. K. In *SnS Thin Films in Chemistry Deposited Solar Cell Structures*, Materials Research Society Spring Meeting 2007, Thin-Film Compound Semiconductor Photovoltaics-, 2007; Wada, T. G. K. D. C. H. S. M. T., Ed. Materials Research Society: 2007.
148. Williams, R. H.; Murray, R. B.; Govan, D. W.; Thomas, J. M.; Evans, E. L., Band structure and photoemission studies of SnS2 and SnSe2. I. Experimental. *Journal of Physics C: Solid State Physics* **1973,** (24), 3631.
149. Koktysh, D.; McBride, J.; Rosenthal, S., Synthesis of SnS nanocrystals by the solvothermal decomposition of a single source precursor. *Nanoscale Research Letters* **2007,** *2* (3), 144-148.
150. Noguchi, H.; Setiyadi, A.; Tanamura, H.; Nagatomo, T.; Omoto, O., Characterization of vacuum-evaporated tin sulfide film for solar cell materials. *Solar Energy Materials and Solar Cells* **1994,** *35*, 325-331.
151. G. Guizzetti; F. Filippini; E. Reguzzoni; G. Samoggia, Electrical properties and spectral response of PbS-Ge heterojunctions. *Physica Status Solidi (a)* **1971,** *6* (2), 605-610.
152. Rahnamai, H.; Zemel, J. N., The PbS---Si heterojunction II: Electrical properties. *Thin Solid Films* **1980,** *74* (1), 17-22.
153. Kanazawa, H.; Adachi, S., Optical properties of PbS. *Journal of Applied Physics* **1998,** *83* (11), 5997-6001.
154. U. Berg; T. Chassé; O. Brümmer, Investigation of the XPS Valence Band Structure from Sn Chalcogenides. *physica status solidi (b)* **1981,** *108* (2), 507-510.
155. Shalvoy, R. B.; Fisher, G. B.; Stiles, P. J., X-ray photoemission studies of the valence bands of nine IV-VI compounds. *Physical Review B* **1977,** *15* (4), 2021.

156. Otto, A.; Ley, L.; Azoulay, J.; Grandke, T.; Eymard, R.; Braun, W.; Cardona, M., Electron-hole interaction in the d-electron excitations of GeS and SnS. *Physical Review B* **1977,** *16* (10), 4429.
157. Ichimura, M., Calculation of band offsets at the CdS/SnS heterojunction. *Solar Energy Materials and Solar Cells* **2009,** *93* (3), 375-378.